UNIVERSITY OF OKLAHOMA

GRADUATE COLLEGE

EVALUATION OF THE WARN-ON-FORECAST SYSTEM WITH DOPPLER LIDAR AND MOBILE RADIOSONDE OBSERVATIONS FROM TORUS 2019

A THESIS

SUBMITTED TO THE GRADUATE FACULTY

In partial fulfillment of the requirements for the

Degree of

MASTER OF SCIENCE IN METEOROLOGY

By

JORDAN LASER

Norman, Oklahoma

2020

EVALUATION OF THE WARN-ON-FORECAST SYSTEM WITH DOPPLER LIDAR AND MOBILE RADIOSONDE OBSERVATIONS FROM TORUS 2019

A THESIS APPROVED FOR
THE SCHOOL OF METEOROLOGY

BY THE COMMITTEE CONSISTING OF

Dr. Michael Coniglio, chair

Dr. Patrick Skinner

Dr. Jason Furtado

Dr. Naoko Sakaeda

Acknowledgements

I would first like to thank Dr. Michael Coniglio and Dr. Patrick Skinner for reaching out to me about this work. This project not only gave me the rare opportunity to be a part of a historic field mission, but also pushed me to learn new computer skills. I'd also like to thank Dr. Elizabeth Smith for time, effort, and lidar expertise. Mike, Pat and Liz were patient with me throughout my masters and were available for questions when I had them. This project felt quite open ended, and they allowed me to find my own way, while providing invaluable advise and direction. I truly feel lucky to have been a part of this research group.

Next, I'd like to thank Dr. Sean Waugh for the conversations over observational platforms and for allowing me to help with general vehicle maintenance and field mission preparation. It's extremely valuable to get hands-on experience and Sean welcomed me into the vehicle bay and gave me the opportunity to participate in the hurricane Dorian deployment.

I'd like to thank Kelsey Britt for supplying me with two critically important Python scripts and answering the questions I threw her way from time to time. As Pat's PhD student, Kelsey was sort of put in a position where I required her help, and she always seemed happy to lend a hand. I'd also like to thank Noah Brauer for offering his sounding script to me and also his moral support. Noah and I served on two field missions together and was a great friend to have during my masters.

I'd also like to thank both Dr. Jason Furtado and Dr. Naoko Sakaeda. They both agreed to positions on my committee under a relatively aggressive time line and fit my defense into the first week of school. I truly appreciate the sacrifice and hope the quality of this paper justifies the time and effort.

Table of Contents

List of Figures

Abstract

Doppler lidar and mobile radiosonde observations from the Targeted Observations with Radars and UAS of Supercells 2019 (TORUS2019) field project are compared to the environmental guidance NSSL Warn-on-Forecast System (WoFS). The aim of WoFS is to provide short-term, storm-scale, probabilistic guidance for severe thunderstorm hazards. As the evolution of convective storms is modulated by the properties of the inflow environment, an accurate prediction of these properties is important for forecasting the evolution of an individual thunderstorm. However, the scarcity of routine observations of the inflow environment of thunderstorms makes evaluation of the quality of WoFS environmental forecasts difficult. Therefore, this study will assess the accuracy of WoFS predictions of the inflow environment of supercells through comparisons to TORUS2019 Doppler lidar and radiosonde observations.

Three case studies from TORUS2019 are explored to evaluate WoFS forecasts: 17 May, 20 May, and 23 May. 16 radiosonde observations and 5 lidar deployments are available for comparison during WoFS forecasts. All 16 radiosondes made it above 3 km so SRH comparisons can be made with all. However only 5 radiosondes traveled high enough (equilibrium level, EL) to compute CAPE, a testament to the tumultuous environment in which they were released. Five lidar deployments are analyzed, three of which are ~ 1 hour long. Three out of four observed supercells on these days produced a tornado within 1 hour and 40 km of a lidar deployment.

WoFS over forecasted mixed-layer and surface based convective available potential energy (MLCAPE and SBCAPE) in all 5 radiosonde observations available for comparison, owing largely to positive surface temperature error and negative temperature error above the plentary boundary layer(PBL). The YSU (PBL) scheme consistently forecasted lower CAPE and thus had the lowest error. Similarly, YSU often forecasted lower storm-relative helicity (SRH), a common trend as Cohen et al. (2015) and (2017) found. SRH comparisons show WoFS typically under forecasting SRH at later times in the evening on 17 May and 23rd, owing to differences in storm motion and more backing in the observation. WoFS well forecasts SRH on 20 May, with small negative errors in YSU and MYJ; The observation falls within the 50th percentile of MYNN for 4 out of 6 observations.

The lidar deployments show WoFS modifying the near-storm environment as the storm approaches similarly to that of the observation, except when the intensity of the mesocyclone is variable. Following a drop in rotational velocity of the mesocyclone, WoFS backs the winds during the first deployment on 20 May, however the observations do not back, likely as a response to the variable mesocyclone intensity. The lidar deployment on 17 May observed a supercell with constant rotational velocity and WoFS forecasts backing of the winds, but not to the same extent as in the observation.

1 Introduction and Motivation

Weather forecasters issue severe weather warnings largely based on observational data collected by the WSR 88-D network. When issuing tornado warnings specifically, the signs of tornado formation are evident in radar data only for a short time (<20 minutes) before the hazard may impact the public. This small time window for issuing a warning motivates the need for predictive systems that can supply forecasters with a glimpse into the possible future states of severe weather.

The Warn-on-Forecast System (WoFS) provides short-term, storm-scale, probabilistic guidance for severe thunderstorm hazards. WoFS is composed of 18 distinct members, making it an "ensemble" of models, from which severe weather associated probabilities can be calculated. This system assimilates observations in real time from satellite, radar and ASOS stations. Assimilating observations allows the model to suppress spurious convection and provide more accurate forecasts of thunderstorm intensity and track (Skinner 2018).

The assimilation of observations, however, does not automatically imply that the model will either accurately represent the environment in which thunderstorms may develop or forecast the evolution of a thunderstorm within that environment. Evaluating the performance of WoFS is essential to understanding its behavior and interpreting its forecasts. Several studies have evaluated WoFS storm-scale predictions using object-based methods that focus largely on the spatio-temporal positioning of modeled storms (Skinner 2016, 2018). These studies use the Multi-Radar/Multi-Sensor System (MRMS) to match observed thunderstorm objects to modeled objects, and uses contingency table-based metrics to quantify forecast quality. While these studies provide bulk statistics on WoFS performance, they do not consider the upstream environment or smaller storm scale features that could be important for thunderstorm evolution.

The Targeted Observation with Radars and Uncrewed Aerial Systems (UAS) of Supercells 2019 (TORUS) field campaign offered the opportunity to collect observations near enough (<80 km) to supercells to capture processes that are not commonly observed with operational soundings. This mission provides a rare opportunity to evaluate WoFS's environmental forecasts as well as WoFS's ability to predict modification between the thunderstorm and its environment. Supercells can modify the ambient environment by creating storm scale boundaries to be more conducive for strong rotating updrafts (Kerr et al. 2019), and it is unknown to what degree WoFS is predicting these modifications.

To assess the quality of WoFS environmental forecasts and associated modifications, three tornadic supercells from TORUS 2019 serve as case studies and are analyzed with mobile radiosonde and Doppler wind lidar observations: the 17 May McCook, Nebraska, the 20 May Mangum, Oklahoma, and the 23 May Canadian, Texas supercells, all of which produced significant tornadoes. TORUS radiosonde data are used to provide vertical profiles of thermodynamic and dynamic quantities to show the differences between observed and modeled convective parameters. The TORUS lidar data provide rare and novel time series of the vertical wind profile below 2 km in the inflow of supercells. The lidar deployments analyzed in these case studies often begin in what is typically referred to as the far-field (>40km from storm) and end in the near-field (<40 km from storm), providing a rare look at storm modification gradients as the storm approaches the stationary lidar.

The following points are the scientific questions the paper aims to answer, followed by hypothesises to these questions:

1. How closely is WoFS representing the inflow environment?
    - Considering WoFS boundary and initial conditions are provided by an operational numerical model, WoFS should predict inflow environments roughly similar to reality and at least supportive of supercells.
2. How accurate are WoFS storm scale predictions?
    - Assimilation of radar reflectively should lead to small location errors for storms observed by radar for long periods of time, on the order of an hour or longer. Larger errors should be expected for relatively new cells or storms that are very weak and may be extinguished by near by zero reflectively data assimilation.
3. To what extent is WoFS predicting storm modification to the inflow environment?
    - The YSU scheme has shown to produce weaker storms (Potvin et al. 2020) so it's expected that the environments in the local schemes are more modified than in the non-local schemes.
4. Can the ensemble mean be improved by weighting members based on PBL scheme?
    - While the YSU scheme has shown smaller systematic biases in environmental variables (Potvin et al. 2020), the hypothesized weaker storm modification in these

members may have competing impacts on PBL scheme performance. However, Cohen et al. (2017) showed the non-local schemes may forecast more accurate hodographs, which is critical for supercell evolution. Even if some members seem to be out performing others, maintaining ensemble spread may be more important than weighting more accurate members.

2 Review of Literature

2.1 Warn-on-Forecast System

Technological advancements in weather surveillance have had a marked impact on preventing loss of life and property. The implementation of the WSR-88D network has helped forecasters issue more accurate warnings for severe weather, and particularly tornadoes (Serafin and Wilson 2000, Brooks 2004, Simmons and Sutter 2005). While observing systems like the WSR-88D network provide crucial real time information to operational forecasters, the warnings issued based on observations are limited in the maximum amount of lead time they can provide to the public to prepare (Stensrud et al. 2009).

Numerical weather prediction systems have shown the potential to reproduce the structure of supercell thunderstorms and their associated severe weather hazards (Klemp and Wilhelmson 1978, Weisman and Klemp 1982, Wicker and Wilhelmson 1995). With these promising studies comes the desire to explicitly predict supercell formation and evolution before the severe weather threat is imminent. Continued advancement in computer power has allowed for explicit convection modeling systems to produce forecasts rapidly enough to provide useful information to forecasters (Pielke and Carbone 2002, Weisman et al 2008).

One numerical weather prediction system, WoFS aims to provide short-term (0-3 hr) probabilistic guidance for severe weather events like hail, flash floods and tornadoes (Stensrud et al. 2009). Recent work has shown WoFS, and similar systems, can produce skillful predictions of severe hail (Snook et al. 2016), tornadic mesocyclones (Dawson et al. 2012, Yussouf et al. 2013), and flash flooding events (Yussouf et al. 2016). WoFS has also been shown to produce accurate forecasts of thunderstorm and mesocyclone position on scales typical of NWS warning within an object-based framework with probability-of-detection values exceeding 0.7 for 30-minute forecasts of composite reflectivity (Skinner et al. 2016, 2018).

The Warn on Forecast System (WoFS) is a Weather Research Forecast-Advanced Research WRF (WRF-ARW, Skamarock and Klemp 2008) based convection allowing ensemble composed of 18 unique members designed to forecast severe weather threat probabilities. The model is run over a 900 km x 900 km domain and is gridded with 51 vertical levels and 3 km horizontal grid spacing. Radar and satellite observations are assimilated every 15 minutes while surface observations from ASOS are assimilated every hour using an ensemble Kalman filter (Wheatley et al. 2015, Jones et al. 2015). The 18 unique members are differentiated by their planetary boundary layer(PBL), longwave, and shortwave radiation schemes. Past studies have shown negligible difference in forecast quality across radiation schemes (Potvin et al. 2020) so the analysis presented in this study will focus on evaluating performance of different PBL schemes.

2.2 Planetary Boundary Layer Schemes

Three-dimensional turbulent processes take place on a wide range of spatial and temporal scales, often below the resolution of numerical models. Although large turbulent eddies may begin to resolved on a 3km grid, abundant turbulent motions smaller than 3 km in the PBL motivates the parameterization of their impacts on grid-scale variables (Stensrud et al. 2007). The 18 unique ensemble members in WoFS use three PBL schemes: the Yonsei University (YSU; Hong et al. 2016), the Mellor-Yamada-Nakanishi Niino (MYNN, Nakanishi and Niino

2004, 2006), and the Mellor-Yamada-Janjic (MYJ; Janjic 2002) schemes. Although these schemes were originally designed for use on grid lengths larger than 3 km, these schemes continue to be used widely in convection allowing models.

The primary difference between these schemes is how the surrounding variables are used to compute mixing at a given grid point. The Newtonian equations of motion, when applied to the PBL, yield turbulent-mixing equations that depend on wind shear and vertical gradients of temperature and moisture. The values of these gradients depend on the method used to calculate them. The local (MYJ and MYNN) schemes constrain the turbulent-mixing equations to use only adjacent vertical grid points, while the non-local (YSU) scheme incorporates more than adjacent grid points in the calculation of state variables (Cohen et al. 2015). A known issue with local schemes is their depiction of localized stability maxima, which may prevent the large-scale mixing that largely influences the thermal profile in the PBL (Stensrud 2007). The non-local schemes are designed to better predict environments characterized by strong surface heating by accounting for the counter-gradient fluxes associated with large turbulent motion (Stull 1991).

In an evaluation of 4-km WRF PBL schemes in the southeast United States cold season, Cohen et al. (2015) highlighted the ability of non-local schemes to better predict the depth of the boundary layer and to produce more realistic hodographs compared to the local schemes, while both local and non-local schemes overestimated mixed-layer convective available potential energy (MLCAPE). Perhaps a somewhat contradictory finding from a later study, Cohen et al. (2017) found that the non-local schemes underestimated 0-3 km storm-relative helicity(SRH), suggesting that the more aggressive mixing in those different cases had the impact of smoothing out the low-level hodograph and effectually reducing shear. Also, the non-local schemes were found to slightly over forecast water vapor mixing ratio in the lowest 100 hPa, perhaps a consequence of under forecasting the extent of mixing. Overall, Cohen et al. (2017) found the asymmetric cloud model version 2(ACM2) and its variants (non-local schemes) to produce the smallest differences from the Rapid Update Cycle (RUC) model.

Coniglio et al. (2013) compared nearly 400 operational soundings to the 5 different PBL schemes in 4-km WRF forecasts of morning and evening convection: 2 non-local: YSU and ACM2, 3 local: MYJ, MYNN, and the quasi-normal scale elimination (QNSE) scheme. All schemes predicted morning PBLs that were too cool and dry (small error in PBL depth besides YSU) in the morning. In the evening, the local schemes forecasted PBLs that were too shallow and moist, except for the MYNN scheme that performed better and was comparable to the coarser-resolution North American Mesoscale (NAM) model forecasts. The morning cool and moist errors resulted in an under forecast of MLCAPE and an over forecast of mixed-layer convective inhibition (MLCIN). When MLCAPE was large, the non-local and MYNN schemes underpredicted MLCAPE, while MYJ and QNSE over predicted MLCAPE when MLCAPE was small.

Potvin et al. (2020) showed, through an object oriented approach similar to Skinner et al. (2018), that all three WoFS PBL schemes (YSU, MYJ, MYNN) exhibited a cool, moist bias at the surface, with YSU posting the smallest biases. However, YSU consistently under forecasts surface based (SB) CAPE, while the other members do not. All schemes under forecasted convective inhibition, likely leading to a positive storm frequency bias identified in Skinner et al. (2018). YSU schemes were found to produce weaker storms, likely because of the less favorable near storm environment in these members. In addition, Potvin et al. (2020) showed that PBL scheme did not alter important storm-environment interactions, so the difference in storm intensity is probably a result of environmental differences among the PBL schemes. They conclude that weighting WoFS members by PBL scheme may modestly improve probabilistic forecast guidance for convective hazards.

2.3 Supercell Dynamics and Feedbacks

Tornadoes, one of the most violent forms of severe weather, exist in the PBL and spawn from rotating thunderstorms with strong updrafts. Rotating thunderstorms, coined 'supercells', require sufficient tropospheric mid-level wind shear in order to form (Rotunno and Klemp 1982). This shear helps to sustain a thunderstorm by separating the cold downdraft from the warm and moist updraft. Once a supercell forms, the process of tornado formation, or tornadogenesis, occurs when horizontal low-level vorticity is tilted, lifted, and stretched into the vertical by the updraft.

Balloon-borne radiosondes are often used to diagnose the environment's potential for supercell and tornado formation. This device observes the environment by measuring temperature, humidity, and wind as it ascends through the atmosphere. The vertical profile of temperature and dewpoint is typically presented on a skew-T log-P diagram and with the vertical profile of the horizontal winds presented on a hodograph. Variables retrieved from soundings, like SRH and CAPE, help diagnose the magnitudes of vertical wind shear and buoyancy, respectively.

SRH and CAPE have been used as proxies to determine potential for supercell formation and evolution (Rotunno and Klemp 1981, 1983, Davies-Jones 1984, Thompson et al. 2007). Composite studies have been performed to identify patterns of SRH, CAPE, and many other variables in tornadic and non-tornadic environments. In general, tornadoes become more likely as SRH increases and the lifting condensation level decreases in the environment (Rasmussen and Blanchard 1998). However, CAPE and many other variables relevant to convective forecasting are not substantially different between non-tornadic and tornadic cases (Thompson 2007), implying that the state of the environment prior to supercell formation, is not be enough information to forecast tornadogenesis (Coffer et al 2015). Anderson-Frey (2016) postulated that this is due to either a lack of understanding on how ambient environments influence tornadogenesis, or perhaps more likely that tornadogenesis is strongly influenced by storm-scale features that are rarely sampled by operational soundings. These storm-scale features are generated by the supercell and thus create a feedback between the supercell and the environment in which it exists.

An important storm-scale feature in supercells is the cold pool that forms by precipitation evaporatively cooling the air in and around the supercell that becomes negatively buoyant and descends toward the ground. This descending air usually reaches the surface, typically to the north and west of the updraft, and spreads outward along the ground. Baroclinic generation of vorticity results in the near-surface vertical vorticity required for tornadogenesis (Markowski and Richardson 2013). Another feedback to consider is the pressure perturbations that form within and around supercells, resulting from the large latent heating and cooling and the deformation of the wind field, including rotation in updraft (Rotunno and

Klemp 1981, 1983). For instance, the mesoscale low pressure that forms beneath a strong rotating updraft causes an acceleration of air toward the storm and enhances the wind field near the supercell, increasing local SRH and making the environment more conducive for tornadogenesis (Kerr et al. 2019, Flournoy 2020).

Potvin et al. (2010) performed a composite study of operational soundings in order to determine the spatiotemporal limits on storm modification: 40-80 km and within one hour of a tornado was determined to be the "Goldilocks Zone" (GZ) in which a proximity sounding was most likely to sample the ambient environment, without interference from the storm itself. This paper will use the terms "far-field" and "near-field", where far-field is synonymous with the GZ and the near-field is within 40 km from the storm velocity couplet. The GZ region was identified based on the idea that radiosonde observations made closer to the storm should be representative of the ambient environment, up until a distance at which storm feedbacks begin to modify the near-storm environment. These feedbacks could include anvil shading related cooling of the surface and the air just above it (Frame and Markowski 2013), cold outflow from the storm, and wind field strengthening due to low pressure perturbations associated with a rotating updraft.

Parker et al. 2014 analyzed near-storm soundings, particularly in the inflow (generally south-east of the storm), obtained during the second Verification of the Origins of Rotation in Tornadoes Experiment (VORTEX2; Wurman et al. 2012). This data set found a "dramatic" increase in SRH near the storm, owing largely to latent heat release and dynamic pressure effects (negative pressure perturbations), although interestingly the increase was found to be much larger for the nontornadic supercells compared to the tornadic supercells. Wade et al. (2018) looked at sounding pairs released simultaneously near supercells, one in the near-field and on in the far-field. Wade et al. (2018) found that the 0-1 km SRH in the near-field of tornadic supercells increased, but not for non-tornadic cases. Wade et al. (2018) also found the near storm winds to back in the lowest kilometer AGL. These findings are supported by Kerr et al. (2019), who quantitatively showed that a positive feedback can occur in which supercells enhance the environmental vertical wind-shear within in the inflow region that further strengthens the rotating updraft.

2.4 Summary of Literature

The typical purpose of evaluating a numerical weather prediction system is to quantify how closely the system resembles the real weather. The studies that have been done on the ambient environment, supercell characteristics, and the feedbacks between the two provide context for comparisons between WoFS and observations of real weather. The trends found (such as those in Potvin et al. 2020 and Cohen et al. 2017) in these studies motivate inspecting WoFS to look for similar trends, such as increasing SRH in the near field. These studies also inform researchers on how to best communicate findings that have relevant implications for the performance of the model (e.g. distinguishing between near and far field when inspecting storm-environment feedbacks, Potvin et al. 2010).

The research presented in this paper aims to add to the studies that have analyzed WoFS and other numerical weather prediction systems, specifically in regards to PBL scheme performance. Many of these past studies typically statistically compared large numbers of operational radiosonde observations to various models. However, this research is the first to compare observations of the inflow of supercell with both Doppler wind lidar and mobile radiosondes to WoFS environmental forecasts.

3 Methodology

3.1 The Field Campaign

The Targeted Observation with UAS and Radar of Supercells (TORUS) field campaign is a collaborative project including the University of Nebraska, University of Colorado, Texas Tech University, University of Oklahoma, the National Severe Storms Laboratory (NSSL), and the Cooperative Institute for Mesoscale Meteorological Studies (CIMMS) and is motivated by improving the current conceptual model of supercell thunderstorms. The aim of TORUS is to reveal the four-dimensional character of storm-generated boundaries and coherent structures that are crucial to tornadogenesis and the evolution of supercells.

A plethora of observational platforms were used for TORUS: Doppler wind lidar, mobile mesonets (Straka et al. 1996), radiosondes, uncrewed aerial systems (UAS, Argrow and Houston 2007), Ka-band (Weiss et al. 2009) and X-band (Burgess et al. 2010) mobile Doppler radars, and the NOAA P-3 Orion Hurricane Hunter (Collins 2014). The first TORUS field phase occurred in spring of 2019 and was fully nomadic in the American Great Plains. The spring of 2019 was an extremely active season in 2019 with 19 supercells targeted from May 16th - June 15th. The first three days of tornadic supercells from TORUS are the focus in this study: 17, 20, and 23 May.

3.2 Observations

This study uses profiles of the lower atmosphere collected with Doppler lidar and mobile radiosondes as these data set provide the best, highest-resolution data sets available from TORUS of the PBL. Note that the data collected in the PBL by TORUS from the other observational platforms (e.g. UASs, P-3 compact raman lidar and dual-Doppler analyses) continue to undergo quality control (QC) and were not available to the author. There were 118 radiosondes launched and 37 deployments of the Doppler wind lidar, of which a subset of 28 radiosonde launches and 8 lidar deployments occurred across the three case studies examined here.

The sounding data are collected every 1 second with Vaisala RS41-SGP radiosondes (Vaisala 2018),which relates to a vertical resolution of 4-5 meters given the nominal balloon ascent rate of 4-5 ms^{-1}.

The lidar used in this study is a Halo Photonics Steamline XR Doppler Lidar and was mounted in the bed of a truck. The lidar was stationary while collecting data. The standard lidar scanning strategy during TORUS was a 70-degree elevation PPI scan every 2 minutes with vertical stares in between. The vertical profile of horizontal wind components used in this study were derived by passing the PPI scans through a Velocity Azimuthal Display (VAD) technique (Liang 2007). The lidar parameters allow for very high spatial and temporal resolution wind profiles; approximately 18 m in the vertical (starting at $\sim$ 60 m AGL) and 30-45 s in time. The vertical velocity profiles derived from the vertical stares were not used because the vertical velocity field in WoFS is typically contaminated with unphysical gravity waves resulting from data assimilation.

The data collection strategy varied by vehicle: The Far-Field Sounding (FFS) vehicle released soundings as rapidly as possible (about every 45 minutes) within the inflow at 40-80km from the supercell. The two mobile mesonet vehicles also ocassionally deployed radiosondes while performing transects of the near-field inflow. The lidar vehicle would position itself to capture the transition from the far-field inflow environment to the potentially storm-modified near-field inflow environment and deployed radiosondes in concert with lidar deployments. The horizontal wind profiles obtained by the lidar have been shown to agree well with the canonical radiosonde vertical profiles (Smith et al. 2020).

The observed datasets containing both kinematic (zonal and meridional wind components, from radiosondes and lidar) and thermodynamic (temperature and dewpoint temperature, from radiosondes) observations are compared to WoFS using hodographs, soundings, and vertical profiles. The data from each lidar deployment are presented as stacked plots displaying both components of the observed wind, errors in these components when compared to WoFS, and the rotational velocity of the mesocyclone. A WoFS forecast is said to be good or reliable when the ensemble members enclose the observation.

Previous studies have used large (>100) radiosonde datasets to statistically evaluate model representation of the PBL in convection allowing models (Coniglio et al. 2012, 2013, Evans et al 2018), however this study uses a case study approach with small radiosonde sample sizes (<10) to inspect WoFS forecasts of PBL characteristics in rarely observed supercell inflow environments. While the observational sample size is relatively low in this study, the vertical profiles of the dynamic and thermodynamic quantities obtained during TORUS provide a unique opportunity to evaluate how a convection-allowing modeling system predicts storm modification of the ambient environment.

3.3 Quality Control

Vaisala applies proprietary filters to the raw radiosonde data to produce the profiles used in this study as truth. Each sounding also was inspected manually by TORUS PIs to ensure data consistency and reliability. Observations collected outside of the inflow to the target supercell or any observations prior to WoFS forecasts were not considered. The inflow region is defined by the region where environmental wind direction points towards the path of the supercell. Radiosondes are carried by the mean flow and can cover >50km in horizontal distance during their float to the tropopause. Considering WoFS outputs convective parameters on a grid fixed to the ground, balloon drift and environmental variability are accounted for by comparing the observed values to a distribution of modeled convective parameter values from an 18 x 15 km grid north of the observation and centered zonally(Fig. 3.3.1). In general, the winds change direction with height, but there is a strong southerly component to the wind throughout most of the atmopshere across all three cases. This motivates the meridionally symmetric- and northern selection of the WoFS grid points used in the parameter analysis.

The lidar data were quality controlled with a signal-to-noise ratio filter, typically leaving the first available data at around 60 meters AGL and terminating somewhere below 2000 meters AGL (due to loss of scattering particles or the presence of cloud water, which quickly attenuates the lidar pulse). Both lidar and radiosonde data sets are resampled at the height (pressure) corresponding to the vertical levels in the WoFS for kinematic (thermodynamic) quantities using a 100-meter averaging window (e.g. data are averaged from 150 to 250 meters to compare to a vertical grid point at 200 meters) in order to create observational data sets comparable to the WoFS vertical grid. This averaging also avoids erroneous errors

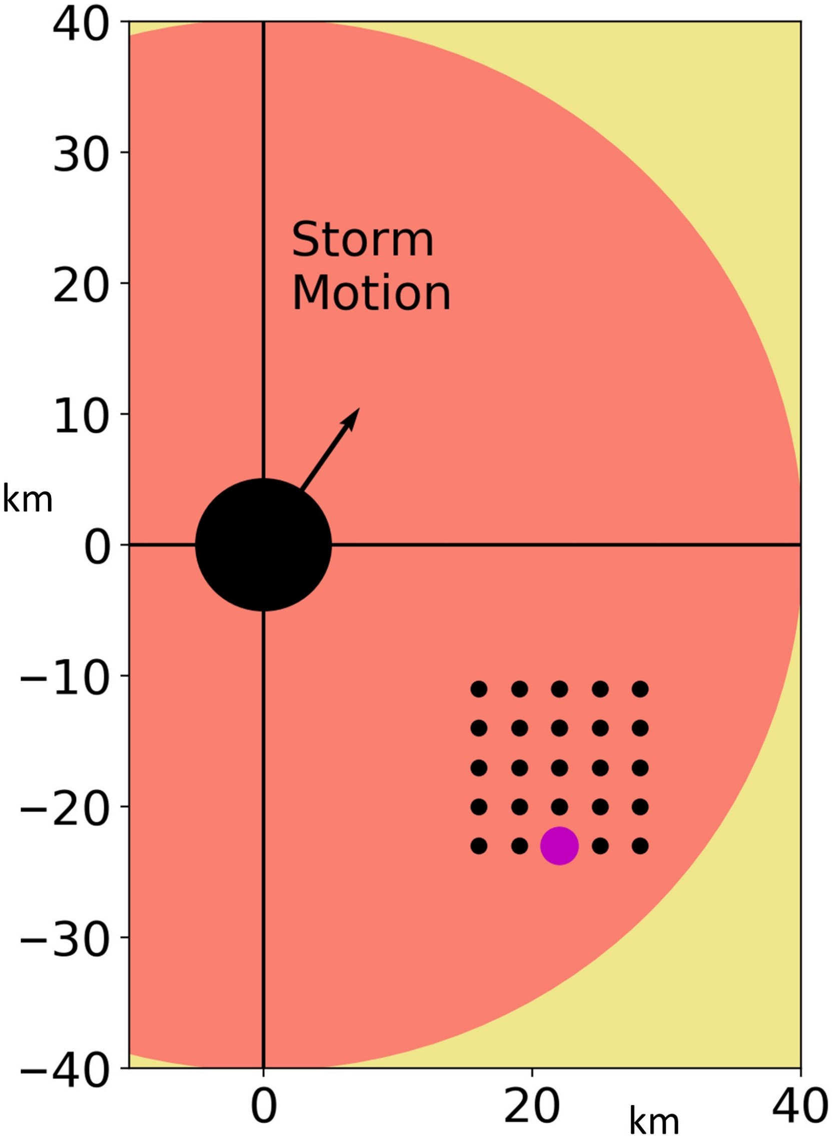

Figure 3.3.1: The smaller black dots represent all the WoFS grid points included in the convective parameter comparisons. The magenta dot represents the nearest WoFS grid point to the near-ground location of the sounding observation. The large black dot represents the center of the storm. The salmon filled circle shows distances from the storm within 40 km, yellow is outside 40 km.

from noise that would contaminate a point-to-point comparison.

3.4 Storm-relative Analysis

The WoFS model output evaluated in this study was produced during the 2019 NOAA Hazardous Weather Testbed Spring Forecasting Experiment (Clark et al. 2012, Gallo et al. 2017). The forecast initialization and valid times are chosen by selecting the nearest forecast valid time to the observation, then selecting the nearest associated initialization time, provided that the valid forecast is between 15(WoFS takes 15 minutes to commute the forecast) and 45 minutes after the initialization time (e.g. a 2236 UTC observation is compared to a WoFS forecast initialized at 2200 UTC and valid at 2235 UTC). This method was used because the forecast is nearest to the observation temporally, resulting in a maximum time difference of 2.5 minutes.

The 18 members in WoFS predict storms that vary in location and strength and thus vary in relation to the location and strength of the observed storm. Because of these variations in modeling storm location, pulling the WoFS grid point nearest to the latitude and longitude of the observation will potentially yield errors caused more by storm location than errors in the environment. Therefore, a storm-relative analysis is employed in this study to provide a consistent comparison between WoFS output and observation.

The storm-relative position within the model is determined by calculating the zonal and meridional displacement from the real storm to the observation, then adding the displacement to the location of the modeled storms. In order to do so, the location of the storms in each of the 18 members and the location of the real storm must be found at every forecast time of

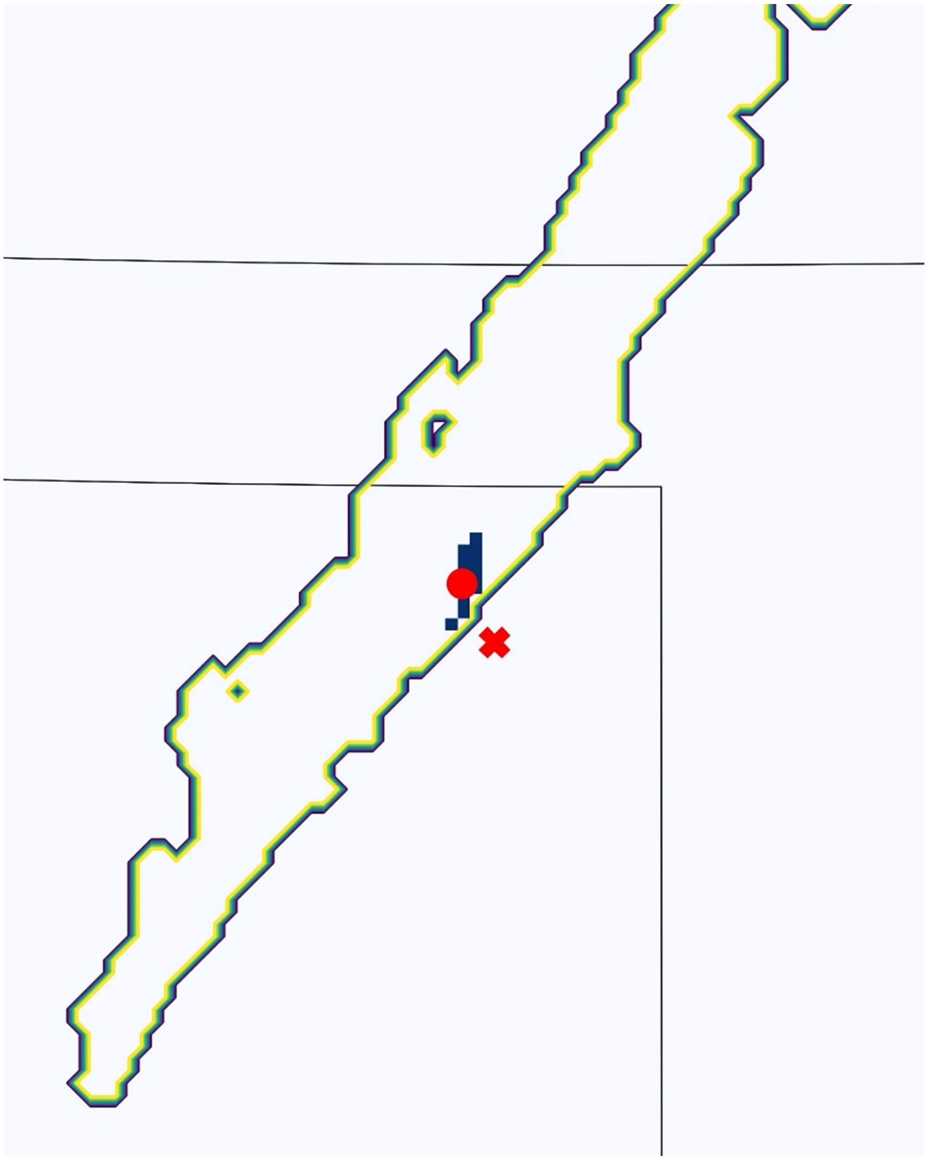

Figure 3.4.1: WoFS storm location (red circle) compared to observed (red X). Member 18 of 17 May 2019 WoFS 0000 UTC forecast, valid 0030 UTC. The blue pixels show the grid points where UH is greater than 50 m^2s^{-2} and corresponds to the storm object. The contoured area is the 3-hour WoFS UH swath of values greater than 5 m^2s^{-2}. Grey lines are the Texas-OK, OK-Kansas borders.

interest. In order to find the hundreds of modeled storm locations, two algorithms used by Britt et al. (2020) were adapted for this study. The first algorithm isolates the 3- hour swath UH object and the second algorithm computes the centroid of updraft helicity (UH) objects (5-minutes objects) as a proxy for mesocyclone location. UH swath objects are defined by a contiguous region of >50 m^2s^{-2} whereas the individual UH objects use a lower threshold of 5 m^2s^{-2} . A lower threshold is used for the individual UH objects so that weaker storms can be located. The first script isolates 3-hour UH swath objects, then the second allows the user to manually find the individual UH object nearest the real storm (Fig. 3.4.1). The location of the real storm was determined using data from the nearest WSR-88D within the GRLevel3 software to pull the latitude and longitude from the location of the velocity couplet.

Once the storm-relative location is determined in all ensemble members, a model sounding is extracted from the WoFS output for each time needed for the comparison to observations. Environmental variables are extracted from the grid mentioned previously, while wind, temperature, and dewpoint values are extracted from the single storm-relative grid point. This processes uses the SHARPpy library (Blumberd et al. 2017). This sounding contains the kinematic and thermodynamic variables discussed previously. The data are then compared to the resampled and averaged observation data and differences are calculated (model – observation) for every member at every vertical grid point for which observational data are available.

4 Case Studies

4.1 Overview of the 17 May 2019 McCook, Nebraska, Tornadic Supercell

The 17 May 2019 McCook, Nebraska tornadic supercell was observed by TORUS and two NEXRAD radars at Goodland, Kansas (KGLD, Fig. 4.1.1, WoFS, Fig. 4.1.2) and North Platte, Nebraska (KTLX). Weak convection initiated at 1830 UTC on a dryline paralleling the Colorado-Kansas border 30 miles south of I-70 and evolved into a supercell over Goodland, Kansas by 2100 UTC. The target supercell then moved at an average heading and speed of 210 degrees and $\sim$ 20 ms^{-1} and produced multiple tornadoes (27 tornado storm reports; Storm Prediction Center) from 2240 to 0120 UTC (ranging from EF0 to EF3).

This case study focuses on the one available lidar deployment (8 far-field, 3 near-field comparable observation times) and 5 radiosonde observations (1 far-field, 4 near-field; Fig. 4.1.4). Of the 5 radiosonde observations, 2 ascended to the equilibrium level (EL) and can be used to compare the observed CAPE to WoFS predicted CAPE. Hereafter, references to the observation-WoFS forecast pairs will appear as: radiosonde observation time, valid WoFS forecast time used in comparison (e.g. 2302,2300).

WoFS possessed a southwestern displacement error in storm object location during the lidar deployment on 17 May (Fig. 4.1.3). The mean zonal error is near constant around 8 km, while the mean meridional error is near zero initially but becomes -10 km. The v-component of Bunker's storm motion vector is consistently smaller than observed, which is consistent with the southerly error of storm objects in WoFS. However, the storm motion vector error is nearly zero in the 2302, 2300 UTC pair and suggest the error in storm object location may have other contributions besides storm motion. Also, it is possible the storms in WoFS are not following the Bunkers motion.

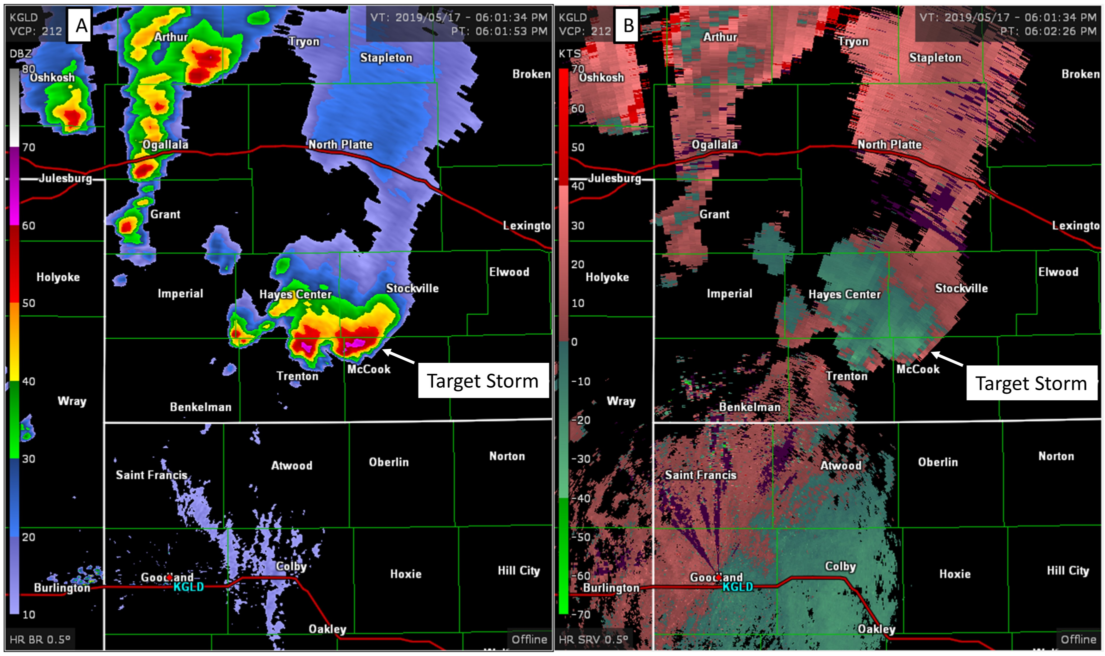

Figure 4.1.1: Radar images from KGLD of the 17 May McCook, Nebraska supercell at 2300 UTC, the time of the McCook tornado report. Panel A shows reflectivity (dBZ); Panel B shows storm-relative velocity (kts).

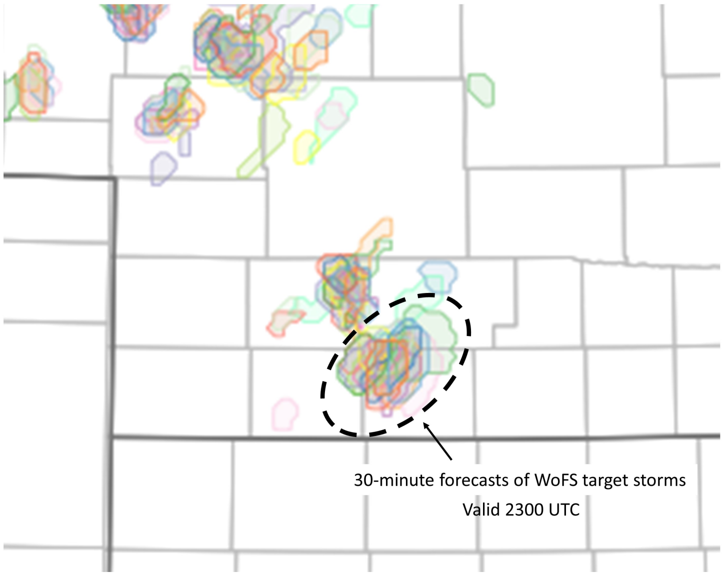

Figure 4.1.2: The dashed oval encompasses contours of 45 dBZ simulated composite reflectivity from 30-minute forecasts from all 18 WoFS members valid at 2300 UTC and initialized at 2230 UTC on 17 May. Different color shading depicts different ensemble members.

4.1.1 Radiosondes

4.1.1.1 Thermodynamics WoFS ensemble mean over forecasts the magnitude of MLCAPE and SBCAPE in both the near-field 0106,0105 UTC and far-field observation 2302,2300 UTC (Fig. 4.1.5). The CAPE decreases throughout the evening as seen in the observations 2302 and 0106 UTC. This reduction of $\sim$ 300 Jkg^{-1} is well forecasted in WoFS, however the over forecast stays about the same for both observations at $\sim$ 500 Jkg^{-1}. The YSU scheme has the smallest over forecast by PBL scheme, which are less than 300 Jkg^{-1}, while both MYJ and MYNN over-forecasts are greater than 500 Jkg^{-1}.

The soundings comparisons (Figures 4.1.6-4.1.9) show that WoFS errors in temperature are typically <2 K throughout the low- to mid-troposphere. For dewpoint, while the errors in the PBL are also typically ¡2K, they can be quite large in the free atmosphere (10-20

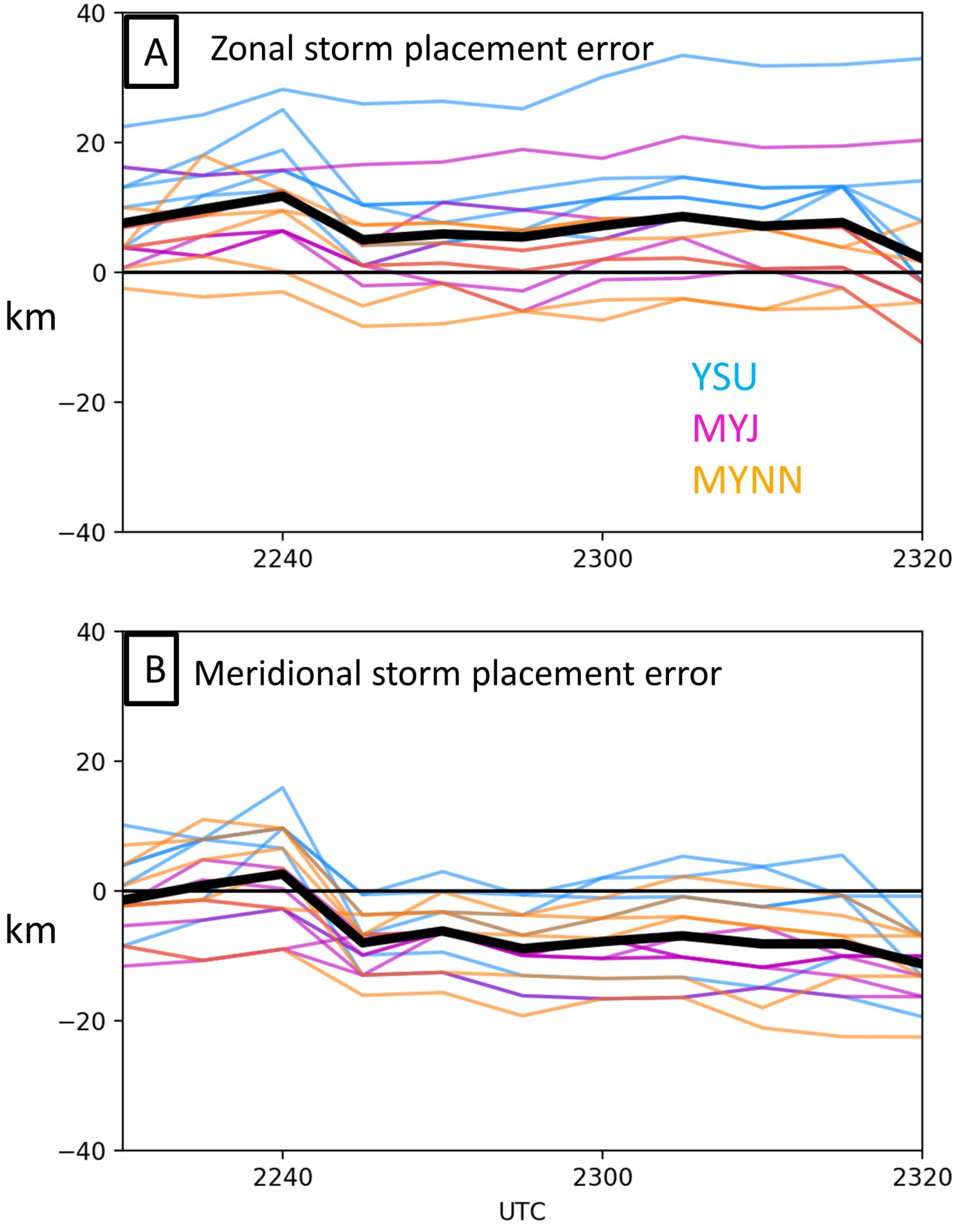

Figure 4.1.3: WoFS storm UH object placement errors (km) during the period of the lidar deployment on 17 May 2019. Panel A displays zonal placement error, Panel B displays meridional placement error. Ensemble mean is black, YSU is blue, MYJ is magenta, and MYNN in orange.

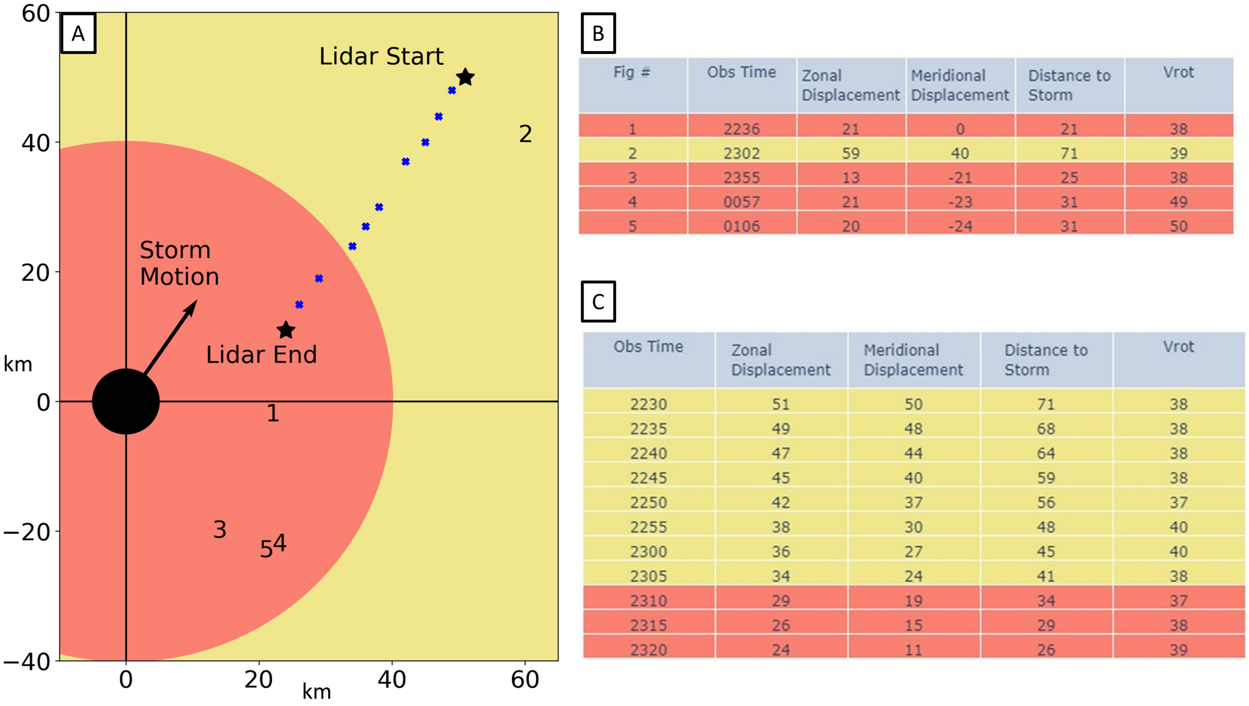

Fig #	Obs Time	Zonal Displacement	Meridional Displacement	Distance to Storm	Vrot
1	2236	21	0	21	38
2	2302	59	40	71	39
3	2355	13	-21	25	38
4	0057	21	-23	31	49
5	0106	20	-24	31	50

Obs Time	Zonal Displacement	Meridional Displacement	Distance to Storm	Vrot
2230	51	50	71	38
2235	49	48	68	38
2240	47	44	64	38
2245	45	40	59	38
2250	42	37	56	37
2255	38	30	48	40
2300	36	27	45	40
2305	34	24	41	38
2310	29	19	34	37
2315	26	15	29	38
2320	24	11	26	39

Figure 4.1.4: Storm-relative locations of observations collected on 17 May used in this study. Panel A displays storm-relative radiosonde (numbers) and lidar (stars and x's) observation locations. Panels B and C display the 5 radiosonde and lidar times, storm-relative coordinates and distance, and rotational velocity of the targeted mesocyclone. In all panels, observations made farther than 40 km from the storm (far field) are shaded in yellow; Observations made closer to the storm are shaded in red (near field). Units of zonal displacement and distance to storm are in km and the rotational velocity of the mesocyclone, a proxy for supercell strength, is measured in ms^{-1}.

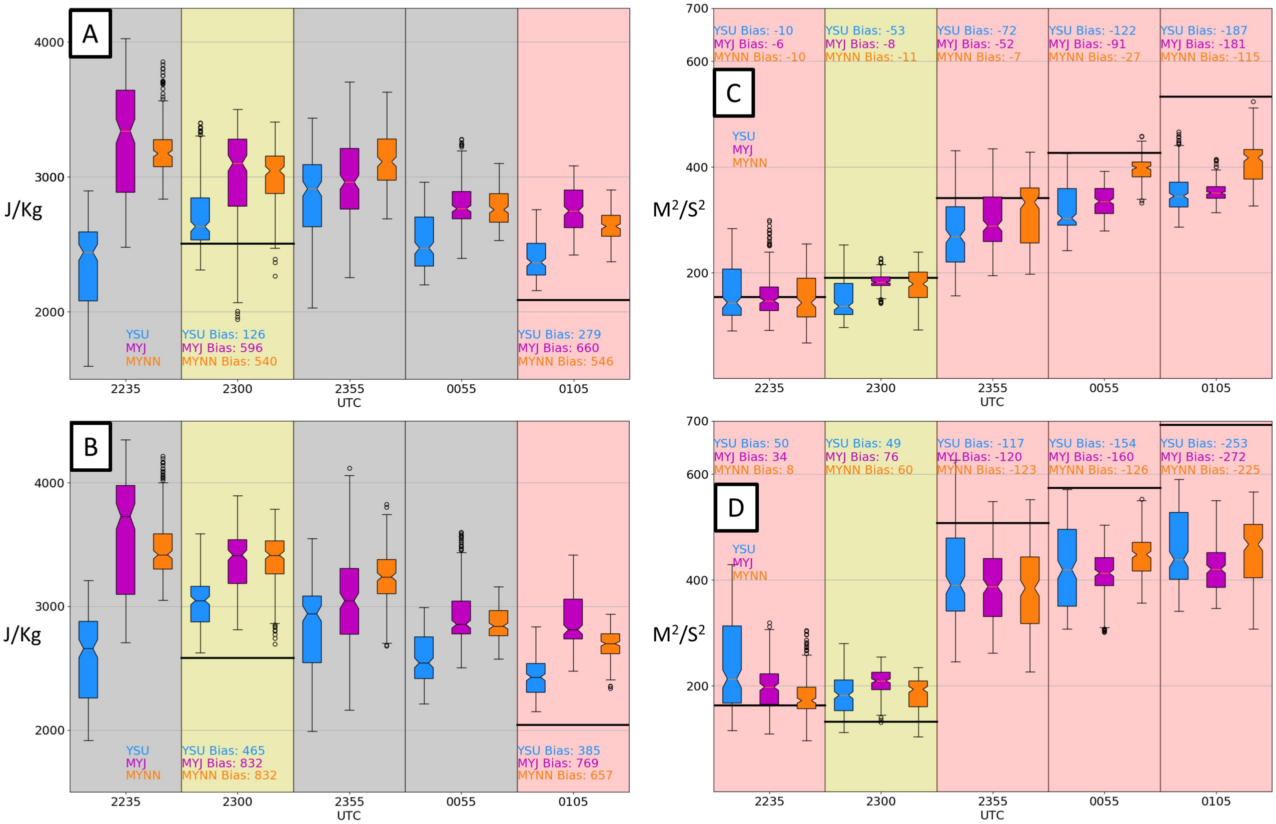

Figure 4.1.5: Box and whisker plots of (A) MLCAPE, (B) SBCAPE, (C) 01SRH, and (D) 03SRH values collected over all horizontal grids points within 15 km grid to the north and 9 km to the east and west of the radiosonde observation (Fig. 3.2.1). The times listed on the horizontal axis are the WoFS forecast used to compare to the respective observation. Observation times are listed in Fig. 4.1.4B. Box plots are color-coded based on PBL scheme: YSU is blue, MYJ is magenta, and MYNN in orange. The nearest forecast times are used for comparisons (e.g. WoFS forecasts initialized 2000 UTC valid at 2235 UTC for an observation at 2236 UTC; observation-WoFS pairs are shown in the format of radiosonde(WoFS). Radiosondes 2236(2235),2355(2355), and 0106(0105) did not reach the EL so the respective CAPE plots are shaded grey and do not include an observed value, which are displayed as a horizontal black bar. PBL scheme errors are labeled. In all panels, observations made farther than 40 km from the storm(far field) are shaded in yellow; observations made closer to the storm are shaded in red.

K). All of the observed near-surface temperatures fall within the envelope of the WoFS members, implying WoFS predicted a high probability of the observation occurring. The YSU scheme consistently predicts the warmest and driest PBLs. The observed temperature inversion between 800 and 700 hPa in all but the the 2236 UTC sounding is also enclosed by the envelope of WoFS members, with the YSU scheme possessing the smallest errors in temperature($<$1K) near the observed location of the inversion. Typically MYJ and MYNN forecast too warm of an inversion. As the inversion lowers later in the evening (0106 UTC), the differences between members become noticeably smaller with the YSU scheme still forecasting cooler temperatures than the MYJ and MYNN schemes. In all four comparisons the non-local YSU and local MYJ and MYNN schemes are behaving as anticipated, with the non-local scheme forecasting a drier, warmer, and more mixed boundary layer (Cohen et al. 2015, 2017).

The dewpoint temperature errors are sensitive to the location of a dry layer evident in the observations from 700-500 hPa at 2302 and 550- 350 hPa at 0106 UTC. The WoFS members enclose the observed dewpoint temperature at most altitudes, but does so only through large spread with the range among the members of $\sim$ 25 K. The YSU members over predict the dewpoint, while the non-local schemes have an mean error near zero at 650 hPa. The ensemble absolute errors are larger in dewpoint temperature in the dry layer at 400 hPa in the 0105 UTC forecast than in the 2300 UTC forecast, likely related to the dryness of this layer, but WoFS still manages to contain the observation in the member envelope, with MYJ members possessing the smallest errors.

The observed profile saturates at 250 hPa, likely as the radiosondes reach the anvil of the storm, but this is not forecasted in WoFS by any members(identified with simulated satellite). The under forecast of an anvil should result in warm PBL temperature error as a result of increase surface heating, however the ensemble still encloses the the observation. This may suggest there is a source of a cool PBL error balancing the over prediction of surface heating.

WoFS over forecasted both SBCAPE and MLCAPE on 17 May. The YSU scheme posted the lowest CAPE errors, a cooler, more representative temperature inversion, and a warmer, drier PBL. The WoFS ensemble average for the 2300 forecasted posted nearly zero error, with the 18 members well enclosing the observation.

4.1.1.2 Kinematics All 5 radiosondes ascended above 3 km so 0-1 km and 0-3 km SRH(01SRH and 03SRH, respectively) comparisons are available in Fig.4.1.5C,D. WoFS forecasts of 01SRH and 03SRH for the earliest observation time (2236,2235) are excellent with mean errors <10 m^2s^{-2}, among all three PBL schemes. In contrast, WoFS under forecasts both 01SRH and 03SRH substantially in the latest three observations (2355, 0057, 0106 UTC), particularly for the YSU-scheme members. WoFS appears to be under forecasting SRH in near-storm soundings, but this is contradicted with the early observation, which is also near-storm, where WoFS has much smaller errors. The dependence of 17 May WoFS SRH errors therefore be more a function of the supercell life cycle than of distance from the storm; the 2236 UTC observation was made relatively early in the storm life cycle.

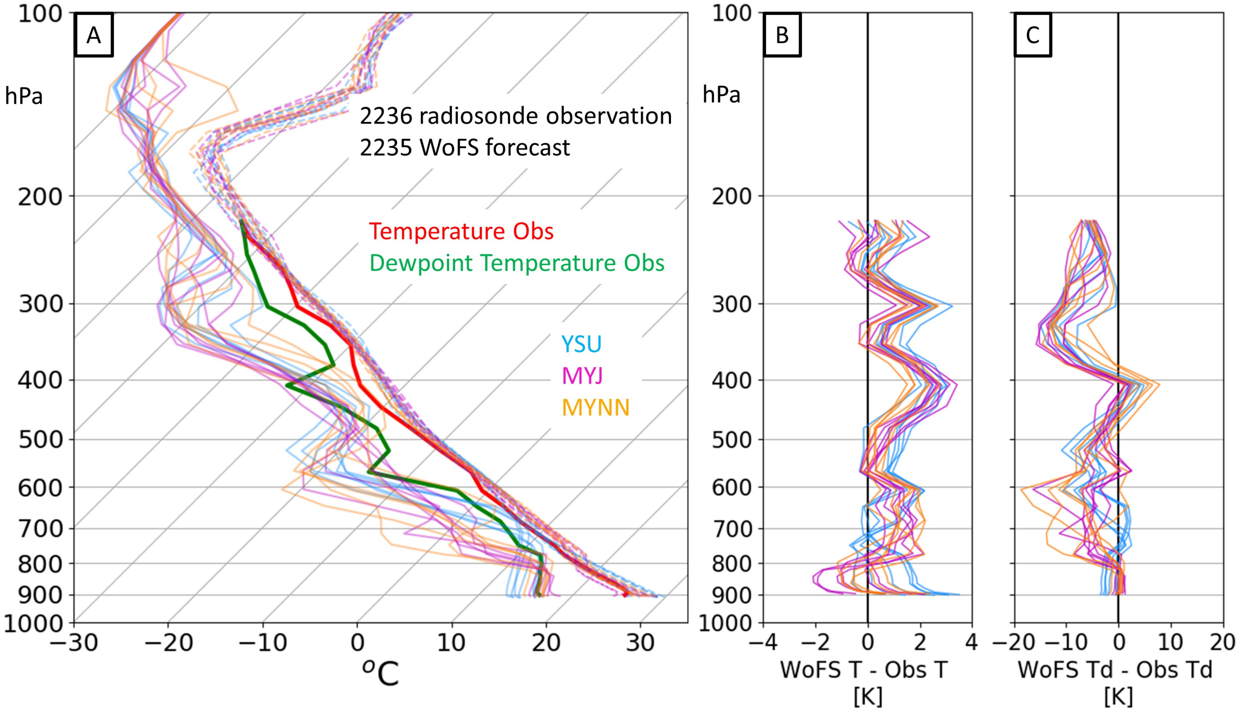

Figure 4.1.6: Panel A is a sounding of the 2236 UTC radiosonde launch compared to the 2235 UTC WoFS forecast, initialized at 2200 UTC on 17 May 2019. The red and green bold lines are the observed temperature and dewpoint temperature, respectively. Panel B and C display vertical profiles of the error in both potential temperature and dew point temperature in K. Members are color-coded based on PBL scheme: YSU is blue, MYJ is magenta, and MYNN in orange.

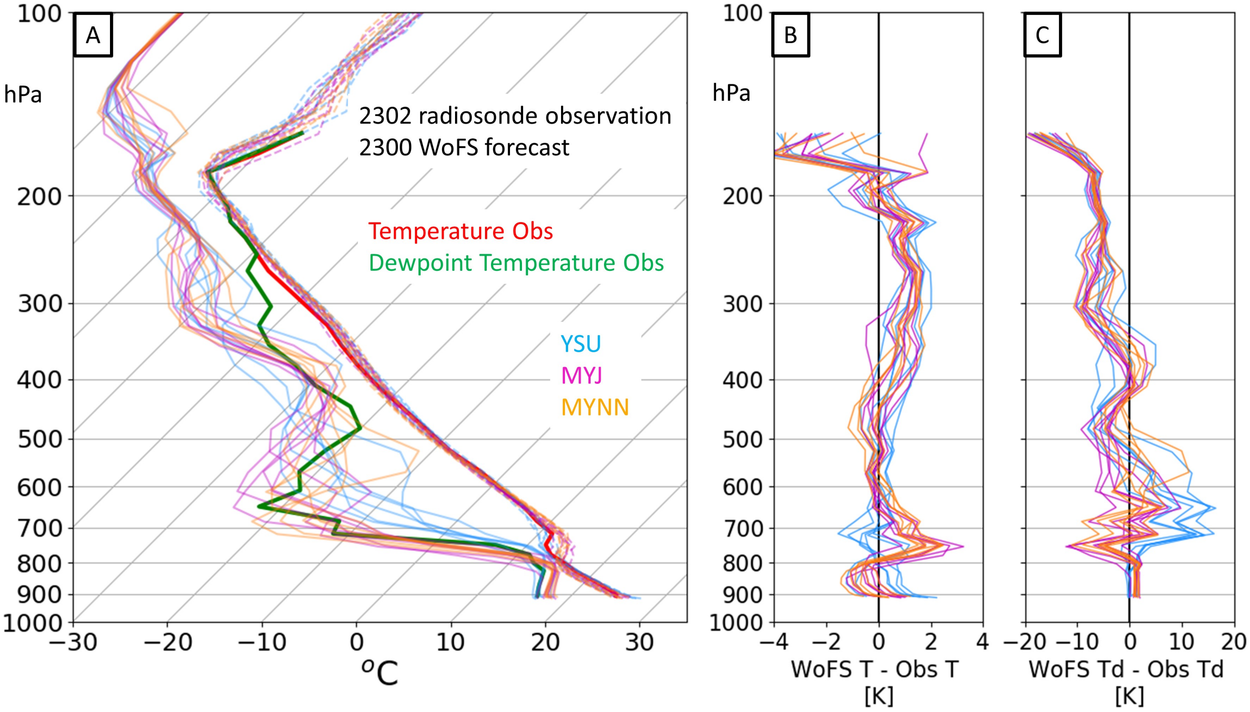

Figure 4.1.7: As in Fig 4.1.6, except for the 2302 UTC radiosonde launch compared to the 2230 UTC WoFS forecast, initialized at 2300 UTC on 17 May 2019.

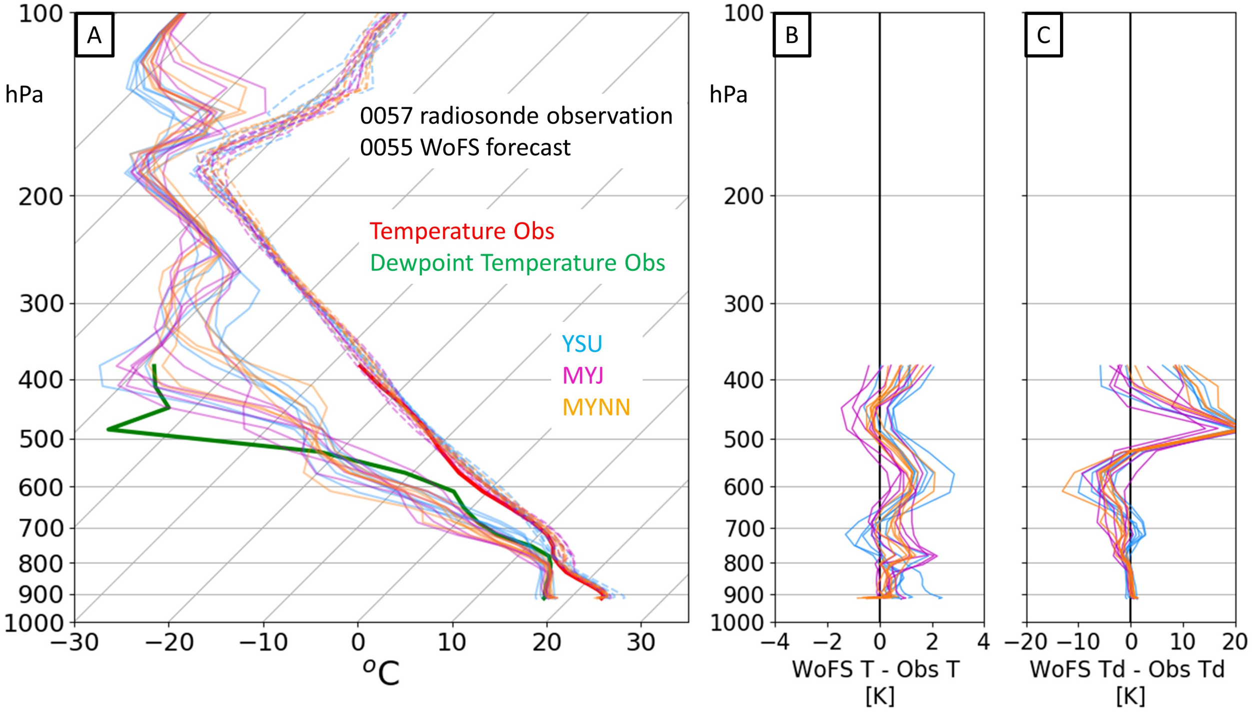

Figure 4.1.8: As in Fig 4.1.6, except for the 0057 UTC radiosonde launch compared to the 0055 UTC WoFS forecast, initialized at 0030 UTC on 17 May 2019.

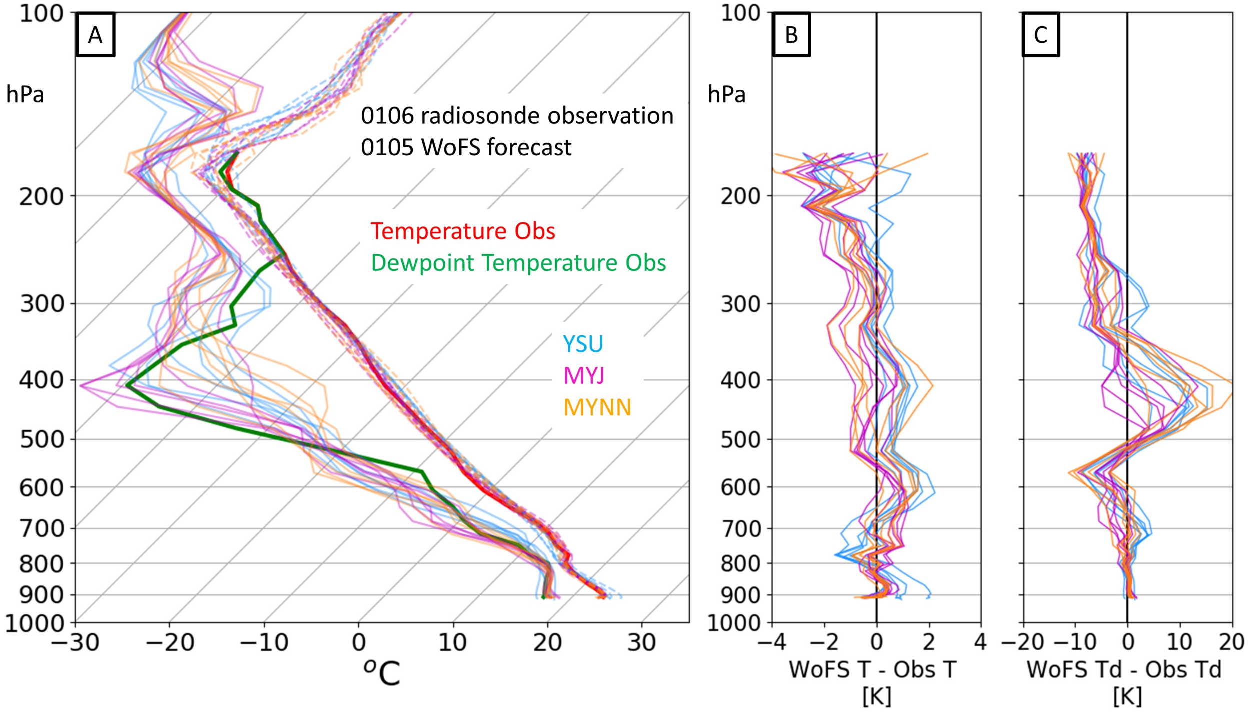

Figure 4.1.9: As in Fig 4.1.6, except for the 0106 UTC radiosonde launch compared to the 0105 UTC WoFS forecast, initialized at 0030 UTC on 17 May 2019.

From a storm modification perspective, the mean WoFS 01SRH and 03SRH values increase with time as do the SRH values obtained observationally. However, the errors grow with time along with the absolute values of SRH. This suggests that the wind field in the WoFS forecasts is responding too weakly to the presence of the storm. In other words, WoFS does increase the wind speed in the lower levels with time, but not to the same degree as seen in the observations. Comparing the early, near-storm 2236,2235 and the later 0106,0105 observation-WoFS pairs (Figures 4.1.10, 4.1.12), the storm-relative winds (panel C) in WoFS are not as strong as in the observation at the later time. In the 0106 UTC observation (Fig. 4.1.12), the stronger v-component in the observation over the lowest 3 km leads to a negative error in SRH.

MYNN errors in SRH are smaller than the other schemes throughout the day. Although the difference in errors among member are often less than 50 m^2s^{-2}, it is intuitive that the local schemes produce higher SRH values than non-local schemes. In convective boundary-layers, non-local schemes tend to mix out wind-shear more strongly than local-schemes (Cohen et al. 2015); indeed, MYNN and MYJ tend to have stronger low-level wind shear than YSU across the 5 radiosondes, which leads to strong SRH.

WoFS has small errors in SRH in the earliest two observations, but a notable similarity among the later sounding observations is the WoFS under forecasted both the strength of the storm-relative winds and the low-level vertical wind shear, leading to increasing errors in SRH with time. A closer inspection of the storm-relative hodographs shows that this under forecast in storm-relative wind speed and wind shear is caused by a negative error in meridional wind from 1- 3 km. Note that these errors appear to be more dependent on time and storm duration than on distance from the storm.

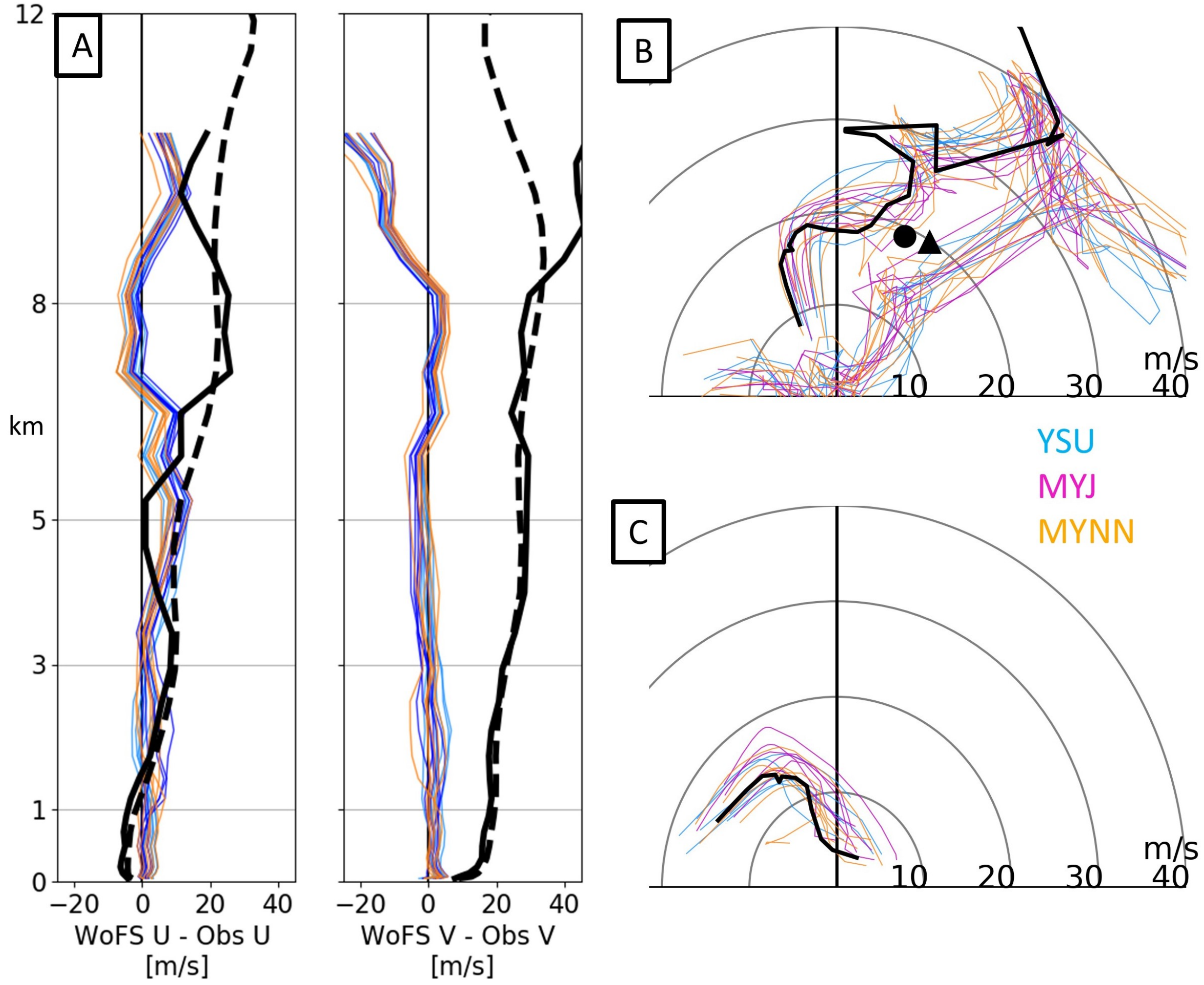

Figure 4.1.10: 2236 UTC radiosonde observation and WoFS forecast initialized at 2200UTC on 17 May 2019, valid at 2235 UTC. (A) Vertical profile of$u$ and$v$ component errors (colors), observed wind (solid black), and WoFS wind (dashed) (ms^{-1}). (B) Ground-relative hodograph of observed (solid black) and WoFS winds, color coded by PBL scheme: YSU is blue, MYJ is magenta, and MYNN in orange. The observed and WoFS storm motion vectors are represented with a dot and triangle, respectively. WoFS storm motion is obstained by averaging over the convective parameter domain. (C) Storm-relative hodograph showing the observed (solid black) and modeled winds(color) up to 3 km AGL.

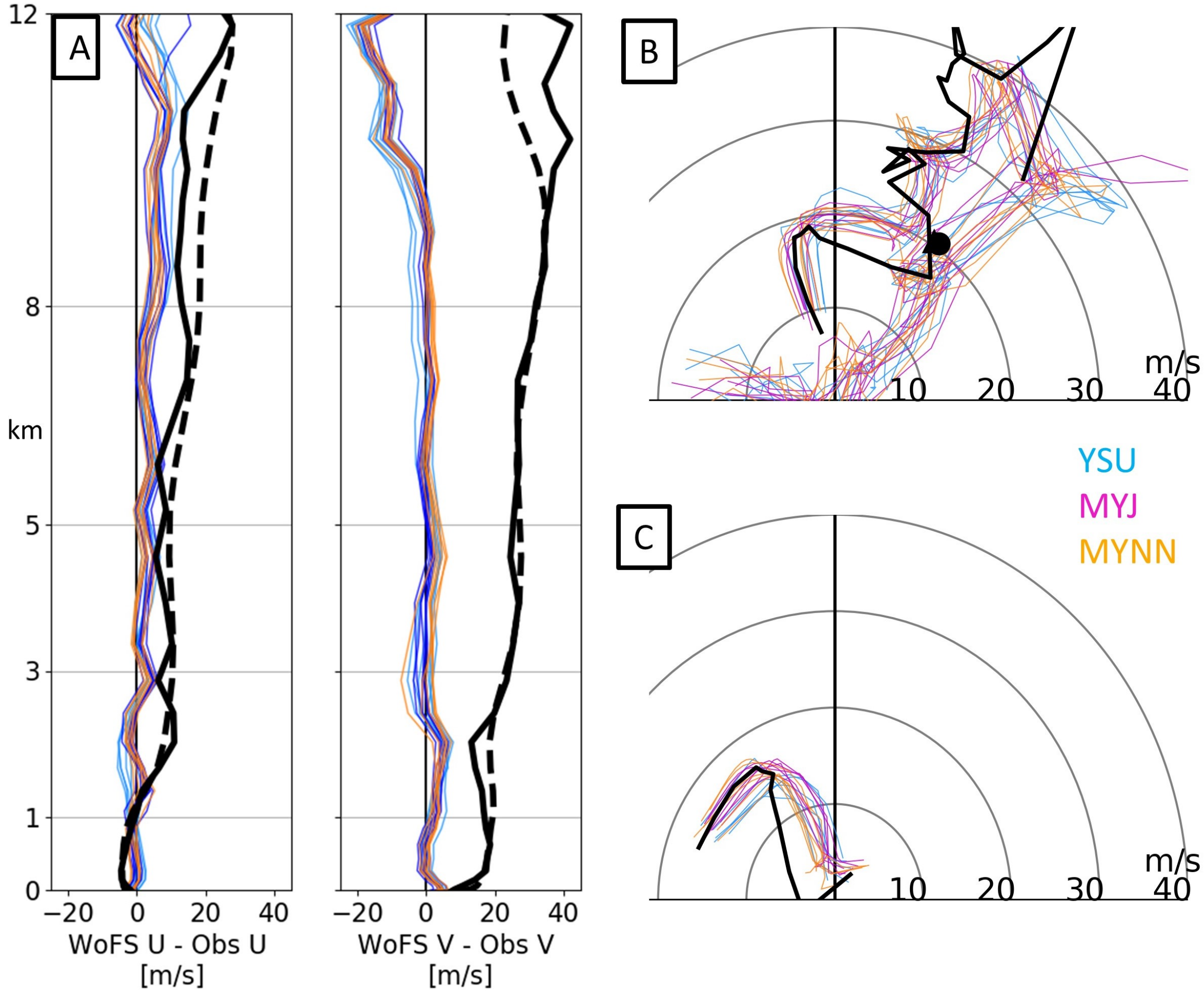

Figure 4.1.11: As in Fig 4.1.10, except for 2302 UTC radiosonde observation and WoFS forecast initialized at 2230 UTC on 17 May 2019, valid at 2300 UTC

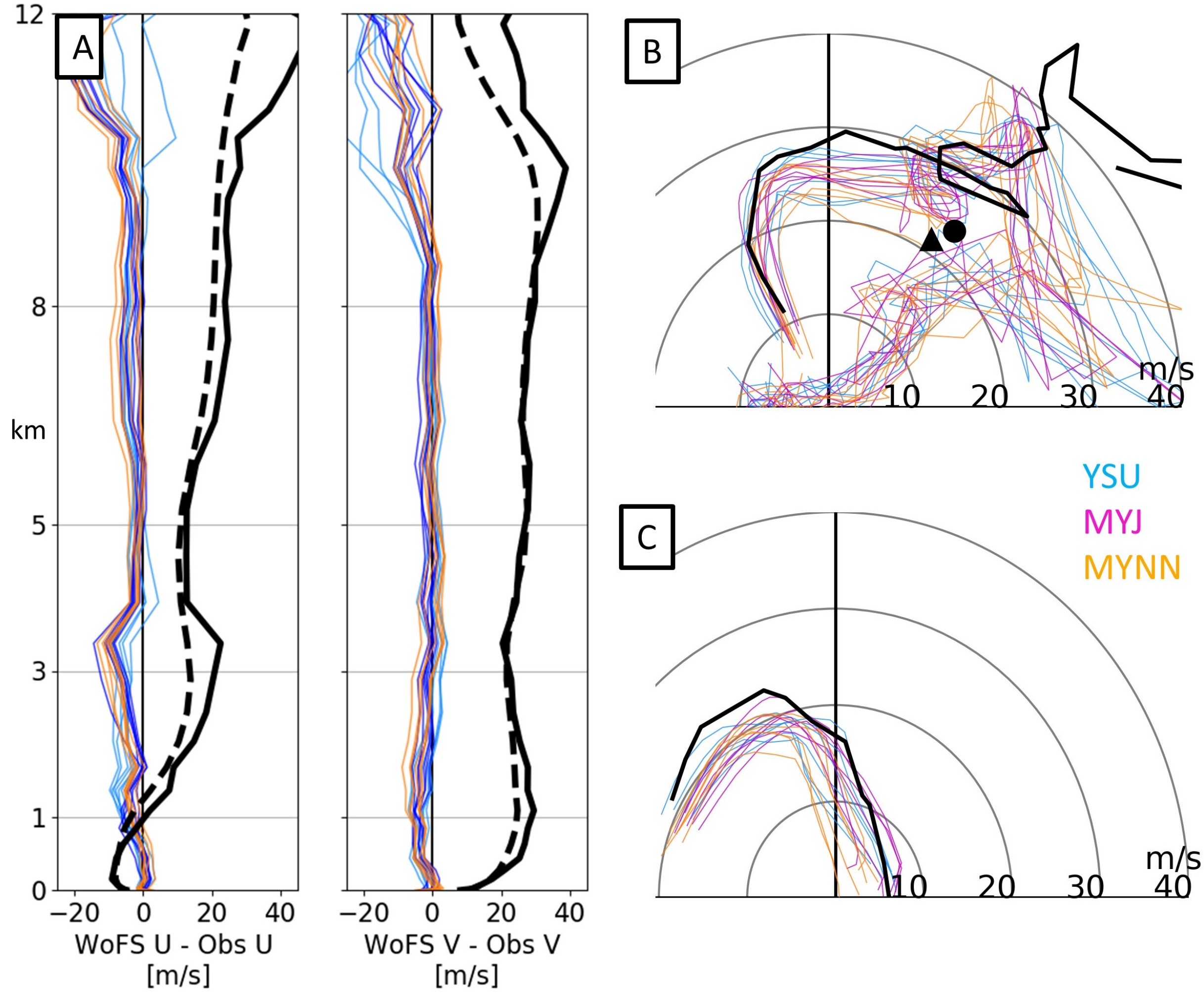

Figure 4.1.12: As in Fig 4.1.10, except for 0106 UTC radiosonde observation and WoFS forecast initialized at 0030 UTC on 17 May 2019, valid at 0105 UTC

4.1.2 Lidar

The only lidar deployment on 17 May collected a 50-minute duration sample of winds in the lowest ∼ 1700 meters AGL from 2230-2320 UTC and observed both near-field and far-field winds as the storm approached the stationary lidar. The winds at all levels were observed to back (turn counterclockwise) as the storm approached the lidar (Fig. 4.1.13). The winds back in WoFS forecasts as well; however, not to the same extent as seen in the observations. At 2230 UTC, WoFS forecasts winds that are more backed in the lowest 500 m than reality (negative u error), but this error becomes positive later in the lidar deployment as the observed winds back more than WoFS winds with the approach of the storm. WoFS winds are generally too strong above 500 m in the v-component by 1-3 ms^{-1}(Fig. 4.1.13Aii).

The error in the u and v-components of the wind may be explained by weaker storm modifications of the inflow environments in WoFS compared to reality. As the storm approaches the lidar, the wind speeds are expected to increase and turn as a response to the impinging low-pressure perturbation caused by the rotating updraft. This response is seen in the backing of the observed winds (counterclockwise turning) and in the reduction of the v-component as the storm-induced low-pressure perturbation pulls the wind-field towards the southwest from the lidar's NE orientation. While WoFS does back winds near the surface, the change in the zonal wind is not more than $\sim$ 3 ms^{-1} during the duration of the lidar deployment and the observed u-component changes by $\sim$ 8 ms^{-1} during the same time. The storm modification signal is present in WoFS forecasts, just not as prominent as in the observation.

Notice that the rotational velocity of the storm is relatively constant through-out the deployment(Fig. 4.1.13Ai). This implies that the errors are not attributable to a time lag between the mesocyclone changing strength and radar velocity data assimilation. The errors here seem to point at a fundamental difference in how WoFS predicts storm modification of the ambient environment: WoFS winds do not back as much as seen in the observation.

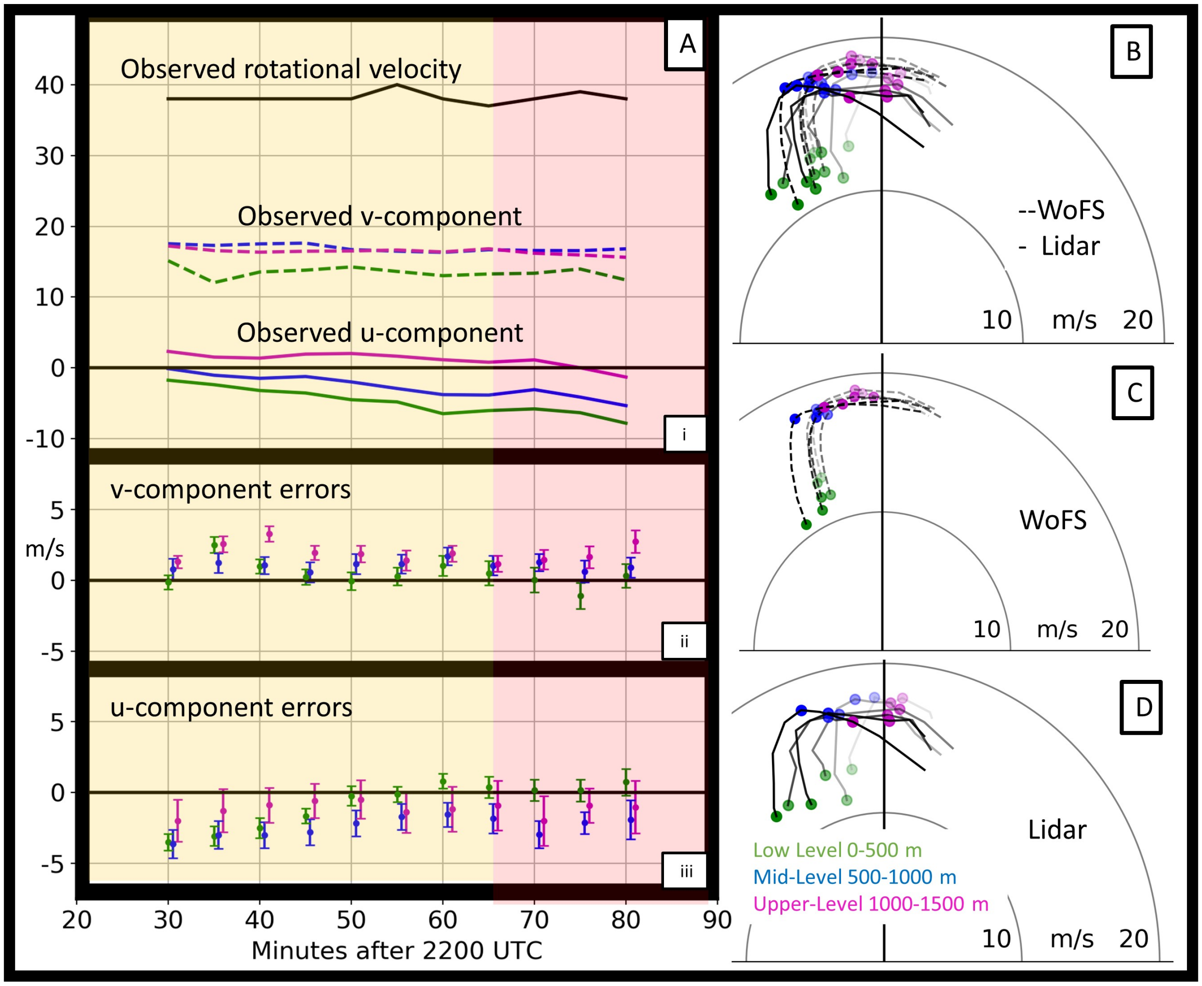

Figure 4.1.13: Hodograph and wind-component errors plotted against time for the lidar observation from 2230-2320 UTC. Panel A displays stacked plots of rotational velocity of the mesocyclone, observed u and v winds components (i), and the error in the v (ii) and u (iii) wind components as a function of time in ms^{-1}. The error bars in the error plots show one standard deviation of all members in the respective level. In all panes, low-level PBL winds, 0-500 meters AGL, are studded with green circles, mid-level PBL winds, 501-1000 meters AGL, are studded with blue circles, and the upper-level winds, 1001-1500 meters AGL are studded with magenta circles. Panel B is a hodograph displaying both the observed and modeled winds every 10-minutes. Panels C and D show only the modeled and observed winds, respectively, for clarity. Times shown in panels B,C, and D are 2230,2240,2250,2300,2310, and 2320 UTC, with times increasing from lighter to darker shades.

4.1.3 17 May Summary

Thermodynamically, the WoFS member envelope enclosed the observed temperature and dewpoint temperature at all levels, except in the regions where the radiosonde entered a cloud at 250 hPa. This indicates that the WoFS ensemble has at least reasonable spread about the observed state. Large dewpoint errors in individual members occurred near the driest portions of the observed profile with errors having magnitudes as large as 20 K. The YSU scheme consistently predicts a warmer and drier PBL, with a weaker upper boundary layer temperature inversion than the MYJ and MYNN members. Also, the profiles above the temperature inversion often show YSU members predicting warmer temperatures than MYJ and MYNN perhaps contributing to smaller errors for YSU in MLCAPE and SBCAPE. All schemes over forecast MLCAPE and SBCAPE.

The radiosondes show the winds backing with time and gaining strength in the meridional direction, with southerly winds increasing at later times (after 0000 UTC). This signal of strengthening meridional winds is intuitive considering the storm-relative location of the later radiosonde deployments: The storm was to the north of the observations, which has the anticipated impact of strengthening the southerly component of the wind due to the northern orientation of the mesocyclone low. The lidar deployment showed the meridional winds slightly decreasing with time, but again this is consistent with the anticipated enviornmental modification by the mesocyclone considering the lidar remains north of the storm throughout the deployment. The observed lidar winds also backed considerably with time as a result of the shortening distance from the mesocyclone. A nearly constant rotational velocity observed in the mesocyclone during this period suggests that change in storm intensity did not play a role in the backing of the winds.

WoFS over forecasts the meridional wind and under forecasts backing before 0000 UTC as seen in the 2236,2235 observation WoFS pair and in the lidar deployment comparison. WoFS accurately forecasts an increase of the southerly winds above 1 km AGL after 0000 UTC, but still under-forecasts the meridional wind speed later in the evening, suggesting that the amplitude of storm modification and potentially the influence of the southerly jet in WoFS must be stronger in order to more accurately predict the observed wind field. The lack of backing and evidence of strengthening meridional wind is reminiscent of the results of the observed storm environment modification for tornadic supercells found in Wade et al. (2018). Interestingly Flournoy et al. (2020) finds that the near-storm environment of supercells simulated using Cloud Model 1 (Bryan et al. 2002) were less backed than in observed near-storm environment. This suggests CM1 and WoFS (using the WRF model) are both under forecasting the magnitude of storm feedback on the environment.

4.2 Overview of the 20 May 2019 Magnum, OK Tornadic Supercell

The supercell that would eventually produce the Magnum, OK tornado at 2210 UTC (Figs. 4.2.1, 4.2.2) initiated $\sim$ 30 km east of Lubbock, Texas at 1700 UTC. This storm tracked ENE and was tornadic as early as 2000 UTC, resulting in a tornado report in Paducah, Texas. TORUS released 11 radiosondes on 20 May, 6 of which were either pre-convection or released before WoFS forecasts were available, leaving 5 radiosonde observations for analysis. The relatively large number of pre-convection soundings were motivated by the high tornado risk as determined by the Storm Prediction Center.

The three earliest radiosonde observations were made in the far field and the two latest were made in the near field (Fig. 4.2.4). TORUS also deployed the lidar twice, the first of which is the longest deployment analyzed in this study, observing both the near and far field from 2030 to 2135 UTC. The second deployment lasted only 20 minutes but the lidar observed the environment within 25 km of the target supercell during the 2210 UTC tornado report in Magnum, OK. WoFS forecasted storms with an increasing southerly error and consistent easterly error from 2030-2135 UTC and 2155-2210 UTC (Fig.s 4.2.1-4.2.3). The storm was observed by the KFDR WSR-88D radar during the time period TORUS observations were made (Fig. 4.2.1).

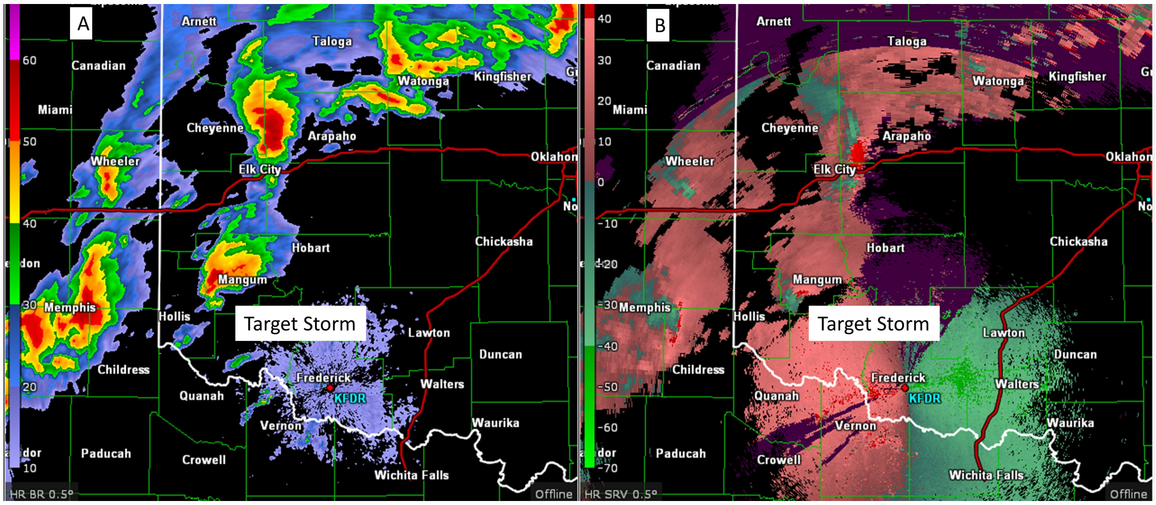

Figure 4.2.1: Radar images from KFDR of the 20 May 2019 Magnum, Oklahoma supercell at 2210 UTC, the time of the Magnum tornado report. Panel A shows reflectivity (dBZ); Panel B shows storm-relative velocity (kts).

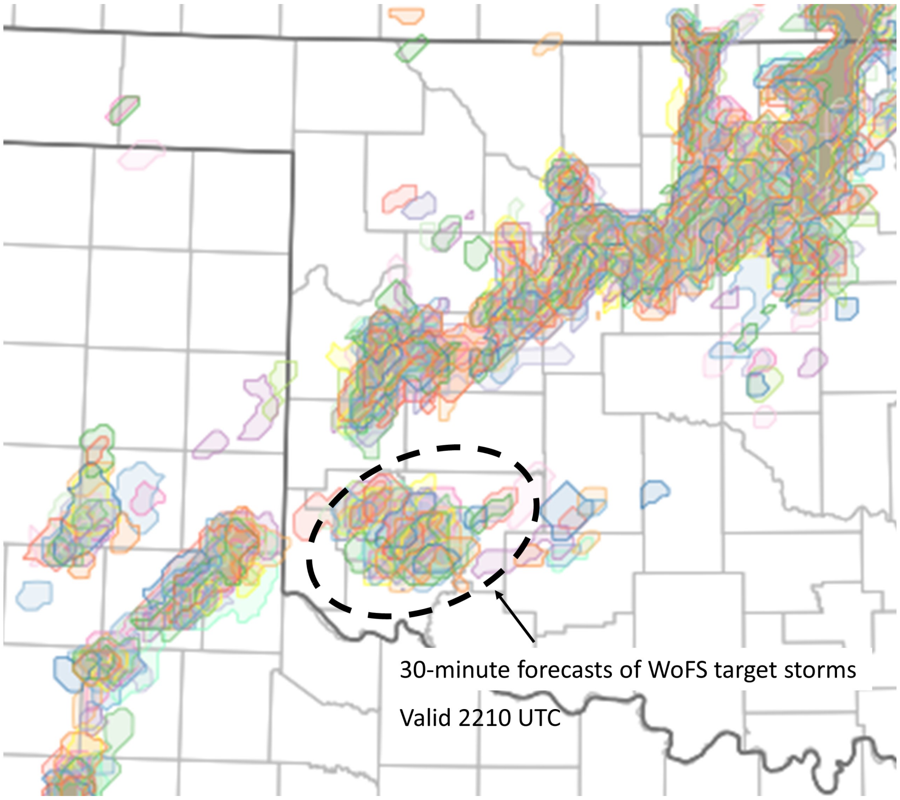

30-minute forecasts of WoFS target storms

Valid 2210 UTC

Figure 4.2.2: As in Fig 4.1.2, except for the target storm on 20 May 2019 forecast initialized at 2130, valid at 2210 UTC

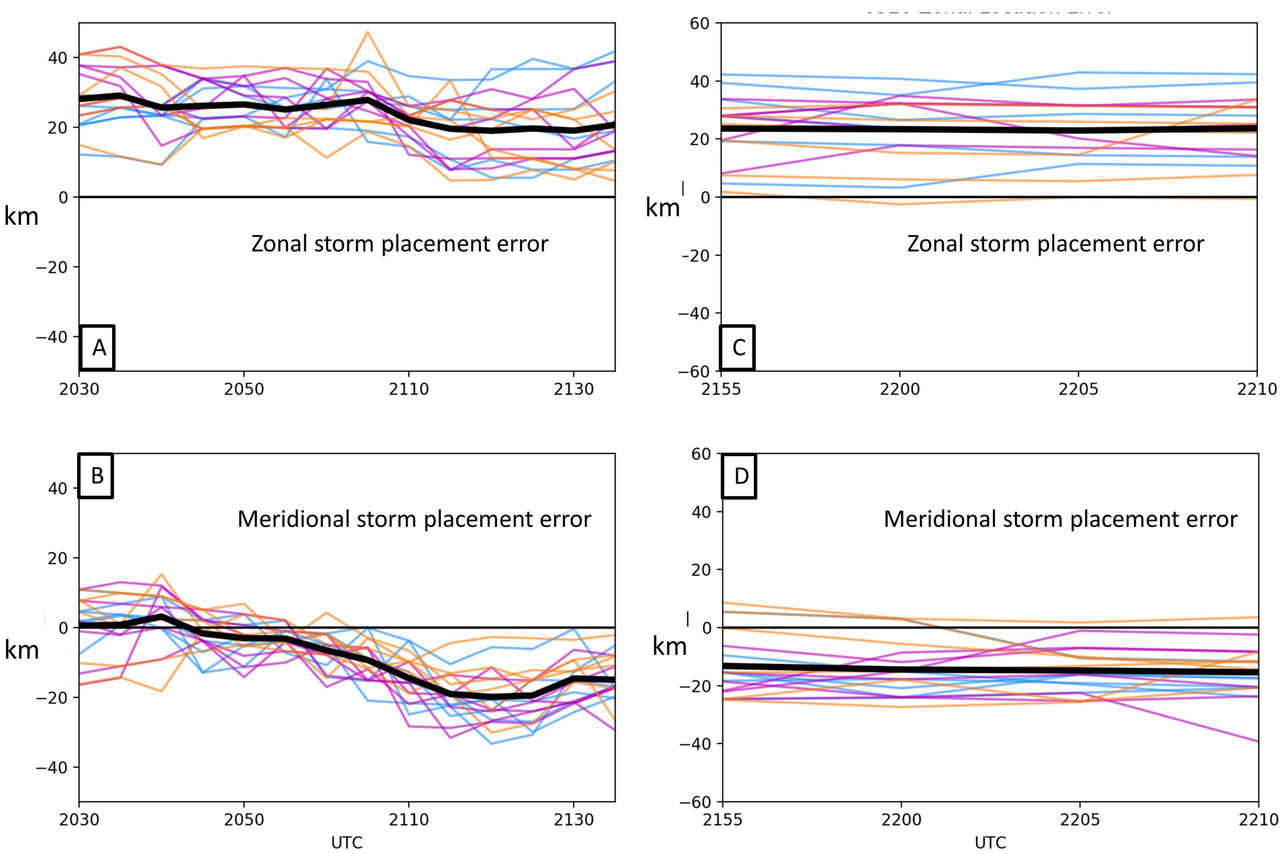

Figure 4.2.3: As in Fig 4.1.3, except for 20 May 2019

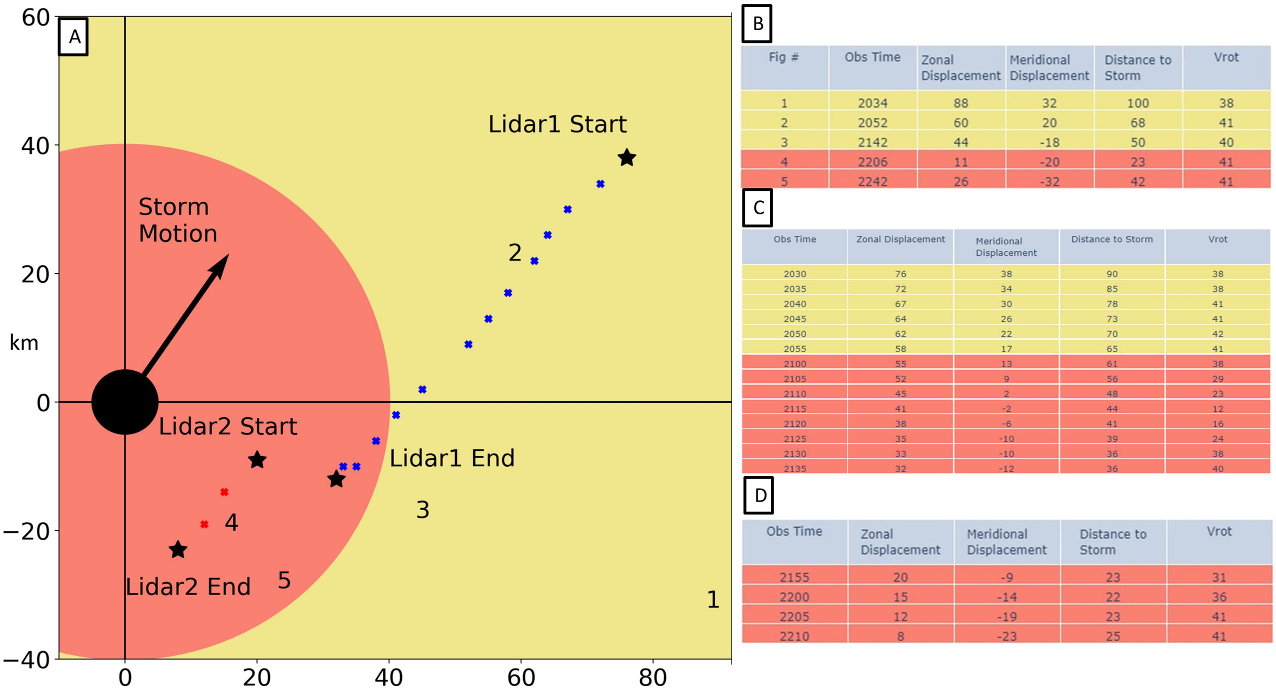

B

Fig #	Obs Time	Zonal Displacement	Meridional Displacement	Distance to Storm	Vrot
1	2034	88	32	100	38
2	2052	60	20	68	41
3	2142	44	-18	50	40
4	2206	11	-20	23	41
5	2242	26	-32	42	41

C

Obs Time	Zonal Displacement	Meridional Displacement	Distance to Storm	Vrot
2030	76	38	90	38
2035	72	34	85	38
2040	67	30	78	41
2045	64	26	73	41
2050	62	22	70	42
2055	58	17	65	41
2100	55	13	61	38
2105	52	9	56	29
2110	45	2	48	23
2115	41	-2	44	12
2120	38	-6	41	16
2125	35	-10	39	24
2130	33	-10	36	38
2135	32	-12	36	40

D

Obs Time	Zonal Displacement	Meridional Displacement	Distance to Storm	Vrot
2155	20	-9	23	31
2200	15	-14	22	36
2205	12	-19	23	41
2210	8	-23	25	41

Figure 4.2.4: As in 4.1.4, except for 20 May 2019

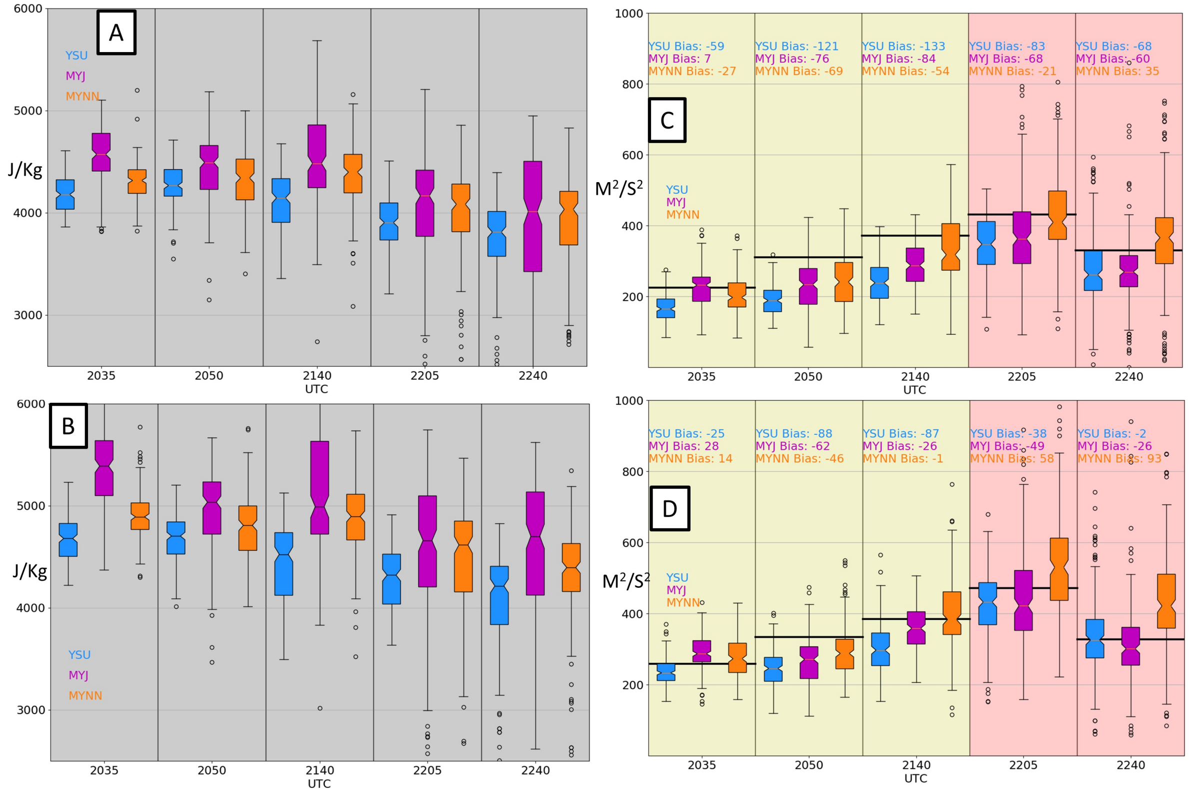

Figure 4.2.5: As in 4.1.5, except for 20 May 2019

4.2.1 Radiosondes

4.2.1.1 Thermodynamics Signal was lost from all five radiosondes as they were ingested into the target supercell at $\sim$ 450 hPa which leaves no CAPE values to compare to WoFS on 20 May. However, box plots of WoFS MLCAPE and SBCAPE are available in Fig.4.2.5, panels A,B to show how the environment around the WoFS storms change throughout the deployment. WoFS decreases the ensemble mean MLCAPE from about 4300 to 3900 Jkg^{-1} and SBCAPE from 5000 Jkg^{-1} to 4500 Jkg^{-1} closer to the supercell. The YSU scheme members often depict lower CAPE than the local members, but the MLCAPE and SBCAPE distributions among the three PBL schemes typically overlap.

WoFS temperature errors in the PBL are less than 2 K in magnitude between the surface and 700 hPa. However, the WoFS forecasts contain a positive surface temperature error at 2035 UTC in most members, up to 2 K in some of the YSU and MYJ members, which may help explain the positive CAPE errors. The 2052,2050 UTC pair also shows a consistent warm error, which is peculiar considering this radiosonde is the farthest observation from the supercell and thus experiences minimal impacts from the storm. This suggests that errors were inherited from the background conditions provided by the HRRR ensemble. Given the presence of clouds from 900-770 hPa reflecting the very moist environment, it is possible that some HRRR members had cloud cover that was too thin and thus had larger insulation than in reality. Also, the dewpoint temperature errors are negative and larger in magnitude for 2050 UTC than 2035 UTC between the surface and 700 hPa, supporting the idea that WoFS is forecasting thinner or no clouds in this layer.

4.2.1.2 Kinematics All radiosondes ascended above 3 km so observed SRH cam be compared to WoFS forecasts of 0-1km SRH and 0-3km SRH as shown in Fig.4.2.5C,D, respectively. For the observation farthest from the storm (2034 UTC), WoFS forecasts both 0-1 and 03SRH quite well with only the YSU members showing values consistently too low. However, a consistent negative bias emerges for the other soundings. These errors appear to have no dependence on distance from or orientation to the target supercell. YSU members typically predict smaller SRH values than the local schemes. MYJ consistently forecasts smaller SRH values than MYNN, an interesting result considering the two schemes are both local.

Panel C in Figures 4.2.8-4.2.10 show the storm-relative hodographs up to 3 km. The observed storm-relative hodograph generally falls within the envelope of the modeled hodographs below about 3 km, which explains the small negative error in SRH, for all radiosonde observations, except the 2206 and 2242 UTC observations. For these, the observed storm speed is ~ 10 ms^{-1} faster than modeled (panel B), which displaces the observed storm-relative hodograph out of the ensemble envelope. However, the dramatic difference in storm motion does not manifest as a large SRH errors because the v-component of the modeled storm-relative winds is larger than observed. In other words, the boost in SRH in the 2206 and 2240 UTC observations results from a larger u-component, whereas the SRH values that would otherwise be lower from a small u-component are maintained somewhat by a v-component of the storm-relative wind that is larger than observed (SRH errors are not too large for somewhat incorrect reasons). The < 2 ms^{-1} errors in storm motion as seen in the first three radiosonde observations does not explain the relatively consistent SE storm object error in WoFS (Fig.

4.2.3). Again, this suggests the storms forecasted by WoFS are not following the Bunkers motion.

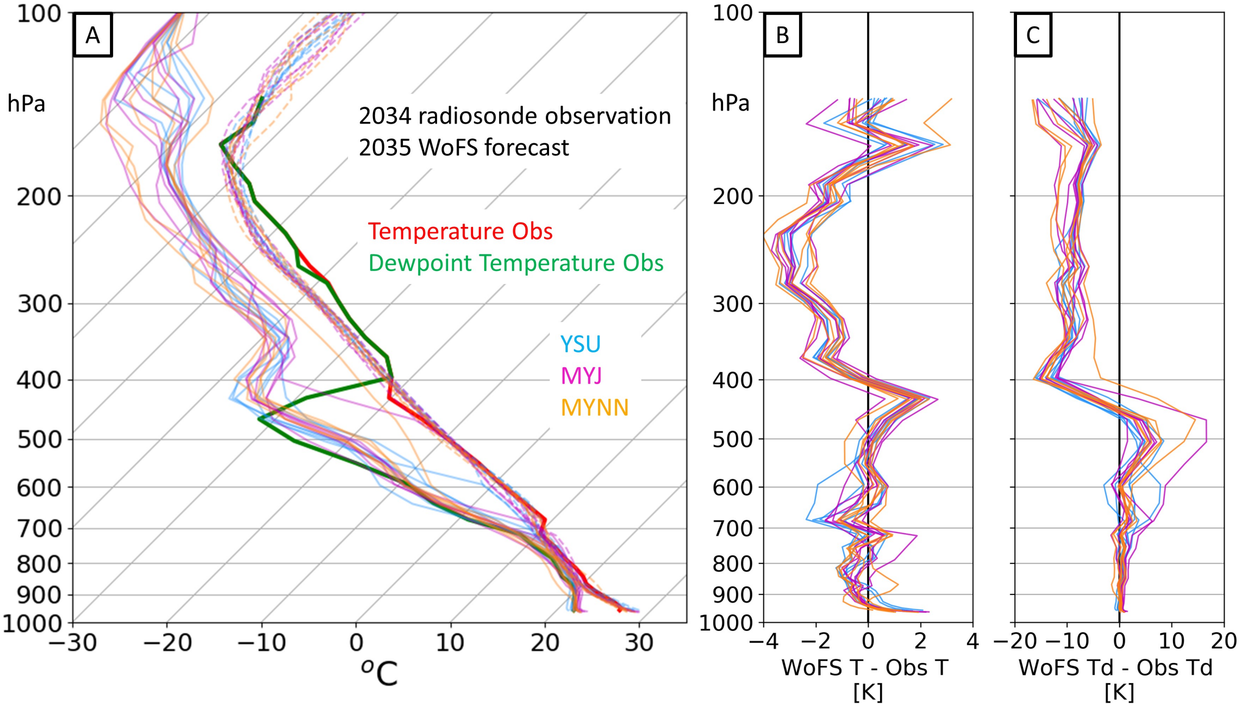

Figure 4.2.6: As in Fig 4.1.6, except for the 2034 UTC radiosonde launch compared to the 2035 UTC WoFS forecast on 20 May 2019, initialized at 2000 UTC.

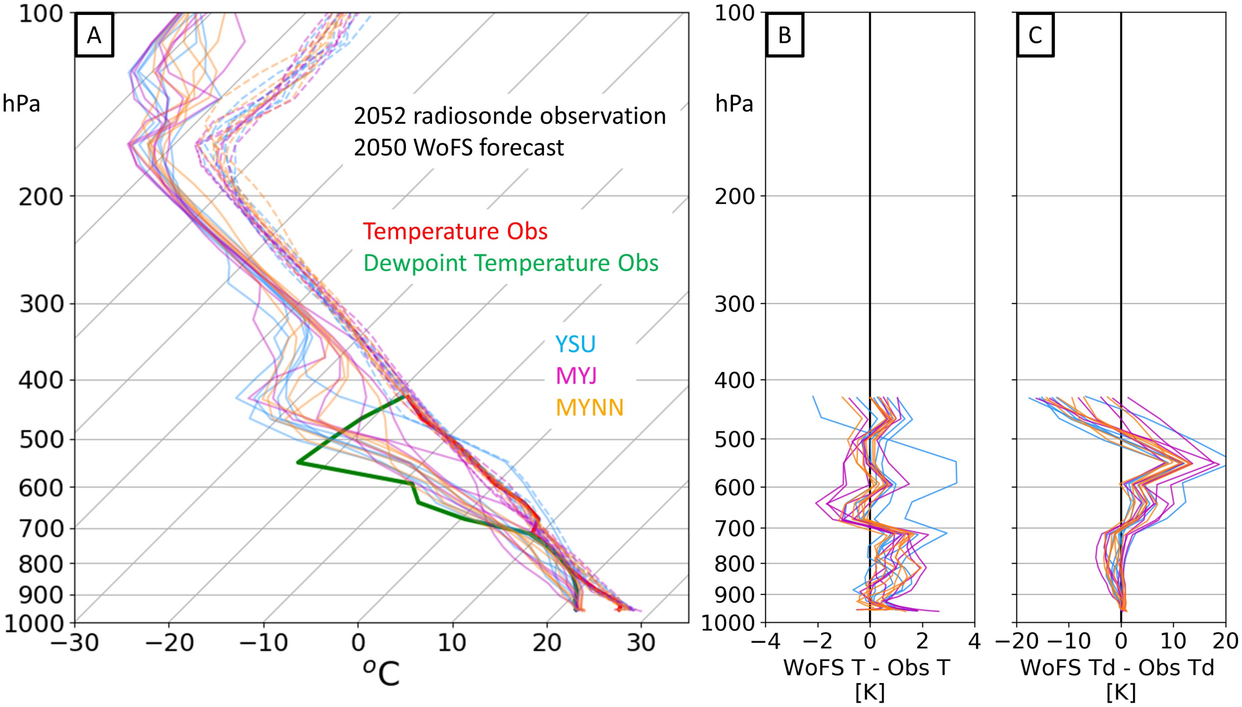

Figure 4.2.7: As in Fig 4.1.6, except for the 2052 UTC radiosonde launch compared to the 2050 UTC WoFS forecast on 20 May 2019, initialized at 2030 UTC.

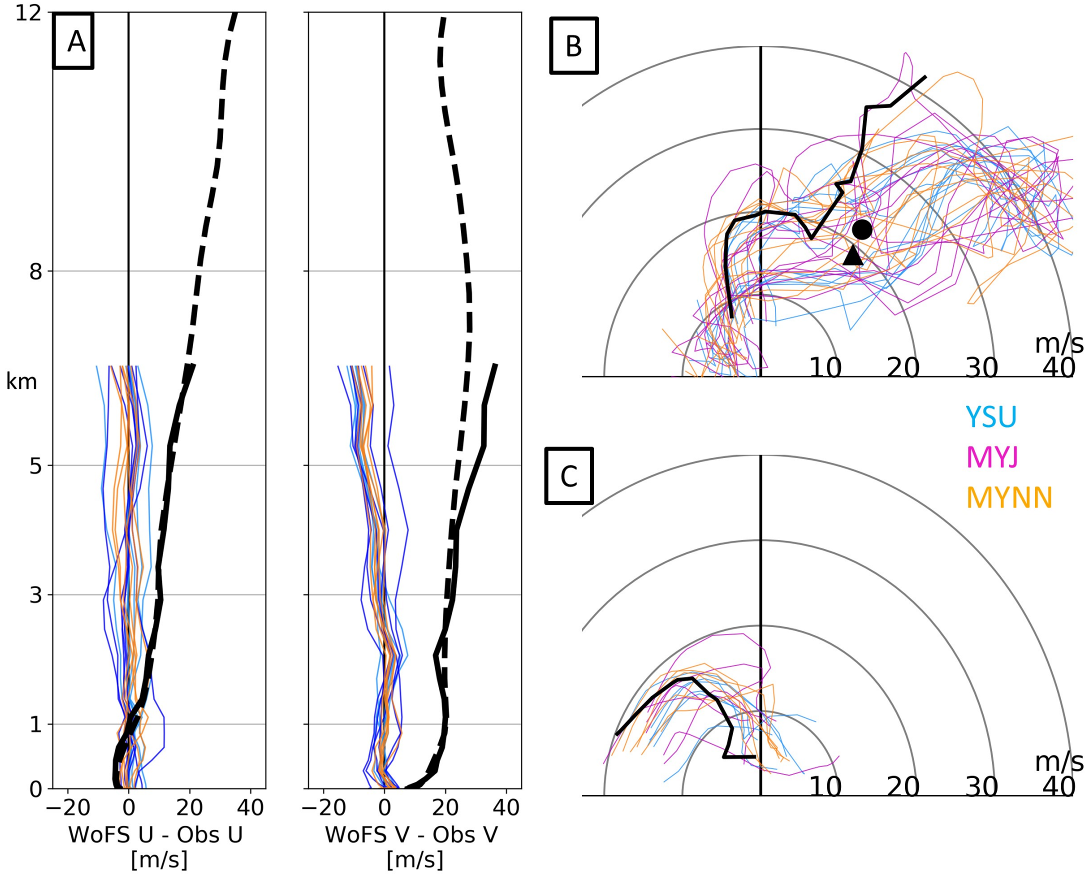

Figure 4.2.8: As in Fig 4.1.10, except for 2052 UTC radiosonde observation and WoFS forecast initialized at 2030 UTC on 20 May 2019, valid at 2050 UTC

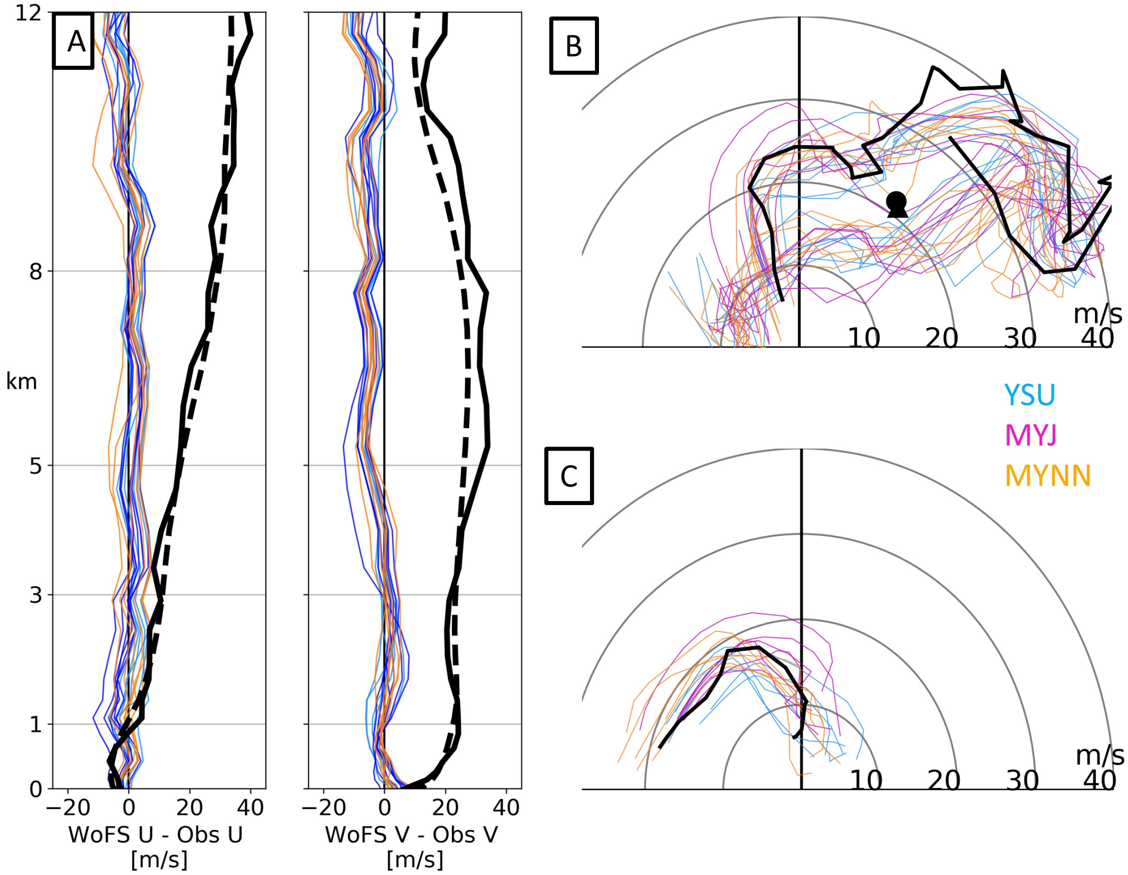

Figure 4.2.9: As in Fig 4.1.10, except for 2142 UTC radiosonde observation and WoFS forecast initialized at 2100 UTC on 20 May 2019, valid at 2140 UTC

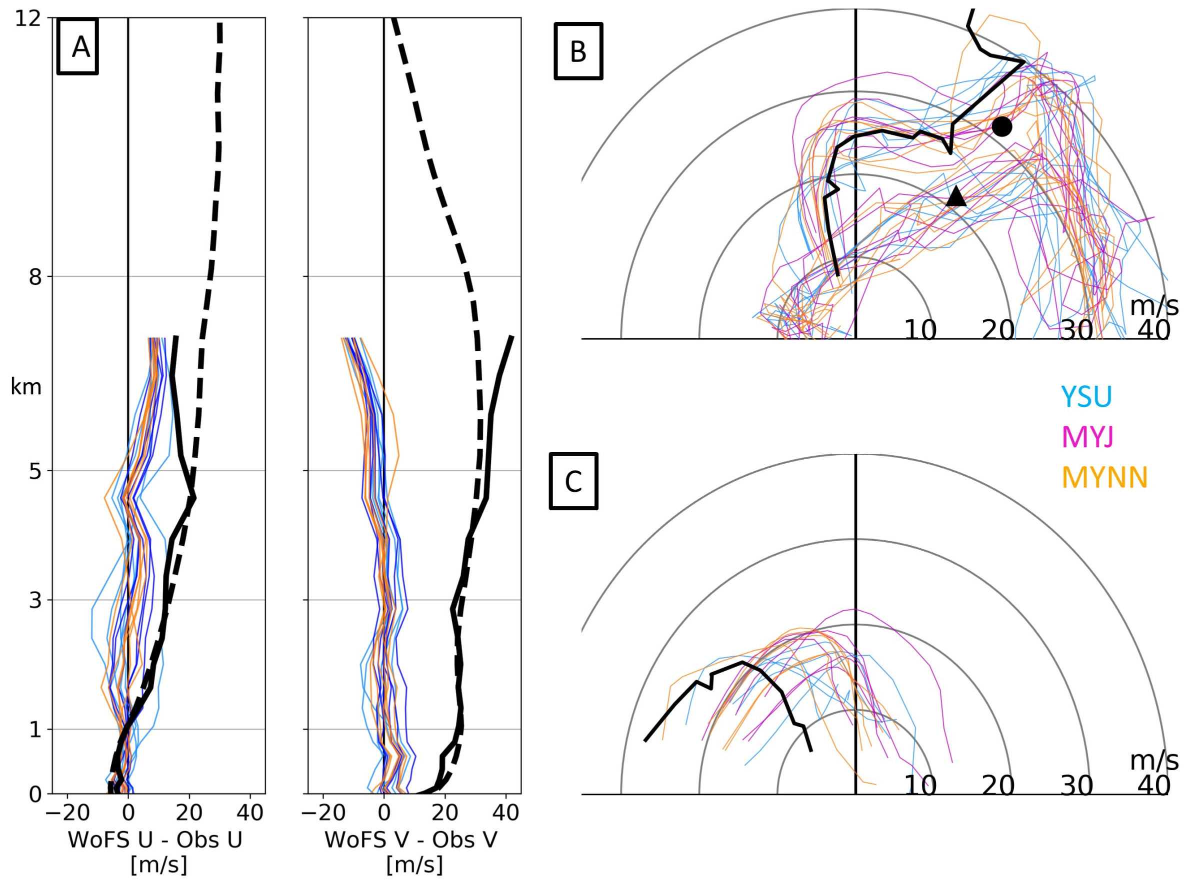

Figure 4.2.10: As in Fig 4.1.10, except for 2242 UTC radiosonde observation and WoFS forecast initialized at 2200 UTC on 20 May 2019, valid at 2240 UTC

4.2.2 Lidar: 1st Deployment

The first of two lidar deployments on 20 May spanned 2030 – 2135 UTC, transitioning from far to near-field at 2120 UTC (Fig. 4.2.11). The winds were observed to remain nearly constant with time (Figure 4.2.11A), with only a small strengthening in the v-component noted after ∼ 2110 UTC. In the WoFS forecasts, however, the winds in WoFS backed with time and showed even more strengthening in the v-component above 500 m AGL. The error in the u and $v$components are generally <2 ms^{-1} in the far-field and errors reaching almost 4 ms^{-1} in the near-field. The maximum low-level error occurs shortly after 2300 UTC (which can be seen by the negative errors in the u- component and the positive errors in the v-component from 60-75 minutes in Fig. 4.2.11A ii, iii). The rotational velocity of the mesocyclone dropped significantly from 2050-2115 UTC as the target supercell merged with a supercell to its east. This merger likely caused a period of reorganization within the mesocyclone of the target supercell, resulting in a drop of rotational velocity. The updraft centers of these two supercells were less than 10 km and appears to have undergone a classic supercell transition as discussed in Hastings and Richardson (2016). The low-pressure perturbation caused by the rotating mesocyclone may have decreased in magnitude during this time, which may be why the lidar does not observe the winds to substantially strengthen in the direction of the supercell as it does for the 17 May case, despite being within 40 km of the storm at the time. The backing seen in the WoFS ensemble mean may be caused by WoFS failing to forecast the drop in mesocyclone intensity, resulting in stronger modification of the near field inflow than was observed.

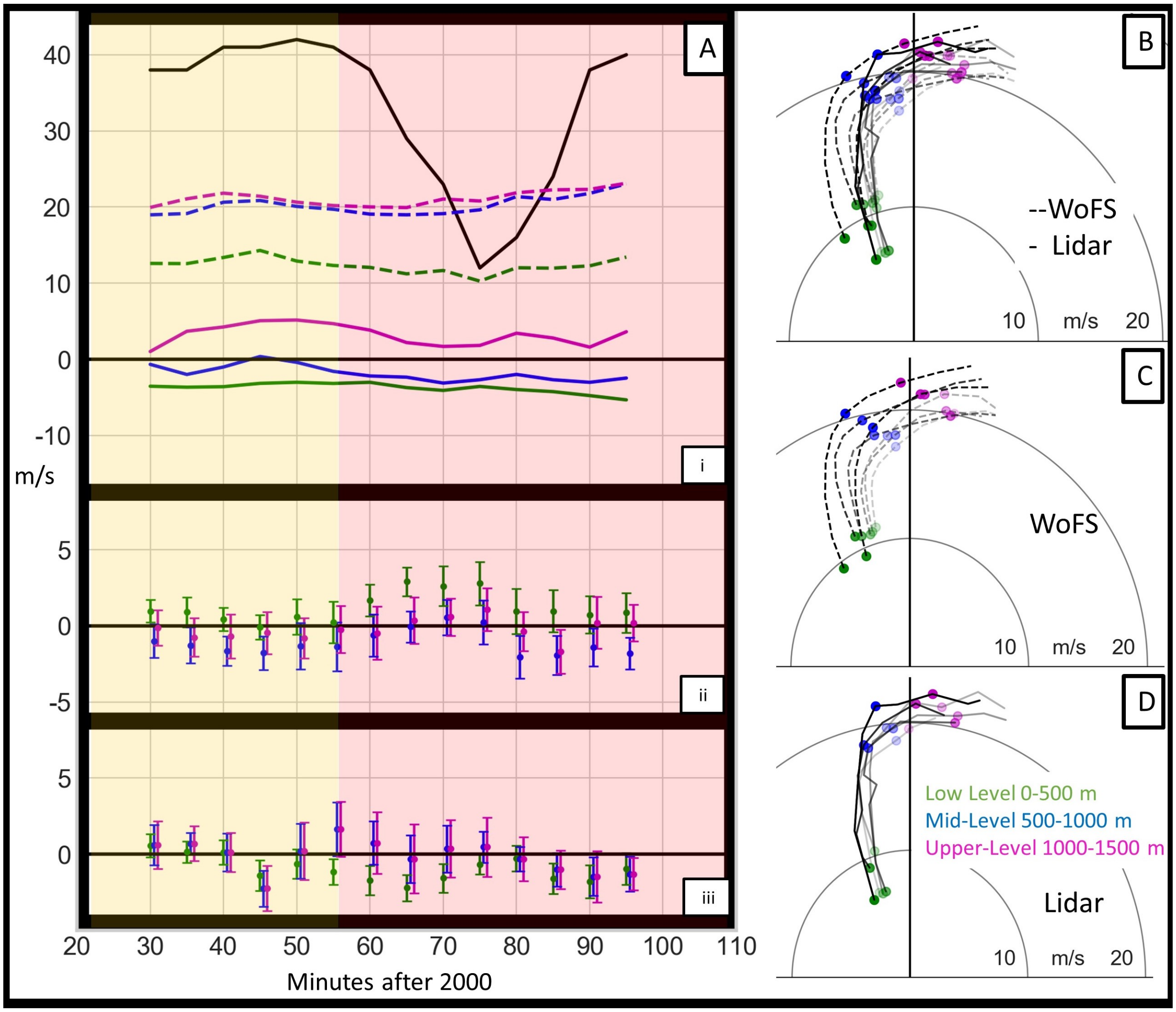

Figure 4.2.11: As in Fig. 4.1.13, except on 20 May 2019. Times shown in panels B,C, and D are 2030, 2040, 2050, 2100, 2110, 2120, and 2130 UTC.

4.2.3 Lidar: 2nd Deployment

The second lidar deployment lasted 20 minutes, from 2155-2210 UTC, and targeted the same supercell as deployment 1 (Fig. 4.2.12). Deployment 2 began just 20 minutes after the first deployment concluded and observed the near-field environment closer to the storm (Fig. 4.2.4), with the target supercell producing a tornado at 2210 UTC just 20 km to the northwest of the lidar. The observed winds veer with time as the storm passes to the northwest, and WoFS forecasts this quite accurately, as the negative errors in the low-level u and v-components of the wind generally remain rather small (<5 ms^{-1}) with time. Veering winds should be expected as the storm becomes displaced northward relative to the lidar, and the zonal forcing component of the low-pressure perturbation abates. The meridional displacement between the lidar and supercell increased throughout this deployment and may have balanced the increased forcing of the strengthening mesocyclone. WoFS is a little more backed than the observations at 2155 UTC, which could result of a prediction of a more intense mesocyclone than was observed in the deployment.

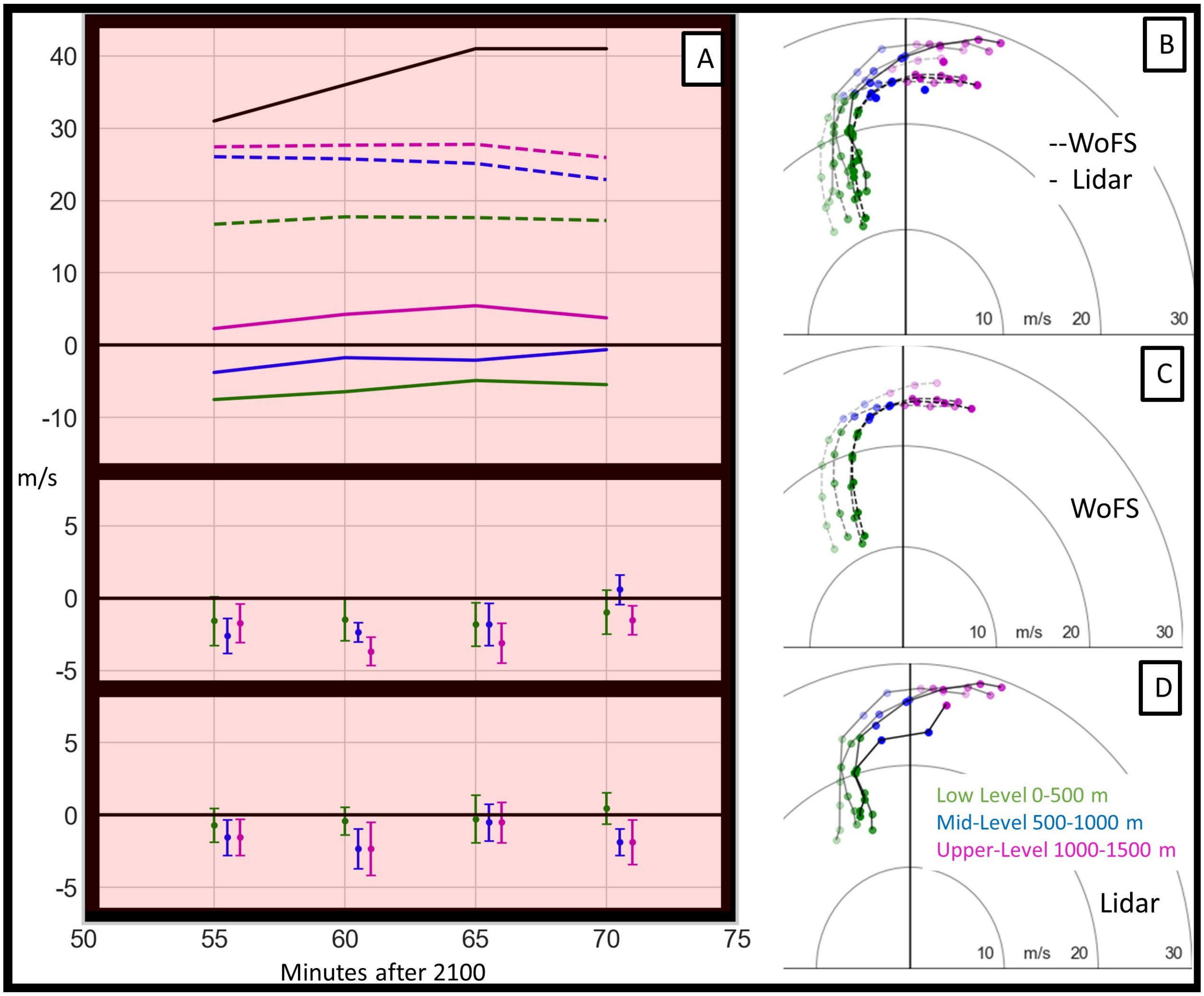

Figure 4.2.12: As in Fig. 4.1.13, except on 20 May 2019. Times shown in panels B,C, and D are 2155, 2200, 2205, and 2210 UTC.

4.2.4 20 May Summary

Unfortunately, no radiosondes made it to the EL on 20 May, leaving no observed CAPE values to compare to WoFS. However, all radiosondes made it above 3 km, allowing for SRH comparisons. WoFS forecasts SRH throughout earlier in the day with errors mostly <50 m^{2}s^{-2}. At later times, 01SRH and 03SRH are generally under forecasted by the WoFS ensemble mean and 01SRH with the YSU members showing the largest errors and the MYNN members showing the smallest errors. Large errors in storm motion seen for the later times (during which the storm became tornadic) do not necessarily translate into large SRH errors, however, because of a positive bias in the WoFS storm-relative v-component pf the wind.

The target supercell went through an interaction with a cell to its east that resulted in a decrease in rotational velocity during the first lidar deployment. It is hypothesized that the weakening of the low-pressure perturbation caused by the drop in rotational velocity caused the observed wind field to remain constant, as opposed to strengthen, as the storm approached the lidar. In contrast, the WoFS guidance backs and strengthens the wind field, suggesting WoFS mmay not represent the drop in mesocyclone intensity. The errors seen in the second deployment are relatively small and is an example how well WoFS can accurately predict near-field supercell environments.A difference between the 20 May and 17 May cases, however, is the storm-relative location of the observations. The lidar was deployed farther south of the eventual supercell track than for the 17 May case. It is possible that the degree to which the WoFS can depict storm-environment modifications is dependent on the location relative to the storm.

4.3 Overview of the 23 May 2019 Pampa, Texas Tornadic Supercells

TORUS targeted two supercells on 23 May, the first of which initiated close to Amarillo, Texas over a SW-NE boundary left behind by morning convection. This non-tornadic supercell tracked NE trough the Texas panhandle and was targeted from 2200 to 2315 UTC. The second supercell, which initiated off the outflow of the first a few miles south of Amarillo moved to the northeast and was targeted from 2315 to 0015 UTC. The second supercell was tornadic and produced a large tornado from 2315 to 2330 UTC. During the second lidar deployment, a third supercell (non-tornadic) tracked along a path just south and east of the first two supercells and approached the lidar location at 0015 UTC. All three supercells were well observed by the KAMA WSR-88D (Fig. 4.3.1).

Of the six radiosonde deployments on this day, four made it to the EL and can be compared to WoFS MLCAPE and SBCAPE. Three radiosondes were in both the far and near field, one of each not reaching the EL. TORUS deployed the lidar once on each of the targeted supercells, the second deployment observed the near storm environment of a tornadic supercell within an hour of producing a tornado.

The WoFS forecasts generally depicted well the evolution of the first two observed storms(Fig. 4.3.2). Errors in storm object location for the first two storms are shown in Fig.4.3.3. The WoFS primarily possessed a northern displacement error in the first deployment (panels A,B), but the error in the second targeted storm is to the SW (panels C,D). The error during the second deployment may be caused by the merging of UH objects of the targeted modeled storm with the storm to its SW within the object identification code adopted from

Britt et al. (2020). A look at the member paintball in Fig.4.3.2 shows that the location covered by the second storm and the storm to its SW (storm 3) is well predicted by WoFS, but the updrafts in the WoFS forecasts are not as are indistinguishable. The author inspected individual member reflectivity forecasts and found that some members in WoFS predict two distinct high reflectivity cores, while others do not. All members produce a broad UH object in the object identification code, and the author was unable to find a UH threshold that well separated the two updrafts.

Note the magnitude of the error in storm object location decreases after 2345 UTC. The author used the latest available forecast for all analysis, so the decrease in this error is likely due to the assimilation of radar velocity that possess two distinct updrafts, which caused the members that previously had trouble separating the updrafts to better forecast two supercells (e.g. two separate rotating updrafts).

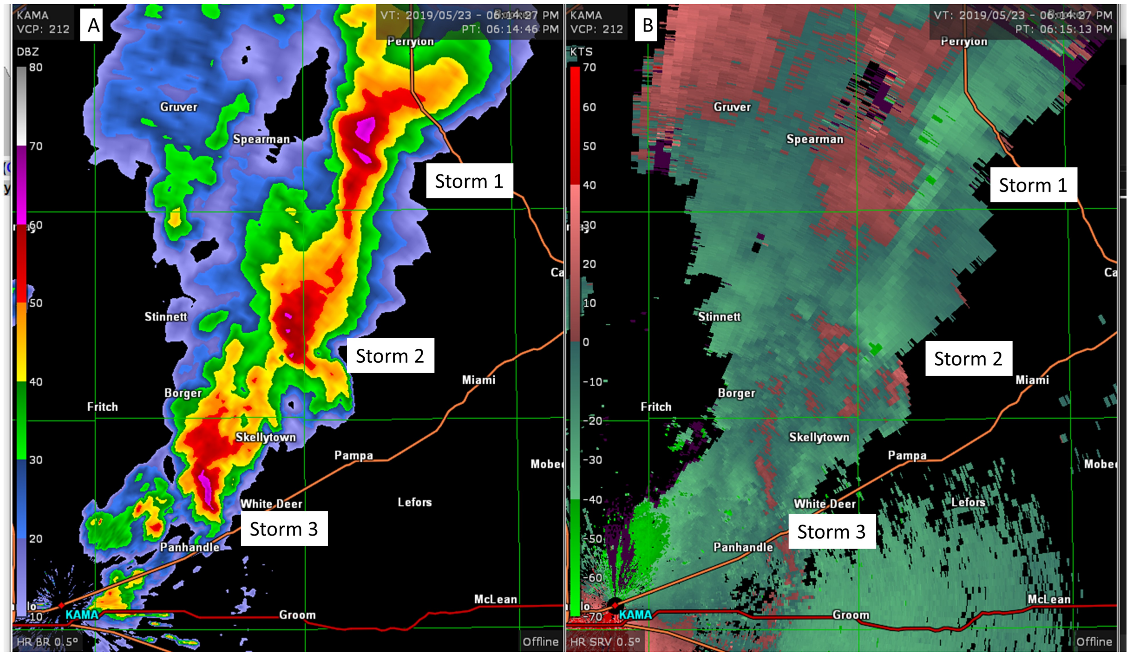

Figure 4.3.1: Radar images from KAMA of the 23 May Pampa, Texas supercell at 2315 UTC, the time of the Pampa tornado report. Panel A shows reflectivity (dBZ); Panel B shows storm-relative velocity (kts).

Figure 4.3.2: The solid black box encompasses contour of 45 dBZ simulated composite reflectivity from 30-minute forecasts from all 18 WoFS members initialized at 2300 UTC, valid at 2315 UTC on 23 May. WoFS forecast initialized at 2130, valid 2210 UTC. Different color shading depicts different ensemble members.

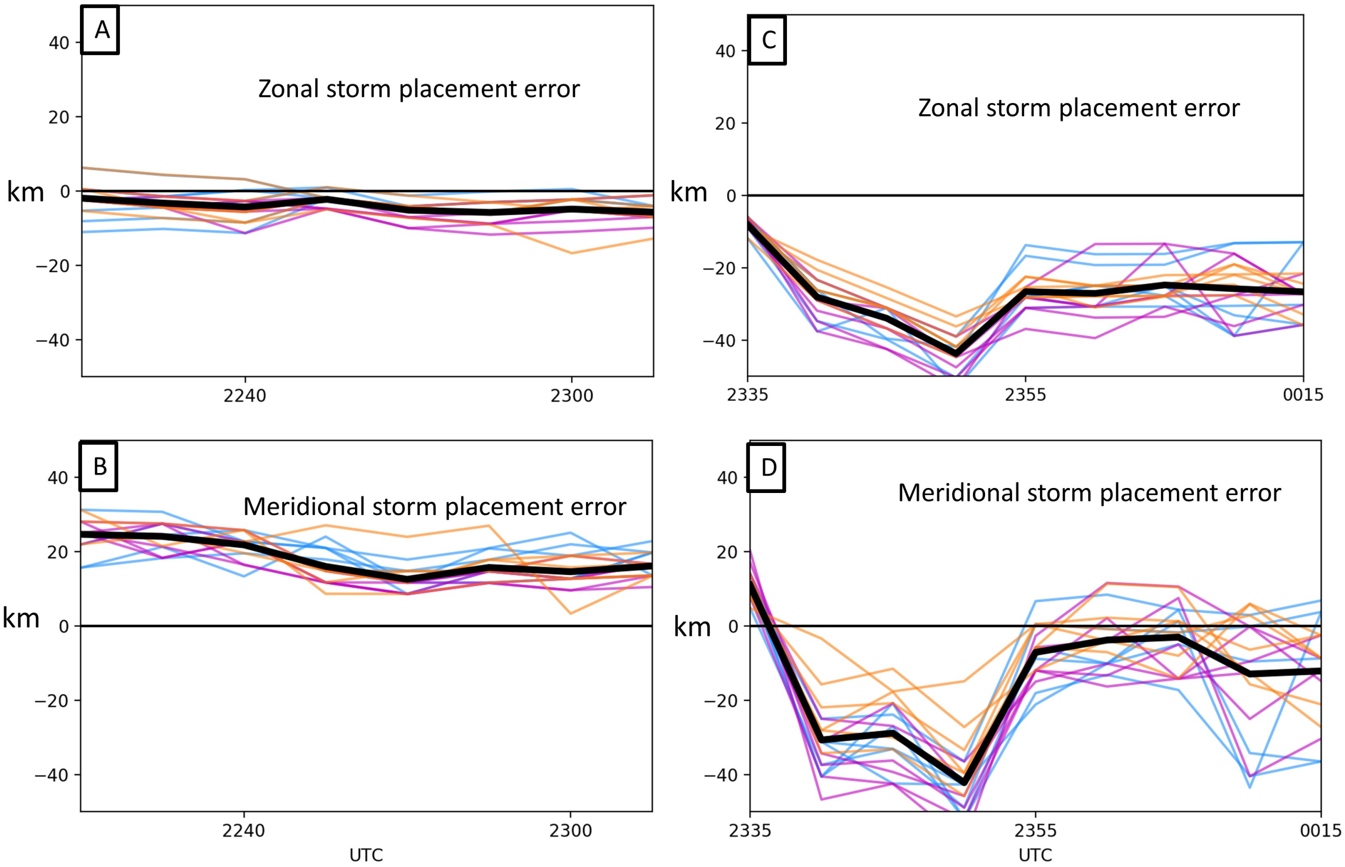

Figure 4.3.3: As in 4.1.3, except for 23 May 2019

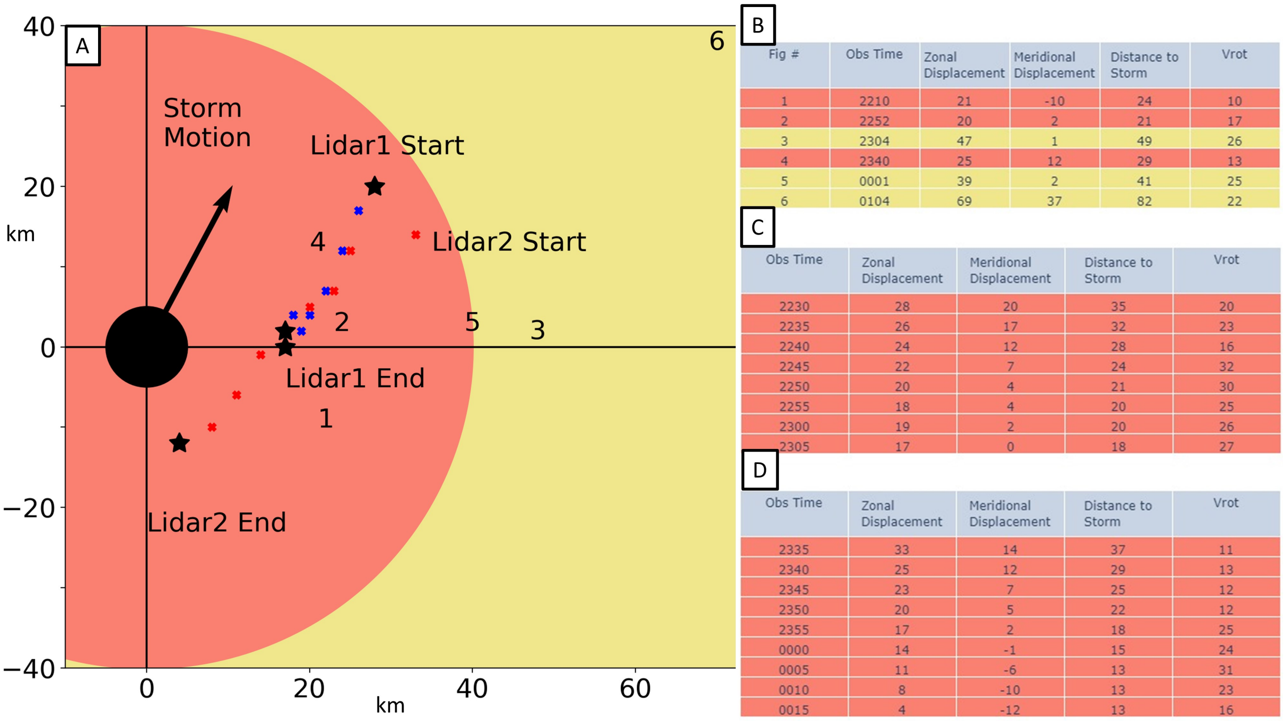

B

Fig #	Obs Time	Zonal Displacement	Meridional Displacement	Distance to Storm	Vrot
1	2210	21	-10	24	10
2	2252	20	2	21	17
3	2304	47	1	49	26
4	2340	25	12	29	13
5	0001	39	2	41	25
6	0104	69	37	82	22

C

Obs Time	Zonal Displacement	Meridional Displacement	Distance to Storm	Vrot
2230	28	20	35	20
2235	26	17	32	23
2240	24	12	28	16
2245	22	7	24	32
2250	20	4	21	30
2255	18	4	20	25
2300	19	2	20	26
2305	17	0	18	27

D

Obs Time	Zonal Displacement	Meridional Displacement	Distance to Storm	Vrot
2335	33	14	37	11
2340	25	12	29	13
2345	23	7	25	12
2350	20	5	22	12
2355	17	2	18	25
0000	14	-1	15	24
0005	11	-6	13	31
0010	8	-10	13	23
0015	4	-12	13	16

Figure 4.3.4: As in 4.1.4, except for 23 May 2019

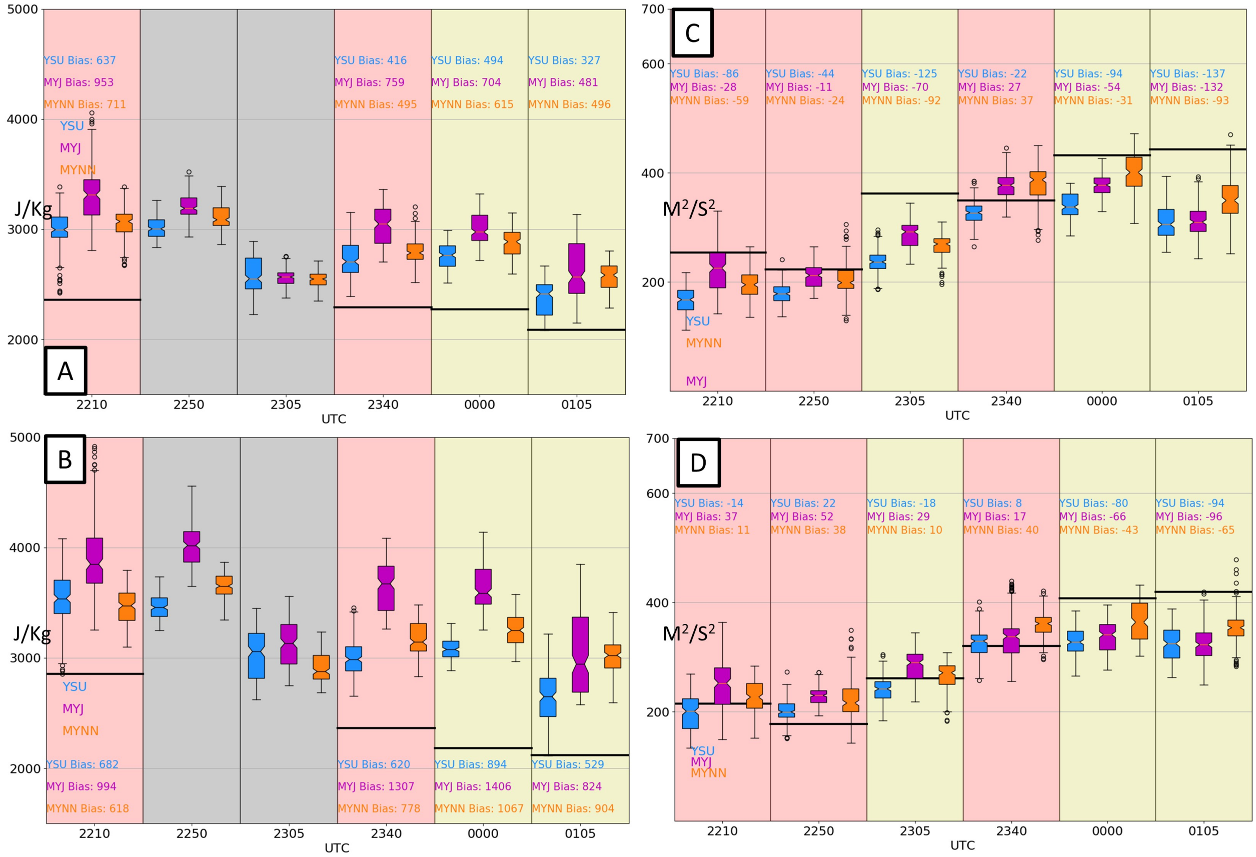

Figure 4.3.5: As in 4.1.5, except for 23 May 2019

4.3.1 Radiosondes

4.3.1.1 Thermodynamics The environment of each of the first two storms was sampled by 3 radiosondes. Of the 4 radiosondes that made it to the EL, WoFS substantially over forecasts both MLCAPE and SBCAPE at all observation times (Fig. 4.3.5). The errors are consistently smallest for the YSU members and consistently largest for the MYJ members, as also seen for the first two cases. Figures 4.3.5-4.3.7 show that the CAPE errors appear to be related mostly to low-level temperature errors, except at 0105 UTC (Fig. 4.3.7), which posted the lowest CAPE errors of the day. MLCAPE and SBCAPE errors also are found to be smallest for the latest observation-WoFS pair in the 17 May observations.

The surface temperature errors are particularly large (2-4 K) in the 2210 UTC forecast (Fig. 4.3.5), with low-level lapse rates that are too steep up to 800 hPa, the approximate PBL top. The temperature error is smaller in later forecasts, as a response to cooling of 2 K in observations and $\sim$ 5 K in the ensemble members. This cooling starts to become evident in the 2340 UTC observation(Fig. 4.3.6). The larger near-surface errors at the earlier times could be related to anvil shading present at the radiosonde locations.

Above the PBL in the 2210 UTC observation, the WoFS forecasts are notably warmer and drier than observed. The peculiar observed reduction in lapse rates and drying near 600 hPa suggests that the warm error at 725 hPa is caused by cooling in the observation, perhaps storm induced, that is not represented in the WoFS forecasts. Wade et al. (2018) shows similar deep near-saturation below 600 hPa in many near-field sounding observations and presents evidence that this results from storm-induced mesoscale lifting in the near-field inflow (although a contribution from precipitation evaporating into the inflow from above cannot be ruled out). This possible lifting also is seen in the 2252 UTC observation (another near-field sounding), however the WoFS forecasts now appear to be representing this cooled/moistened environment quite well, perhaps from another assimilation cycle that better initialized the storms. Temperature errors in later forecast periods look to be a result of misplacing the small temperature inversion/warm layer seen in the observations near 700hPa. These errors are typically not larger than 2 K, owing to the weakness of the temperature inversion/warm layer.

WoFS predicts the top of the PBL conditions quite well at the later forecast times and had errors in temperature and dewpoint typically no larger than 2 K. Errors in temperature and dewpoint above the PBL appear to be caused largely by the radiosonde entering clouds where none exist in WoFS (note there was rarely an occurrence of WoFS forecasting clouds where none existed, possibly implying a negative “cloudiness” error in WoFS). Synthetic satellite shows that WoFS indeed forecasts anvils for these storms, but it appears that the WoFS does so without saturating in the layer where the clouds exist, resulting in larger errors in dewpoint than temperature.

4.3.1.2 Kinematics Overall, WoFS more accurately forecasts both 01 and 03SRH on 23 May than on 17 May. All six WoFS ensemble mean forecasts have mean errors less than 100 m^2s^{-2} and commonly less than 50 m^2s^{-2}. Peculiarly, WoFS under predicts SRH in the far field (~ -100 m^2s^{-2}) more than in the near field (~ -40 m^2s^{-2}), except for the 2340 UTC forecast in which the ensemble mean predicts SRH perfectly (~ 10 m^2s^{-2}, error overall with the mean magnitude of the error among the three PBL schemes no larger than 40 m^2s^{-2}). Among all of the soundings, the YSU scheme commonly under forecasts mean SRH more than the other schemes, which was also found in the first two cases. Also, the YSU scheme typically has the largest errors in the 03SRH but posts smaller errors than the other schemes in 01SRH.

Errors in storm motion vectors are all small (<2 ms^{-1}), with perhaps the only exception being the 2252 UTC observation, which displays a stronger veer-back-veer signal than any of the WoFS forecasts at that time, and in any observation at other times. This leads to the larger error in storm motion, which leads to low-level storm-relative winds that are too backed in the WoFS forecasts, culminating in an over forecast of 01SRH. The small errors in storm motion supports the hypothesis that the errors in storm object location are not attributable to differences in observed and modeled storm motion vectors.

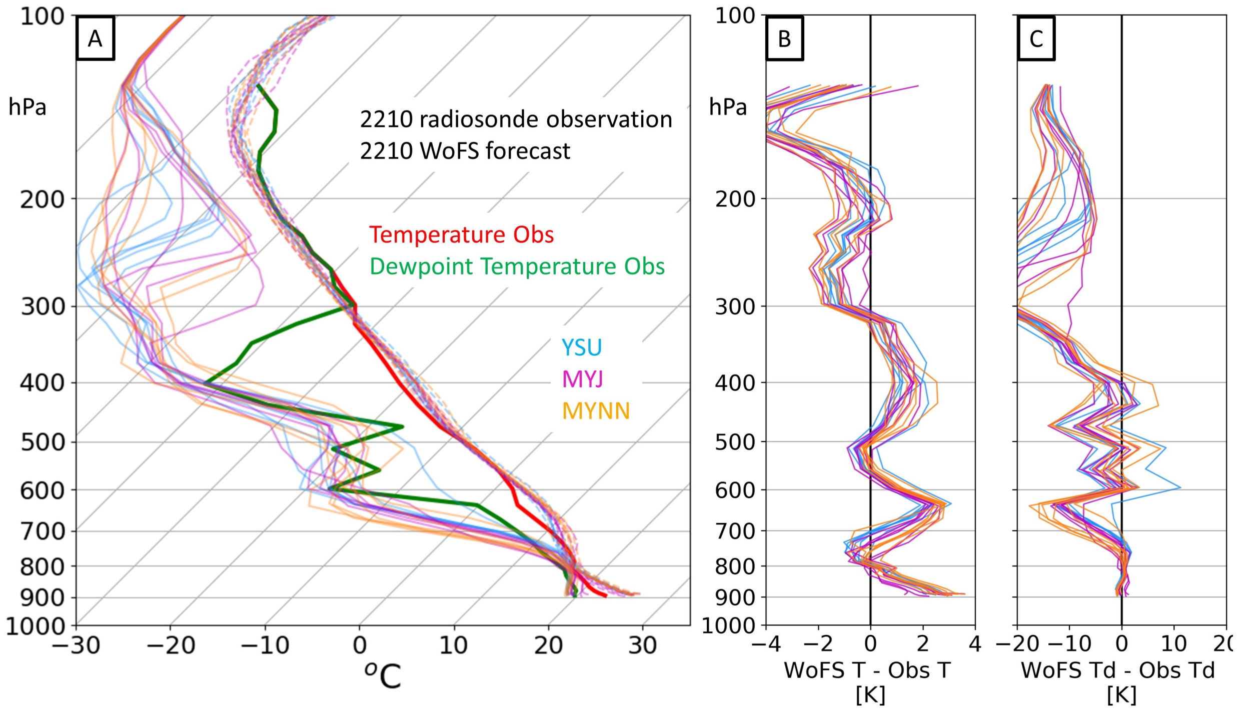

Figure 4.3.6: As in Fig 4.1.6, except for the 2210 UTC radiosonde launch compared to the 2210 UTC WoFS forecast, initialized at 2130 UTC.

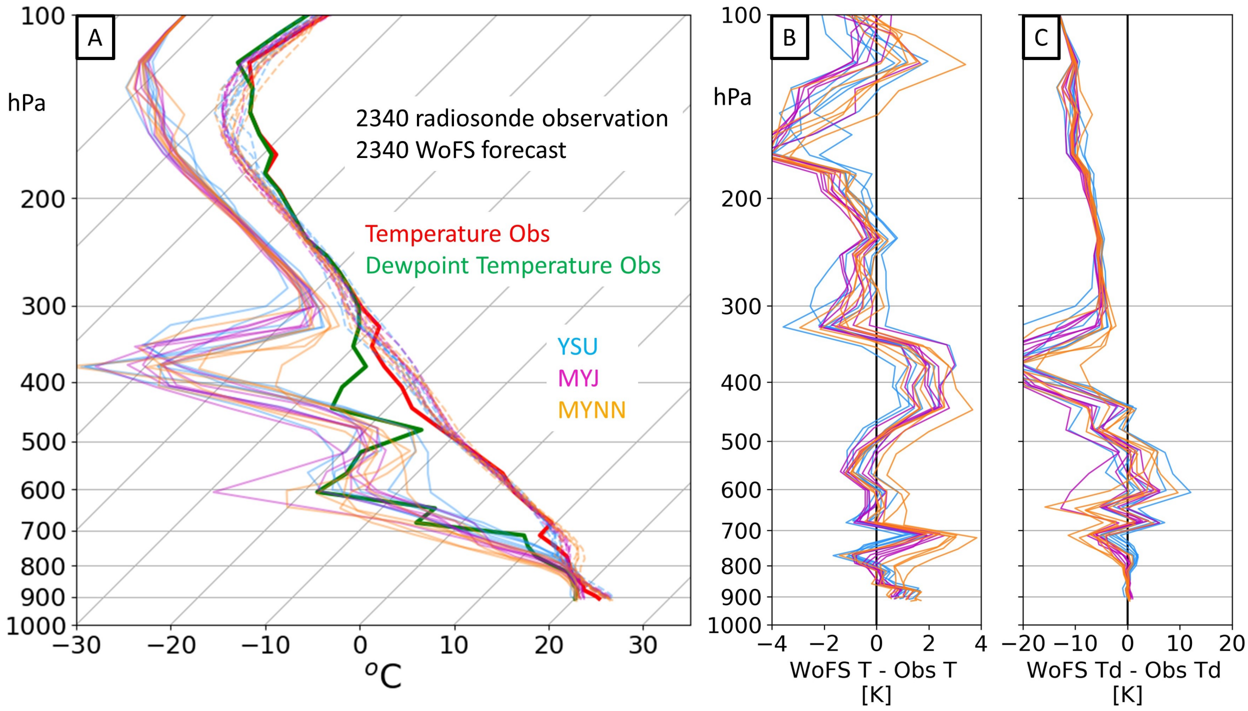

Figure 4.3.7: As in Fig 4.1.6, except for the 2340 UTC radiosonde launch compared to the 2340 UTC WoFS forecast, initialized at 2300 UTC.

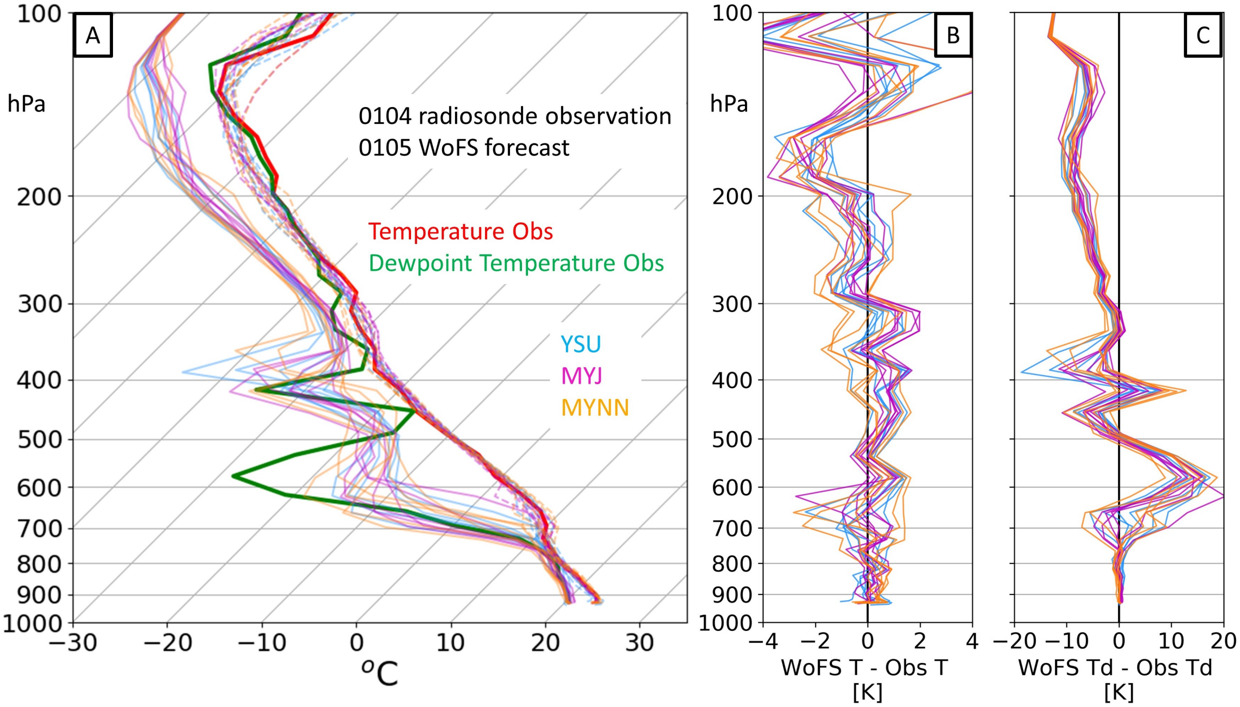

Figure 4.3.8: As in Fig 4.1.6, except for the 0104 UTC radiosonde launch compared to the 0105 UTC WoFS forecast, initialized at 0030 UTC.

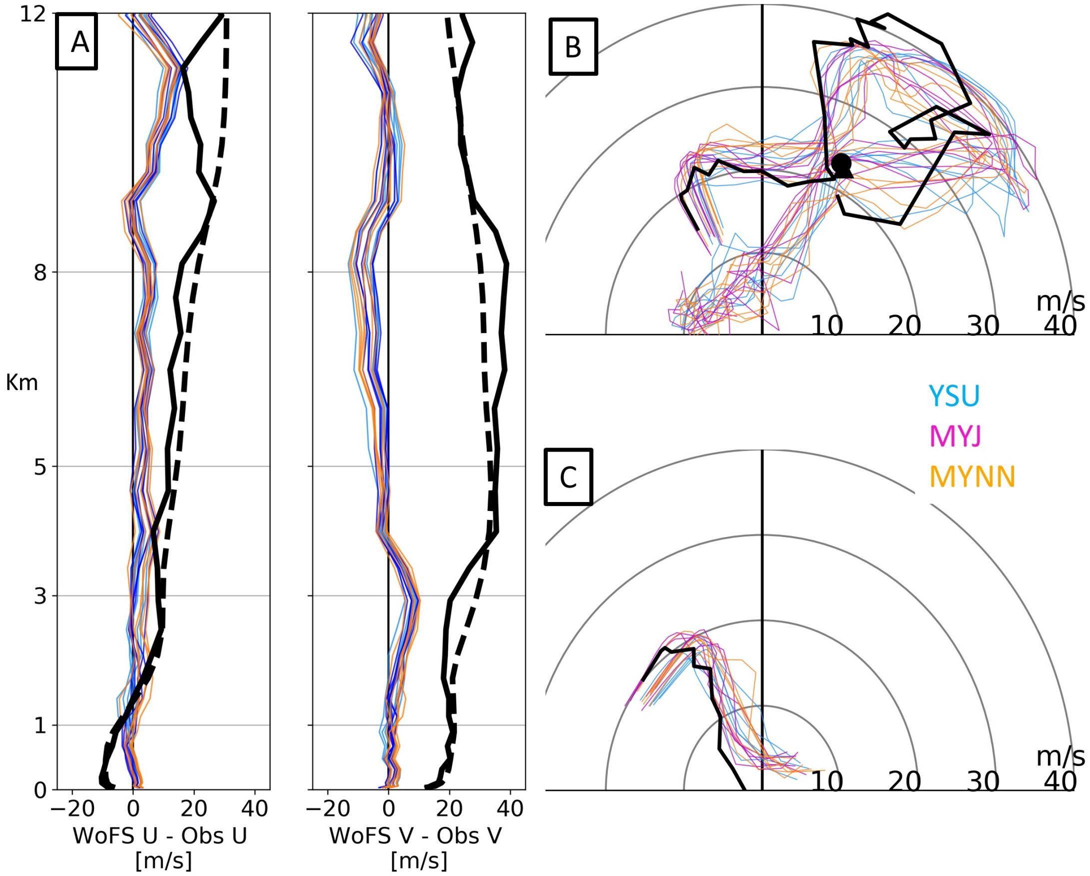

Figure 4.3.9: As in Fig 4.1.10, except for 2210 UTC radiosonde observation and WoFS forecast initialized at 2130 UTC, valid at 2210 UTC

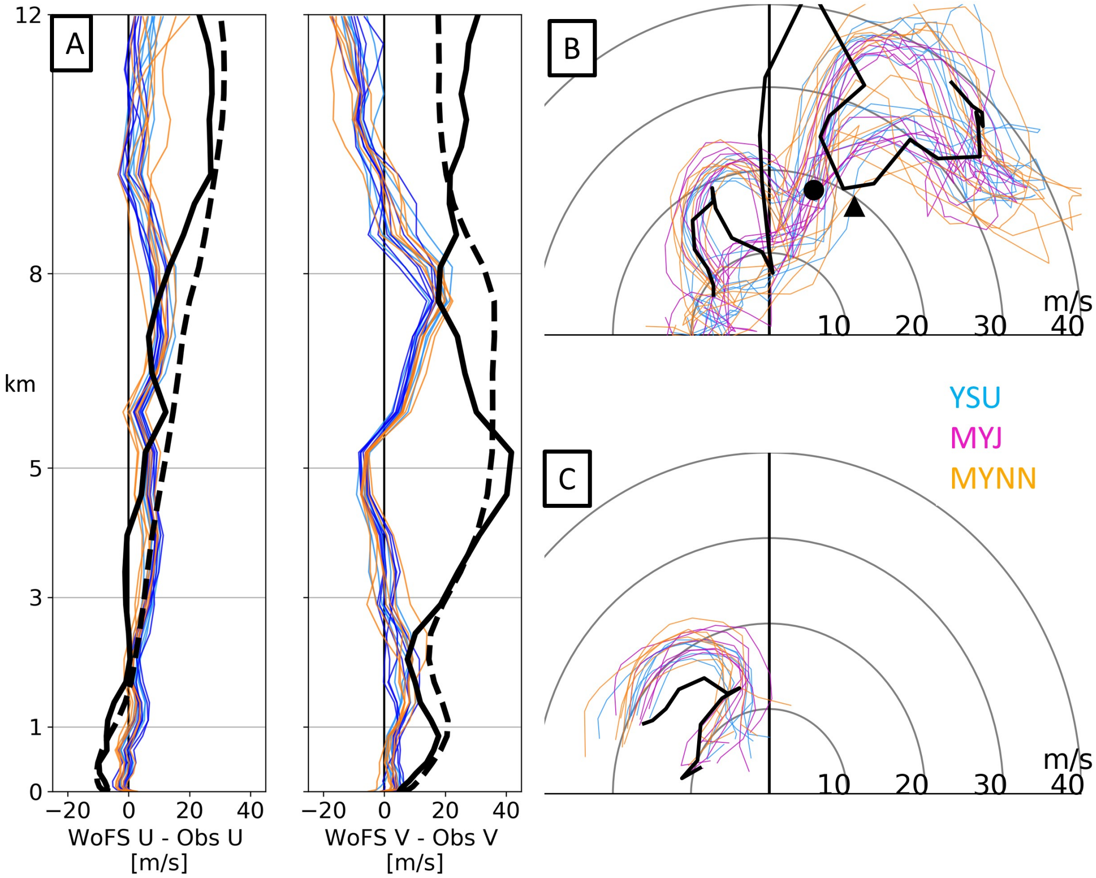

Figure 4.3.10: As in Fig 4.1.10, except for 2252 UTC radiosonde observation and WoFS forecast initialized at 2230 UTC, valid at 2250 UTC

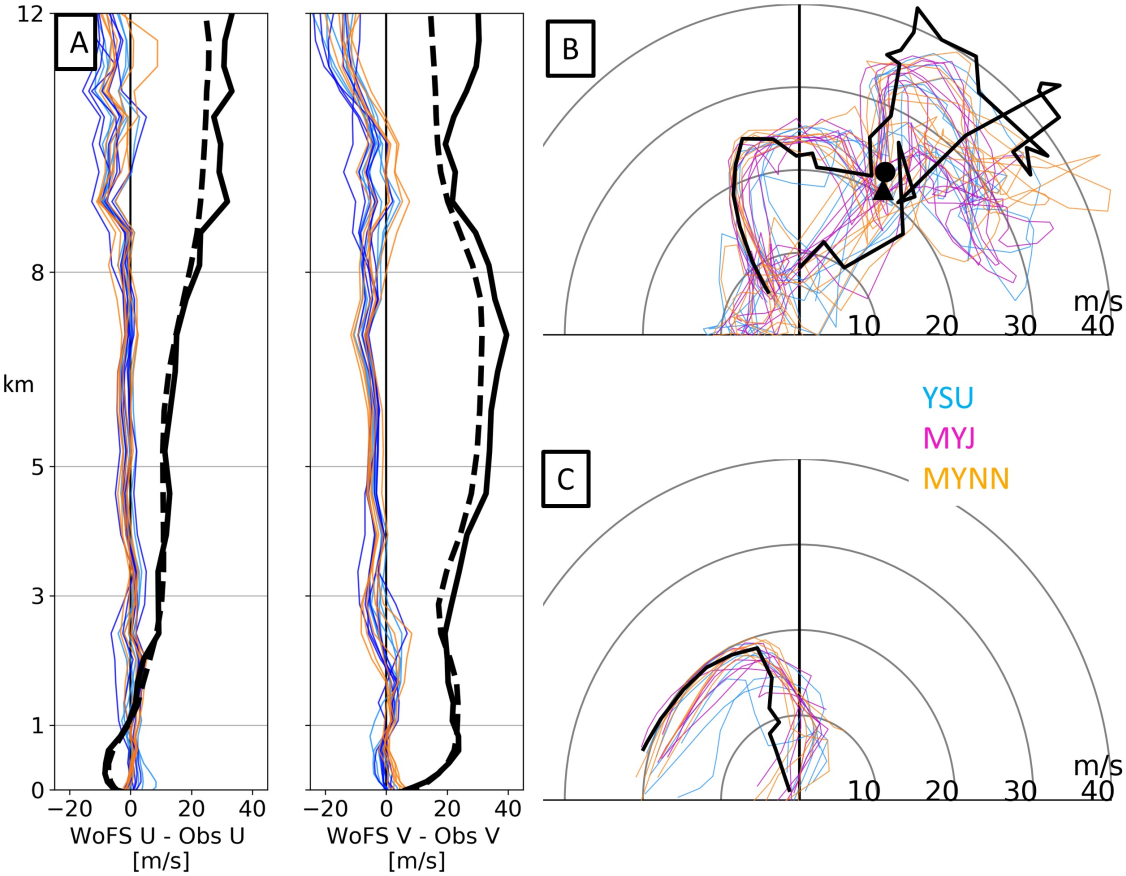

Figure 4.3.11: As in Fig 4.1.10, except for 0104 UTC radiosonde observation and WoFS forecast initialized at 0030 UTC, valid at 0105 UTC

4.3.2 Lidar: 1st Deployment

The first lidar deployment on 23 May lasted 35 minutes and observed the near field environment from a northeast to east orientation relative to the target supercell (Fig. 4.3.4). The lidar was only able to sample winds up to 500 meters because of low clouds, but still was able to observe a backing and strengthening in the winds below that level(Fig. 4.3.11). With the decreasing zonal distance to the strengthening storm, backing and strengthening winds are expected here. WoFS accurately predicts a small amount of backing; however, at the time to storm is closest to the lidar the large increase in low-level wind speeds is under predicted as seen by the negative errors in u and v at 2305 UTC. Interestingly, WoFS backs the winds more than the observation at 2300 UTC. The rotational velocity of the storm appears to vary by over 10 ms^{-1} during this period, so WoFS could be forecasting too constant of a low-pressure perturbation that leads to winds backing too much while the mesocyclone is weakening and too little while the storm is strengthening.

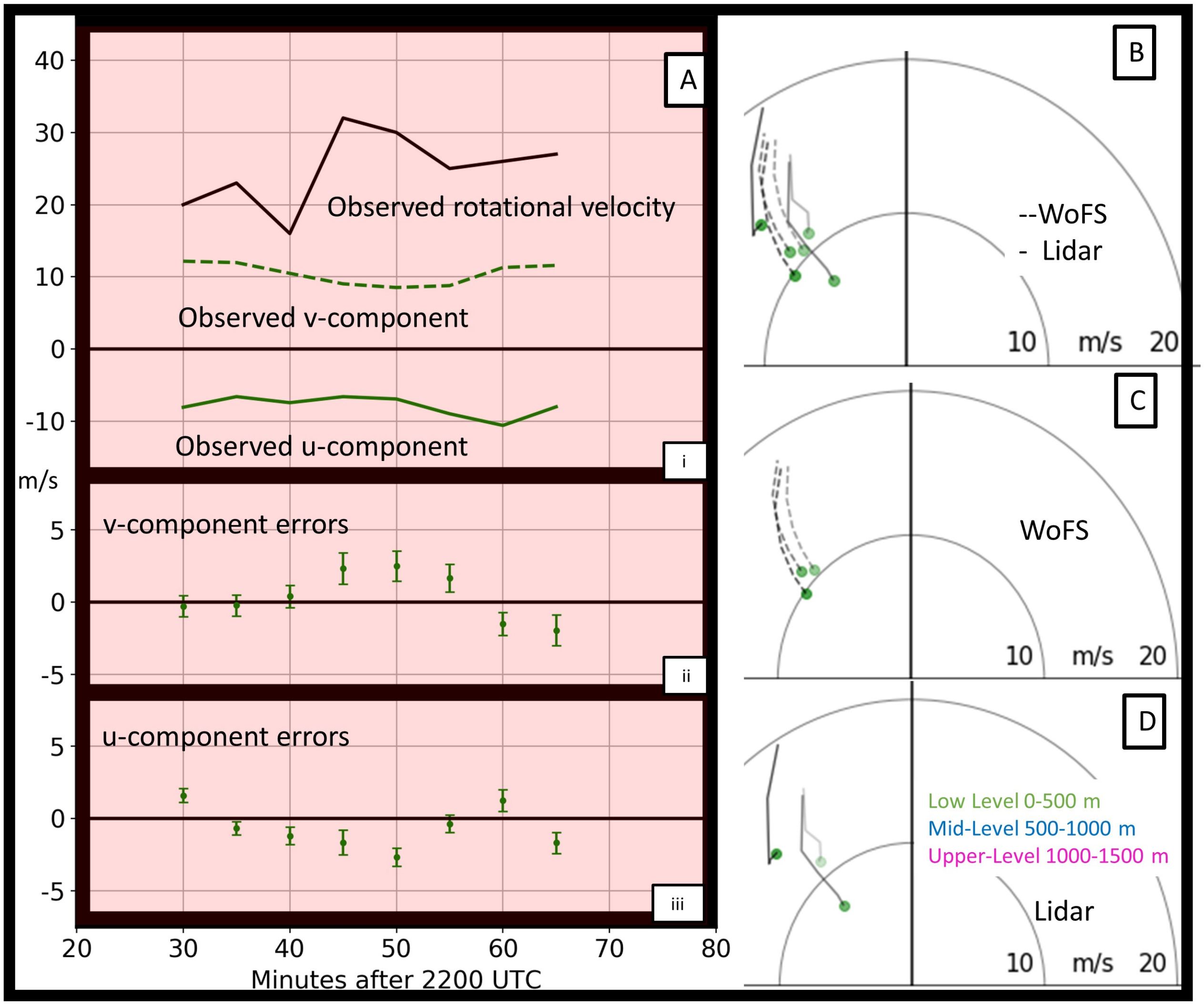

Figure 4.3.12: As in Fig. 4.1.13, except on 23 May 2019. Times shown in panels B,C, and D are 2240, 2250, 2300 UTC.

4.3.3 Lidar: 2nd Deployment

The second lidar deployment lasted from 2335 – 0015 UTC and sampled the near field environment of the second target supercell of the day (Fig. 4.3.12). This deployment begins northeast and ends almost due south of the supercell (Fig 4.3.4). This is a particularly interesting deployment as the winds backed early on, particularly above 250 m AGL, then veered as the storm moved north of the lidar after 0000 UTC, causing a strong meridional increase in the winds at 0005 UTC (Fig 4.3.12Ai). WoFS initially had small errors in the wind but appears to forecast the opposite trend than what is seen in the lidar observations, leading to some of the largest wind errors among the three case studies of over 5 ms^{-1} in both the u and v-components. WoFS predicts a weaker zonal component of the wind as the storm approaches the lidar, then backs the low level wind and increases the $v$component of the upper-level wind at 0000 UTC. Both the lidar and WoFS agree on the strengthening of the meridional component of the wind at 0005 UTC, but the winds are still much weaker in WoFS than observed. The time-dependent changes before 0005 UTC suggest that the storms in WoFS may have been weaker, leading to a lack of a backing signal in the model and under forecasting the increase in wind speed after 0005 UTC. Another hypothesis is WoFS could be under forecasting storm modification of the inflow environment.

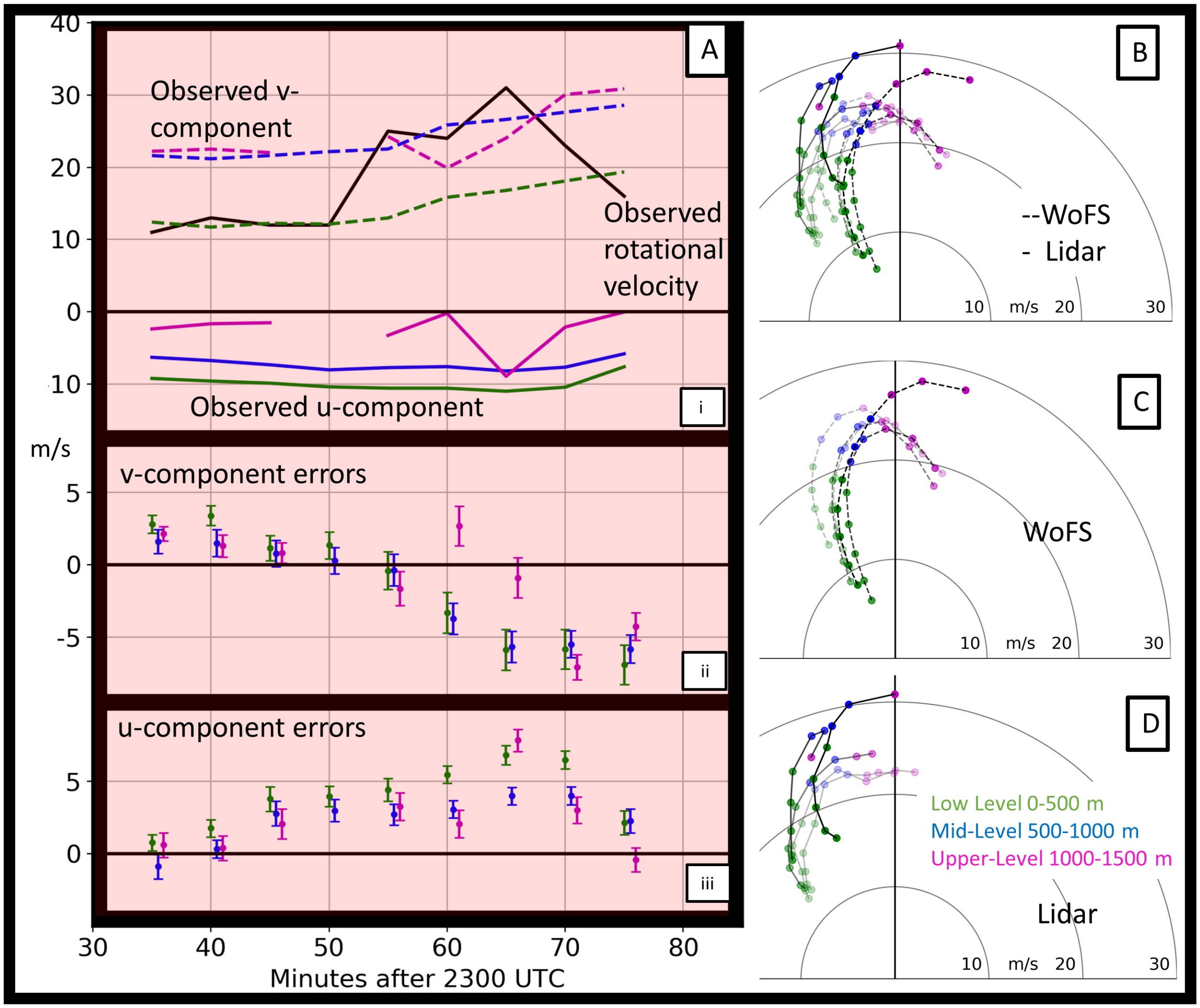

Figure 4.3.13: As in Fig. 4.1.13, except on 23 May 2019. Times shown in panels B,C, and D are 2335, 2345, 2355, 0005, and 0015 UTC.

4.3.4 23 May Summary

WoFS over forecasts both MLCAPE and SBCAPE in all available radiosondes. The YSU scheme, which predicts the lowest values of CAPE, produced smaller errors than MYJ and MYNN, with only a few exceptions. WoFS accurately forecasts both 01SRH and 03SRH, with errors commonly $<100 m^2 s^{-2}$. Interestingly for this case, the errors are larger in the far field than the near field.

Both lidar deployments collected near field observations during a period of fluctuating mesocyclone strength, as evidenced by the changing rotational velocity. WoFS posts the largest errors when the rotational velocity quickly increases in magnitude, and errors drop when the rotational velocity decreases. This finding suggests that WoFS environmental forecasts of the wind field may be degraded when forecasting rapidly evolving storms or WoFS could be under resolving storm modification of the inflow environment.

5 Discussion and Conclusions

5.1 Radiosondes

For the six radiosondes from the three case studies that made it to the EL, WoFS over forecasted both SBCAPE and MLCAPE in all six, with mean errors near 500 Jkg^{-1} and 1000 Jkg^{-1} on 17 May and 23 May, respectively. The far field 2302 UTC observation on 17 May possessed a smaller error than the near field 0106 UTC observation, and this trend is also seen on 23 May, with the far field 0104 UTC possessing the smallest errors of the day. While more samples are needed to substantiate this trend, it seems there may be an inverse relationship between WoFS over prediction of CAPE and distance from the storm (e.g. WoFS errors in CAPE becomes larger closer to the storm). The CAPE errors were often partially attributable to a positive surface temperature error (23 May 2210 UTC observation, Fig.4.3.6) and also by WoFS forecasting too cool temperatures above the PBL (MYNN scheme in the 17 May 0106 UTC observation, Fig.4.1.9). The temperature data from the mobile mesonets was still undergoing processing at the time of the author's defense, and could not use the temperature data to verify the radiosonde surface temperatures.

The YSU scheme typically forecasts warmer temperatures above the PBL and a drier PBL leading to lower CAPE than both the MYJ and MYNN schemes, resulting in smaller errors in every radiosonde observation. The convective contamination in the radiosondes on 20 May and 23 May is so frequent in the vertical profiles that it is difficult to discern, but the YSU scheme consistently predicts a warmer and drier PBL than the MYJ and MYNN schemes. A drier PBL would increase the height of the lifting condensation level and could explain the smaller predicted CAPE in the YSU schemes.

The 17 May 2302 UTC radiosonde observation provides an example of how WoFS PBL members are hoped to behave in tandem: the local schemes predict cooler, wetter PBLs with negative and positive errors respectively, while the YSU scheme forecasts a warmer, drier PBL with positive and negative errors respectively. This spread almost symmetrically encompasses the observation, leading to an ensemble mean with nearly no temperature or dewpoint temperature error with in the PBL. Even at 750 hPa, the YSU scheme under forecasts the magnitude of the temperature inversion, while MYJ and MYNN over forecast it, leading to a negligible error in the WoFS ensemble mean.

Although WoFS often accurately forecasts SRH with errors <50 m^2s^{-2}, there were several instances when the storm-relative winds are not backed and/or strong enough in the lowest 1 km. This is clearly evident in the 0106 UTC observation on 17 May (Fig. 4.1.12, panel c) and the 0104 UTC observation on 23 May (Fig. 4.3.10). Considering WoFS shows smaller SRH errors earlier in the event on 17 May and 23rd (SRH errors were smaller overall for all observations on 20 May), there may be a relationship between SRH errors and supercell duration or the nocturnal transition. It was anticipated that SRH errors would be more strongly dependent on distance from the storm, but the first radiosonde observations on 17 May and 23rd were near-field and posted the smallest errors of each day, respectively. This suggests WoFS may be under forecasting storm modification of the environment, not solely in a spatial sense, but in a temporal sense. This trend is seen clearly on 17 May in Fig.4.1.5 where WoFS increases SRH later in the evening, but not to the extent seen in the observations.

5.2 Lidar

The 5 lidar provide high-resolution a time series of the evolving environment close to strong, often tornadic supercells, a unique data set. Every lidar deployment observed at least 15 minutes of near field, potentially storm-modified air and two deployments even captured the transition between near and far field environments. In these two deployments (17 May and the first on 20 May) WoFS forecasts modifications of the low-level winds as the storm approaches the lidar, but not in the same character as the observations, which seems dependent on the evolution of the mesocyclone. The 17 May supercell's rotational velocity is nearly constant during the deployment, and the lidar observed a consistently backing and strengthening wind field with time. WoFS under forecasts the magnitude of this backing, possibly because the winds are too backed early in the deployment, but become too veered later. The 20 May supercell's rotational velocity drops while interacting and merging with a nearby supercell to its northeast, and possibly as a result the wind field does not back and strengthen as the storm approaches the lidar. An intriguing result here is that WoFS does back and strengthen the wind field more than what was observed, suggesting that the mesoyclones in the WoFS forecasts did not decrease in intensity.

WoFS does perform well, however, in the second deployment on 20 May while the mesocyclone is gaining strength. WoFS well forecasts the veering of the wind-field as the storm moves to an almost due north orientation from the lidar. This change of the mesocyclone strength is smaller in the second deployment versus the first on 20 May. If WoFS is having difficulty forecasting storm modification on the inflow environment, one would expect the errors to be larger in the second deployment considering the storm is closer to the lidar than in the first deployment. However the errors are smaller in the second deployment, which may be influenced by the more constant rotational velocity of the mesocyclone during this period.

The two deployments on 23 May corroborate the hypothesis that the WoFS wind errors may have a dependence on the magnitude of change in mesocyclone strength with time. The rotational velocity slightly increases (~ 5 ms^{-1}) over the first deployment as the storm approaches the lidar. The wind field is observed to back and strengthen, and WoFS forecasts this change, albeit to a lesser degree. Like the 17 May deployment, the winds in the first 23 May deployment are backed too far in WoFS at the beginning of the deployment, then are too veered by the end. The second deployment on 23 May may best illustrate the dependence of WoFS errors on mesocyclone strength. As the mesocyclone strengthens by 20 ms^{-1} over 15 minutes, the errors grow to nearly 5 ms^{-1} in both the zonal and meridional components of the wind field. The mesocyclone weakens in the later 10 minutes of the deployment and the wind errors drop. Note that the drop in errors of the u-component of the wind is likely influenced by the northern orientation of the storm-relative to the lidar at this time as well (no u-component of low-pressure perturbation induced pressure gradient force).

5.3 Summary and Conclusions

Mobile radiosonde and lidar observations collected during the TORUS 2019 field campaign are compared to WoFS environmental forecasts using three case studies: The 17 May, 20 May, and 23 May supercells. Of the four supercells targeted on these days, 3 were tornadic within an hour of the release time of several radiosondes and during the period of high-resolution lidar observations. The data sets provided by the 16 radiosondes allow for WoFS forecasts of convective parameters like CAPE and SRH to be evaluated. WoFS consistently over forecasted CAPE in both the near and far field, owing to positive surface temperature errors, too dry PBLs, and negative temperature errors above the PBL. The YSU scheme often predicts lower CAPE and SRH than MYJ and MYNN, supporting the work of Potvin et al. (2020), Cohen et al. (2015),and (2017), where they found the non-local schemes often under estimate 03SRH and under predicted MLCAPE(in southeast U.S. convective environments for Cohen et al. 2015 and 2017), both thought to be impacts of more aggressive mixing in the non-local versus local scheme.

The lidar deployments collectively illustrate that the wind field in WoFS appears to be modified by the modeled storms, mostly in the sense that the wind field is strengthened in the direction of the supercell due to the low-pressure perturbation induced by the rotating updraft. For the case in which the rotational velocity of the observed storm stays almost constant, the WoFS forecasts under predict the backing (and large SRH) observed in the inflow ahead of the approaching storm. In the other two cases, the observed storm's rotational velocity changes with time and the character of the WoFS wind errors are different. The observed winds appear to respond as expected to the changes in rotational velocity and WoFS appears to forecast the same responses, but to a lesser extent. For example, the lidar deployment in which the WoFS over forecasts the near-storm winds appears to correspond to a period when the observed storm temporarily weakened.

Scientific questions and how they were answered by the study:

1. How closely is WoFS representing the inflow environment?

- WoFS forecasts environments thermodynamically and kinematically supportive of supercells
- WoFS over forecasts MLCAPE in all observations
- WoFS under forecasts SRH late on 17 May, but forecasts small (<100 m^2s^{-2}) errors in nearly all observations on 20 May and 23rd

2. How accurate are WoFS storm scale predictions?
   - Errors typically less than 40 km, larger errors on 23 May likely a result of indistinguishable UH objects
3. To what extent is WoFS predicting storm modification to the inflow environment?
   - WoFS forecasts storm modified wind fields with errors less than 5 ms^{-1} during periods of relatively constant rotational velocity (17 May and 2nd lidar deployment on 20 May)
   - Errors in WoFS wind field forecasts grow (>5ms^{-1}) during periods of rapid change in rotational velocity (1st lidar deployment on 20 May and 2nd deployment on 23 May)
4. Can the ensemble mean be improved by weighting members based on PBL scheme?
   - YSU forecasts smallest MLCAPE of all schemes resulting in smaller errors than non-local schemes
   - YSU schemes forecast more reasonable inversions layers on 17 May
   - No PBL scheme consistently forecasts smaller errors in SRH or storm location

6 Future Research

A natural future project would be to extend current analysis to more case studies from TORUS 2019 to see if trends found in these case studies are representative of the rest of the mission. TORUS2020 is postponed, and may offer more case studies from future deployments. Several more days are available for study. The analysis method chosen for these case studies inherently influences the result, as with any scientific analysis. It is always good practice to vary aspects of the analysis to gauge that inherent influence. A few changes that would be interesting to make:

1. Reproduce the same lidar figures but use lagged observations (e.g. comparing a 2230 lidar observation to the 2235 forecasts instead of the 2230 UTC forecast. These analyses may indicate if WoFS just needs more time to assimilate the changes in mesocyclone strength, or if the errors seen in this study as dependent on some other cause.
2. Recalculate observed convective parameters using the observed variable profiles that have been spatially averaged onto the WoFS vertical grid. This will eliminate and influence on the errors by resolution differences. In a related fashion, a sensitivity study could also be performed on the 100-meter window over which the data were averaged.

Cohen et al. (2017) highlighted the need for regionally dependent studies as models may behave differently based on typically environmental set-ups (e.g. higher SRH and lower CAPE in American southeast). This study analyzed WoFS environmental forecasts in particularly late day tornadic supercells during the spring-time in the American Great Plains. Exploring WoFS environmental forecasts near either tornadic or non tornadic supercells in other parts of the country and times of day or year would provide WoFS developers with a better understanding of the WoFS forecasts. Similarly, if enough observations are available, the analysis could be split based on if the supercells are tornadic or not to investigate if WoFS forecasts environments similar to the composites used in Coffer et al. (2015), which may have important implications on the WoFS ability to discern between tornadic and non-tornadic storms.

The observational data sets collected by TORUS provided a rare opportunity to evaluate WoFS environmental forecasts in, often tornadic, supercell environments. However, WoFS, if it is to be useful to most forecasters in the future, must also be evaluated in other severe weather contexts such as hurricanes. While WSR-88D data have been used in previous studies to evaluate WoFS, the time series provided by a ground based lidar in a land falling hurricane would provide the opportunity to evaluate WoFS wind forecasts in the lowest $\sim$ 2 km for potentially days. Granted the lidar would only observe during periods without precipitation and would ideally be accompanied by radiosonde and mobile radar observations.

7 Reference List

Blumberg, W. G., Halbert, K. T., Supinie, T. A., Marsh, P. T., Thompson, R. L., amp; Hart, J. A. (2017). SHARPpy: An Open-Source Sounding Analysis Toolkit for the Atmospheric Sciences. Bulletin of the American Meteorological Society, 98(8), 1625-1636. doi:10.1175/bams-d-15-00309.1

Britt, K. C., P. S. Skinner, P. L. Heinselman, and K. H. Knopfmeier, 2020: Effects of horizontal grid spacing and inflow environment on forecasts of cyclic mesocylogenesis in NSSL's Warn-on-Forecast System (WoFS). Wea. Forecasting, 35, Conditionally Accepted.

Brooks, H. E. (2004). TORNADO-WARNING PERFORMANCE IN THE PAST AND FUTURE: A Perspective from Signal Detection Theory. Bulletin of the American Meteorological Society, 85(6), 837-844. doi:10.1175/bams-85-6-837

Brooks, H. E., Doswell, C. A. (2002). Deaths in the 3 May 1999 Oklahoma City Tornado from a Historical Perspective. Weather and Forecasting, 17(3), 354-361. doi:10.1175/1520-0434(2002)0172.0.co;2

Bryan, G. H., Parker, M. D. (2010). Observations of a Squall Line and Its Near Environment Using High-Frequency Rawinsonde Launches during VORTEX2. Monthly Weather Review, 138(11), 4076-4097. doi:10.1175/2010mwr3359.1

Clark, A. J., Weiss, S. J., Kain, J. S., Jirak, I. L., Coniglio, M., Melick, C. J., . . . Correia, J. (2012). An Overview of the 2010 Hazardous Weather Testbed Experimental Forecast Program Spring Experiment. Bulletin of the American Meteorological Society, 93(1), 55-74. doi:10.1175/bams-d-11-00040.1

Coffer, B. E., Parker, M. D. (2016). Simulated Supercells in Nontornadic and Tornadic VORTEX2 Environments. Monthly Weather Review, 145(1), 149-180. doi:10.1175/mwr-d-16-0226.1

Cohen, A. E., Cavallo, S. M., Coniglio, M. C., Brooks, H. E. (2015). A Review of Planetary Boundary Layer Parameterization Schemes and Their Sensitivity in Simulating Southeastern U.S. Cold Season Severe Weather Environments. Weather and Forecasting, 30(3), 591-612. doi:10.1175/waf-d-14-00105.1

Cohen, A. E., Cavallo, S. M., Coniglio, M. C., Brooks, H. E., Jirak, I. L. (2017). Evaluation of Multiple Planetary Boundary Layer Parameterization Schemes in Southeast U.S. Cold Season Severe Thunderstorm Environments. Weather and Forecasting, 32(5), 1857-1884. doi:10.1175/waf-d-16-0193.1

Collins, J. (2014). The NOAA Hurricane Hunters: A Historical and Mission Perspective. Retrieved 2020, from file:///E:/Jordan20Master's/Literature/P320Orion.pdf

Coniglio, M. C. (2012). Verification of RUC 0–1-h Forecasts and SPC Mesoscale Analyses Using VORTEX2 Soundings. Weather and Forecasting, 27(3), 667-683. doi:10.1175/waf-d-11-00096.1

Coniglio, M. C., Correia, J., Marsh, P. T., Kong, F. (2013). Verification of Convection-Allowing WRF Model Forecasts of the Planetary Boundary Layer Using Sounding Observations. Weather and Forecasting, 28(3), 842-862. doi:10.1175/waf-d-12-00103.1

Davies-Jones, R. (1984). Streamwise Vorticity: The Origin of Updraft Rotation in Supercell Storms. Journal of the Atmospheric Sciences, 41(20), 2991-3006. doi:10.1175/1520-0469(1984)0412.0.co;2

Evans, C., Weiss, S. J., Jirak, I. L., Dean, A. R., Nevius, D. S. (2018). An Evaluation of Paired Regional/Convection-Allowing Forecast Vertical Thermodynamic Profiles in Warm-Season, Thunderstorm-Supporting Environments. Weather and Forecasting, 33(6), 1547-1566. doi:10.1175/waf-d-18-0124.1

Frame, J., Markowski, P. (2013). Dynamical Influences of Anvil Shading on Simulated Supercell Thunderstorms. Monthly Weather Review, 141(8), 2802-2820. doi:10.1175/mwr-d-12-00146.1

Gallo, B. T., Clark, A. J., Jirak, I., Kain, J. S., Weiss, S. J., Coniglio, M., . . . Willington, S. (2017). Breaking New Ground in Severe Weather Prediction: The 2015 NOAA/Hazardous Weather Testbed Spring Forecasting Experiment. Weather and Forecasting, 32(4), 1541-1568. doi:10.1175/waf-d-16-0178.1

Hastings, R., amp; Richardson, Y. (2016). Long-Term Morphological Changes in Simulated Supercells Following Mergers with Nascent Supercells in Directionally Varying Shear. Monthly Weather Review, 144(2), 471-499. doi:10.1175/mwr-d-15-0193.1

Ii, D. T., Wicker, L. J., Mansell, E. R., Tanamachi, R. L. (2012). Impact of the Environmental Low-Level Wind Profile on Ensemble Forecasts of the 4 May 2007 Greensburg, Kansas, Tornadic Storm and Associated Mesocyclones. Monthly Weather Review, 140(2), 696-716. doi:10.1175/mwr-d-11-00008.1

Jones, T. A., Knopfmeier, K., Wheatley, D., Creager, G., Minnis, P., Palikonda, R. (2016). Storm-Scale Data Assimilation and Ensemble Forecasting with the NSSL Experimental Warn-on-Forecast System. Part II: Combined Radar and Satellite Data Experiments. Weather and Forecasting, 31(1), 297-327. doi:10.1175/waf-d-15-0107.1

Kerr, C. A., Stensrud, D. J., Wang, X. (2019). Diagnosing Convective Dependencies on Near-Storm Environments Using Ensemble Sensitivity Analyses. Monthly Weather Review, 147(2), 495-517. doi:10.1175/mwr-d-18-0140.1

Klemp, J. B., Rotunno, R. (1982). High Resolution Numerical Simulations of the Tornadic Region Within a Mature Thunderstorm. Intense Atmospheric Vortices, 191-203. doi:10.1007/978-3-642-81866-0-15

Klemp, J. B., Rotunno, R. (1983). A Study of the Tornadic Region within a Supercell Thunderstorm. Journal of the Atmospheric Sciences, 40(2), 359-377. doi:10.1175/1520-0469(1983)0402.0.co;2

Klemp, J. B., Wilhelmson, R. B. (1978). The Simulation of Three-Dimensional Convective Storm Dynamics. Journal of the Atmospheric Sciences, 35(6), 1070-1096. doi:10.1175/1520-0469(1978)0352.0.co;2

Liang, X. (2007). An Integrating Velocity–Azimuth Process Single-Doppler Radar Wind Retrieval Method. Journal of Atmospheric and Oceanic Technology, 24(4), 658-665. doi:10.1175/jtech2047.1

Markowski, P. M., amp; Richardson, Y. P. (2013). The Influence of Environmental Low-Level Shear and Cold Pools on Tornadogenesis: Insights from Idealized Simulations. Journal of the Atmospheric Sciences, 71(1), 243-275. doi:10.1175/jas-d-13-0159.1

Parker, M. D. (2014). Composite VORTEX2 Supercell Environments from Near-Storm Soundings. Monthly Weather Review, 142(2), 508-529. doi:10.1175/mwr-d-13-00167.1

Pielke, R., Carbone, R. E. (2002). Weather Impacts, Forecasts, and Policy: An Integrated Perspective. Bulletin of the American Meteorological Society, 83(3), 393-403. doi:10.1175/1520-0477(2002)0832.3.co;2

Potvin, C. K., Elmore, K. L., amp; Weiss, S. J. (2010). Assessing the Impacts of Proximity Sounding Criteria on the Climatology of Significant Tornado Environments. Weather and Forecasting, 25(3), 921-930. doi:10.1175/2010waf2222368.1

Potvin, C. K., Skinner, P. S., Hoogewind, K. A., Coniglio, M. C., Gibbs, J. A., Clark, A. J., . . . Smith, E. N. (2020). Assessing Systematic Impacts of PBL Schemes on Storm Evolution in the NOAA Warn-on-Forecast System. Monthly Weather Review, 148(6), 2567-2590. doi:10.1175/mwr-d-19-0389.1

Rasmussen, E. N., amp; Blanchard, D. O. (1998). A Baseline Climatology of Sounding-Derived Supercell andTornado Forecast Parameters. Weather and Forecasting, 13(4), 1148-1164. doi:10.1175/1520-0434(1998)0132.0.co;2

Rotunno, R., Klemp, J. B. (1982). The Influence of the Shear-Induced Pressure Gradient on Thunderstorm Motion. Monthly Weather Review, 110(2), 136-151. doi:10.1175/1520-0493(1982)1102.0.co;2

Serafin, R. J., Wilson, J. W. (2000). Operational Weather Radar in the United States: Progress and Opportunity. Bulletin of the American Meteorological Society, 81(3), 501-518. doi:10.1175/1520-0477(2000)0812.3.co;2

Simmons, K. M., Sutter, D. (2005). WSR-88D Radar, Tornado Warnings, and Tornado Casualties. Weather and Forecasting, 20(3), 301-310. doi:10.1175/waf857.1

Skamarock, W. C., Klemp, J. B. (2008). A time-split nonhydrostatic atmospheric model for weather research and forecasting applications. Journal of Computational Physics, 227(7), 3465-3485. doi:10.1016/j.jcp.2007.01.037

Skinner, P. S., Wheatley, D. M., Knopfmeier, K. H., Reinhart, A. E., Choate, J. J., Jones, T. A., . . . Palikonda, R. (2018). Object-Based Verification of a Prototype Warn-on-Forecast System. Weather and Forecasting, 33(5), 1225-1250. doi:10.1175/waf-d-18-0020.1

Skinner et al. (2016). Application of Two Spatial Verification Methods to Ensemble Forecasts of Low-Level Rotation. Weather and Forecasting, 31(3), 713-735. doi:10.1175/waf-d-15-0129.1

Skinner et al. (2018). Object-Based Verification of a Prototype Warn-on-Forecast System. Weather and Forecasting, 33(5), 1225-1250. doi:10.1175/waf-d-18-0020.1

Smith, E. N., M.C. Coniglio, S. Waugh, 2020: TORUS Doppler Lidar and Radiosonde Wind Observation Intercomparison. 10th Symposium on Lidar Atmospheric Applications, Amer. Meteor. Soc., Boston, MA,
https://ams.confex.com/ams/2020Annual/meetingapp.cgi/Paper/366169

Smith, T. M., Lakshmanan, V., Stumpf, G. J., Ortega, K. L., Hondl, K., Cooper, K., . . . Brogden, J. (2016). Multi-Radar Multi-Sensor (MRMS) Severe Weather and Aviation Products: Initial Operating Capabilities. Bulletin of the American Meteorological Society, 97(9), 1617-1630. doi:10.1175/bams-d-14-00173.1

Snook, N., Jung, Y., Brotzge, J., Putnam, B., Xue, M. (2016). Prediction and Ensemble Forecast Verification of Hail in the Supercell Storms of 20 May 2013. Weather and Forecasting, 31(3), 811-825. doi:10.1175/waf-d-15-0152.1

Stensrud, D. J. (2007). Parameterization Schemes. doi:10.1017/cbo9780511812590

Stensrud, D. J., Xue, M., Wicker, L. J., Kelleher, K. E., Foster, M. P., Schaefer, J. T., . . . Tuell, J. P. (2009). Convective-Scale Warn-on-Forecast System. Bulletin of the American Meteorological Society, 90(10), 1487-1500. doi:10.1175/2009bams2795.1

Stensrud, D. J., Wicker, L. J., Xue, M., Dawson, D. T., Yussouf, N., Wheatley, D. M., . . . Brewster, K. A. (2013). Progress and challenges with Warn-on-Forecast. Atmospheric Research, 123, 2-16. doi:10.1016/j.atmosres.2012.04.004

Straka, J. M., Rasmussen, E. N., Fredrickson, S. E. (1996). A Mobile Mesonet for Finescale Meteorological Observations. Journal of Atmospheric and Oceanic Technology, 13(5), 921-

936. doi:10.1175/1520-0426(1996)0132.0.co;2

Stull, R. B. (1991). A comparison of parameterized vs. measured transilient mixing coefficients for a convective mixed layer. Boundary-Layer Meteorology, 55(1-2), 67-90. doi:10.1007/bf00119327

Supinie, T. A., Yussouf, N., Jung, Y., Xue, M., Cheng, J., Wang, S. (2017). Comparison of the Analyses and Forecasts of a Tornadic Supercell Storm from Assimilating Phased-Array Radar and WSR-88D Observations. Weather and Forecasting, 32(4), 1379-1401. doi:10.1175/waf-d-16-0159.1

Thompson, R. L., Mead, C. M., amp; Edwards, R. (2007). Effective Storm-Relative Helicity and Bulk Shear in Supercell Thunderstorm Environments. Weather and Forecasting, 22(1), 102-115. doi:10.1175/waf969.1

Wade, A. R., Coniglio, M. C., Ziegler, C. L. (2018). Comparison of Near- and Far-Field Supercell Inflow Environments Using Radiosonde Observations. Monthly Weather Review, 146(8), 2403-2415. doi:10.1175/mwr-d-17-0276.1

Weisman, M. L., Klemp, J. B. (1982). The Dependence of Numerically Simulated Convective Storms on Vertical Wind Shear and Buoyancy. Monthly Weather Review, 110(6), 504-520. doi:10.1175/1520-0493(1982)1102.0.co;2

Weisman, M. L., Davis, C., Wang, W., Manning, K. W., Klemp, J. B. (2008). Experiences with 0–36-h Explicit Convective Forecasts with the WRF-ARW Model. Weather and Forecasting, 23(3), 407-437. doi:10.1175/2007waf2007005.1

Wheatley, D. M., Knopfmeier, K. H., Jones, T. A., Creager, G. J. (2015). Storm-Scale Data Assimilation and Ensemble Forecasting with the NSSL Experimental Warn-on-Forecast System. Part I: Radar Data Experiments. Weather and Forecasting, 30(6), 1795-1817. doi:10.1175/waf-d-15-0043.1

Wicker, L. J., Wilhelmson, R. B. (1995). Simulation and Analysis of Tornado Development and Decay within a Three-Dimensional Supercell Thunderstorm. Journal of the Atmospheric Sciences, 52(15), 2675-2703. doi:10.1175/1520-0469(1995)0522.0.co;2

Wurman, J., D. Dowell, Y. Richardson, P. Markowski, E. Rasmussen, D. Burgess, L. Wicker, and H.Bluestein, 2012: The second Verification of the Origins of Rotation in Tornadoes Experiment:VORTEX2. Bull. Amer. Meteor. Soc., 93, 1147–1170.

Yussouf, N., Gao, J., Stensrud, D. J., Ge, G. (2013). The Impact of Mesoscale Environmental Uncertainty on the Prediction of a Tornadic Supercell Storm Using Ensemble Data Assimilation Approach. Advances in Meteorology, 2013, 1-15. doi:10.1155/2013/731647

Yussouf, N., Kain, J. S., Clark, A. J. (2016). Short-Term Probabilistic Forecasts of the 31 May 2013 Oklahoma Tornado and Flash Flood Event Using a Continuous-Update-Cycle

Storm-Scale Ensemble System. Weather and Forecasting, 31(3), 957-983. doi:10.1175/waf-d-15-0160.1